MAPPING TOPOLOGICAL MAGNETIZATION AND MAGNETIC SKYRMIONS

by

JORDAN J. CHESS

A DISSERTATION

Presented to the Department of Physics
and the Graduate School of the University of Oregon
in partial fulfillment of the requirements
for the degree of
Doctor of Philosophy

December 2017

DISSERTATION APPROVAL PAGE

Student: Jordan J. Chess

Title: Mapping Topological Magnetization and Magnetic Skyrmions

This dissertation has been accepted and approved in partial fulfillment of the requirements for the Doctor of Philosophy degree in the Department of Physics by:

Stephen Kevan	Chair
Benjamin J. McMorrran	Advisor
Raghuveer Parthasarathy	Core Member
David Johnson	Institutional Representative

and

Sara D. Hodges	Interim Vice Provost and Dean of the Graduate School

Original approval signatures are on file with the University of Oregon Graduate School.

Degree awarded December 2017

DISSERTATION ABSTRACT

Jordan J. Chess

Doctor of Philosophy

Department of Physics

December 2017

Title: Mapping Topological Magnetization and Magnetic Skyrmions

A 2014 study by the US Department of Energy conducted at Lawrence Berkeley National Laboratory estimated that U.S. data centers consumed 70 billion kWh of electricity[1]. This represents about 1.8% of the total U.S. electricity consumption. Putting this in perspective 70 billion kWh of electricity is the equivalent of roughly 8 big nuclear reactors, or around double the nation's solar panel output[2]. Developing new memory technologies capable of reducing this power consumption would be greatly beneficial as our demand for connectivity increases in the future. One newly emerging candidate for an information carrier in low power memory devices is the magnetic skyrmion. This magnetic texture is characterized by its specific non-trivial topology, giving it particle-like characteristics. Recent experimental work has shown that these skyrmions can be stabilized at room temperature and moved with extremely low electrical current densities. This rapidly developing field requires new measurement techniques capable of determining the topology of these textures at greater speed than previous approaches. In this dissertation, I give a brief introduction to the magnetic structures found in Fe/Gd multilayered systems. I then present newly developed techniques that streamline the analysis of

Lorentz Transmission Electron Microscopy (LTEM) data. These techniques are then applied to further the understanding of the magnetic properties of these Fe/Gd based multilayered systems.

This dissertation includes previously published and unpublished co-authored material.

CURRICULUM VITAE

NAME OF AUTHOR: Jordan J. Chess

GRADUATE AND UNDERGRADUATE SCHOOLS ATTENDED:

University of Oregon, Eugene
Boise State University, Boise

DEGREES AWARDED:

Doctor of Philosophy, Physics, 2017, University of Oregon
Bachelor of Science, Physics, 2013, Boise State

AREAS OF SPECIAL INTEREST:

Data Driven Decision Making
Metrology
Memory Devices

PROFESSIONAL EXPERIENCE:

Graduate Research Assistant, University of Oregon, 2013-2017

GRANTS, AWARDS AND HONORS:

Poster Award, 59th Annual Conference on Magnetism and Magnetic Materials, 2014

First-Year Fellowship Award, 2013

PUBLICATIONS:

JJ Chess, SA Montoya, EE Fullerton, and BJ McMorran. *AIP Advances* **7** 056807 (2017).

S Montoya, S Couture, **J Chess**, J Lee, N Kent, M-Y Im, S Kevan, P Fischer, B McMorran, and S Roy. *Physical Review B* **95** 224405 (2017).

JJ Chess, SA Montoya, TR Harvey, C Ophus, S Couture, V Lomakin, EE Fullerton, BJ McMorran. *Ultramicroscopy* **177** 78 (2017).

S Montoya, S Couture, **J. Chess**, J Lee, N Kent, D Henze, S Sinha, M-Y Im, S Kevan, and P Fischer. *Physical Review B* **95** 024415 (2017).

TR Harvey, JS Pierce, JJ Chess, BJ McMorran. arXiv:1507.01810.

C Ophus, J Ciston, J Pierce, TR Harvey, **J Chess**, BJ McMorran, C Czarnik, HH Rose, P Ercius. *Nat. Comm.* **7** 10719 (2016).

JT Lee, **J Chess**, S Montoya, X Shi, N Tamura, S Mishra, P Fischer, B McMorran, S Sinha, and E Fullerton. *Applied Physics Letters* **109** 022402 (2016).

TABLE OF CONTENTS

Chapter Page

LIST OF FIGURES

CHAPTER I

INTRODUCTION

From Bubbles to Skyrmion Racetrack Memories

Magnetic bubbles, cylindrical domains in out-of-plane media, were investigated in the 1960–70s as bits in solid state data storage media[3]. In the 80s they were used in commercial devices that moved bubbles down a thin magnetic track with magnetic field gradients, and had no moving parts. At the time, these devices had memory densities similar to hard drives and performance on par with core memory; because of this they were largely thought to be the memory of the future, as evidenced by references to them found in multiple patent applications through the 1980s[4, 5]. As you might guess, bubble memory's reign was short-lived as it was eclipsed by improvements in the performance of rotating magnetic hard drives.

More recently, spurred by advancements in current controlled domain wall motion, interest in a track-like memory with no moving parts has reemerged[6]. In their original 2008 proposal Parkin *et al.* suggested a solid-state memory composed of U-shaped vertical nanowire tracks on which domain walls could be moved back and forth by a spin-polarized current. During this motion, the walls travel past stationary read and write elements positioned at the bottom of the U[6]. Progress on domain-wall based racetrack memories continues[7], but in a further echo of the past, the magnetic skyrmion has emerged as the most promising information carrier for racetrack memory[8].

Skyrmions, named after the British physicist Tony Skyrme, are topologically stable solitons originally proposed as a model for nucleons[9]. The first experimental identifications of these particle-like topological defects in magnetic materials was in 2009, when the mysterious A phase of MnSi was identified as a magnetic skyrmion lattice[10, 11, 12]. In this material and other non-centrosymmetric systems, antisymmetric exchange, also referred to as the Dzyaloshinskii-Moriya interaction (DMI), acts to stabilize these structures. Later, Yu *et al.* imaged current-induced skyrmion flow using Lorentz transmission electron microscopy (LTEM)[13]. They estimated the minimum critical current density for skyrmion motion to be roughly 10 A cm^{-2}, which is several orders of magnitude smaller than the value for domain wall motion ($\sim 10^7$ A cm^{-2})[13]. This low critical current density, coupled with the skyrmion's ability to pass by structural defects in a nanowire[8], are what make them attractive for low power memory and logic applications.

Topological Magnetic Textures

As topological defects, the whirling magnetization of skyrmions can be characterized by a non-zero topological number (S_k), given by

$$S_k = \frac{1}{4\pi} \int \mathbf{m} \cdot (\partial_x \mathbf{m} \times \partial_y \mathbf{m}) \, \mathrm{d}x \, \mathrm{d}y, \tag{1.1}$$

where $\mathbf{m}$ is the normalized magnetization. This integral is also called the local topological density, and counts the number of times and direction $\mathbf{m}$ wraps the unit sphere. In cases with cylindrical symmetry, this equation is generally more easily evaluated in spherical coordinates in which case we can express the normalized magnetization as,

$$\mathbf{m} = \{\cos \mathbf{\Phi}(\phi) \sin \mathbf{\Theta}(\rho), \sin \mathbf{\Phi}(\phi) \sin \mathbf{\Theta}(\rho), \cos \mathbf{\Theta}(\rho)\}. \tag{1.2}$$

This parameterization also makes the mapping to the unit sphere more explicit. Equation 1.1 then becomes[14],

$$S_k = \frac{1}{4\pi} \int_0^\infty \mathrm{d}\rho \int_0^{2\pi} \mathrm{d}\phi \frac{\mathrm{d}\boldsymbol{\Theta}(\rho)}{\mathrm{d}\rho} \frac{\mathrm{d}\boldsymbol{\Phi}(\phi)}{\mathrm{d}\phi} \sin \boldsymbol{\Theta}(\rho) = \cos \boldsymbol{\Theta}(\rho)|_0^\infty \boldsymbol{\Phi}(\phi)|_0^{2\pi}. \tag{1.3}$$

Choosing the polarity of the skyrmion such that the magnetization points up at $\rho \to \infty$ and down at the origin leads to,

$$\cos \boldsymbol{\Theta}(\rho)|_0^\infty = 2. \tag{1.4}$$

Of the several possibilities for the remaining term, a particularly convenient one is

$$\boldsymbol{\Phi}(\phi) = n\phi + \gamma. \tag{1.5}$$

Above γ is referred to as the helicity, and n determines the skyrmion number, because

$$\boldsymbol{\Phi}(\phi)|_0^{2\pi} = 2\pi n + \gamma - 0 - \gamma = 2\pi n. \tag{1.6}$$

It is interesting to note that these topological considerations were known in the 70s and applied to characterize magnetic bubbles at the time[3]. In that context it was more common to use the winding number W to characterize the bubbles,

$$W = \frac{S_k}{p} \tag{1.7}$$

where p is the polarity. The advantage of the winding number is that it can easily be calculated visually by looking at the domain wall of a bubble or skyrmion. For a closed loop, one simply counts the total rotation of the magnetization along the loop.

Figure 1 shows various examples of skyrmions (or bubbles) with varying topology and helicity, both the skyrmion number and winding number are noted in the Figure. Topological defects with n=-1 are generally referred to as anti-skyrmions, while those with n=1 as skyrmions. Skyrmions are generally categorized as either Néel ($\gamma = 0, \pi$) or Bloch ($\gamma = \frac{\pi}{2}, \frac{3\pi}{2}$).

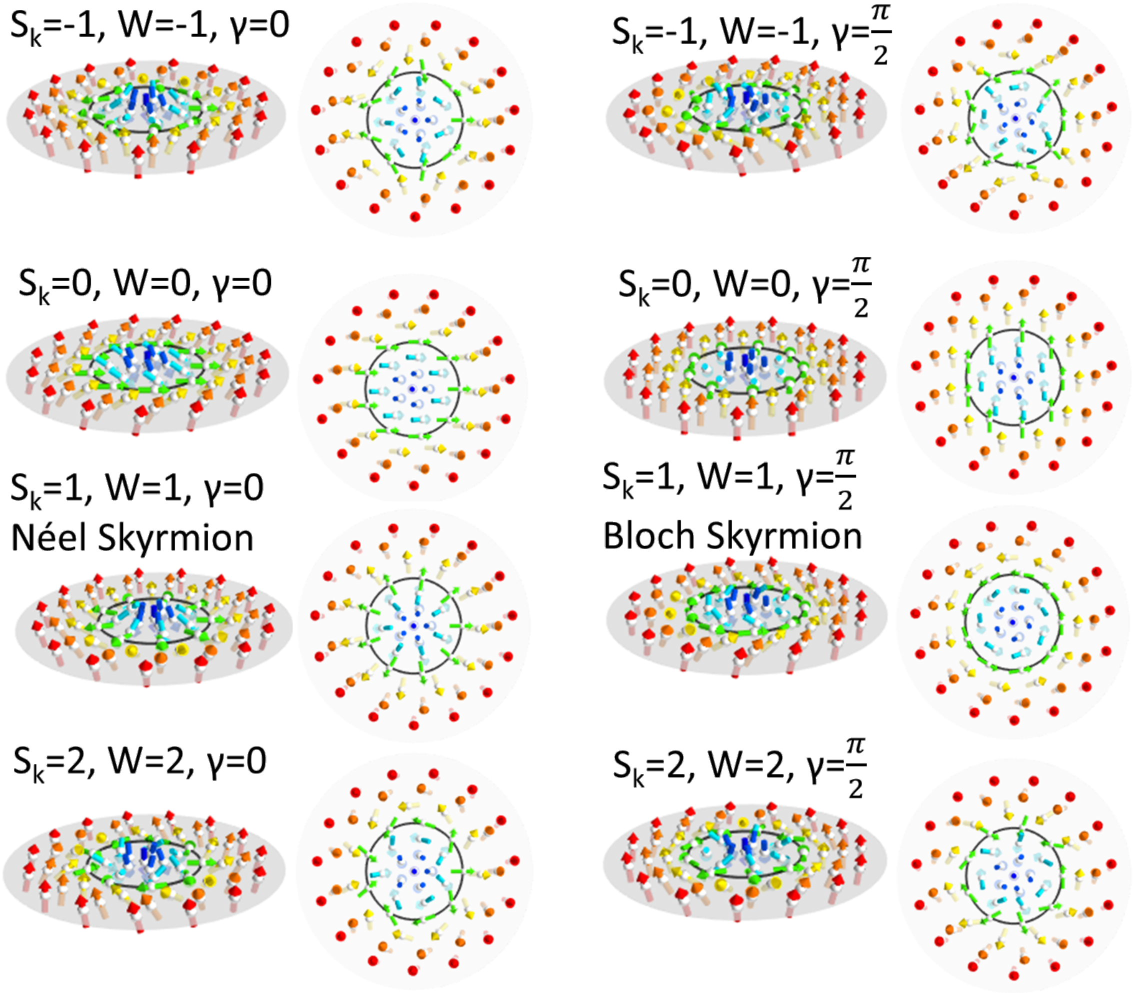

FIGURE 1. Topology of Various Field Configurations
The field configuration of various bubbles/skyrmions with different skyrmion number and helicity. The black line indicates the closed loop around which the winding number can be calculated.

Bubbles vs Skyrmions

At this point the reader may be questioning what differences, if any, are there between skyrmions and bubbles. There have been two competing camps: staunch DMI advocates[15], and topology-plus-properties pragmatists. The DMI advocates believe that a skyrmion requires two things: first it must have the proper topology, and second it must have a fixed chirality that is controlled by DMI in the Hamiltonian that both stabilizes the skyrmion topology making it a soliton and forces a specific chirality[15]. The pragmatists rely on a functional definition; a Skyrmion is a small ($<$ 100 nm), axisymmetric isolated state, with particle-like properties, has a topological charge of 1, is easily moved by a current, and is stable (in the sense that if it is a bit in a memory device it won't change from a 1 to a 0). To me, the first definition seems to have stronger support by individuals who care less about applications and more about new magnetic phenomenon, where the converse is true for the pragmatists definition (they just want the device to work).

In 2010 Ezawa[16] published an article claiming to have found 'giant Skyrmion' solutions, stabilized by dipole-dipole interactions. These states were around 1 μm in size. This was followed by a comment from Kiselev *et al.* arguing that in fact all Ezawa had found were well-known bubble domain solutions[15]. Kiselev *et al.* point out that these domains are not stable solitons, and result only from a competition between radial instability and elliptic instability. Further, Kiselev *et al.* lay out a distinction, that seems useful, that a skyrmion can be distinguished from a bubble with non-trivial topology by its radial profile. Skyrmions have a core size that is proportional to $|D|$, the magnitude of the DM interaction, while bubbles have extended cores with domain wall thickness $x_0 = \sqrt{A/K}$ where A is the exchange stiffness and K the anisotropy. It is useful to note that Kiselev *et al.* are making claims based on materials with $Q \gg 1$, where $Q = K/(2\pi M_s)$ where M_s is the saturation magnetization. Unfortunately, in my experience, at conferences, reading, and during the review process, speakers/questioners, authors, and referees seem to pick and choose which parts of the definitions they apply. This debate continues; two reviews published this year take either side of the argument[17, 18]. Jiang *et al.* make the point that because the most important factor is the topological class of the magnetic texture[18], measuring the radial extent of a magnetic core is not sufficient to identify a skyrmion.

There are indirect ways to deduce a domain's topology based on its dynamics[19], but the best way is to map the real space magnetization and directly determine the topology or winding number. The most employed technique used to quantify the topology of these magnetic feature is LTEM. The high resolution of this technique, the capability of mapping magnetic textures with nanometer resolution and widespread access to tools capable of performing LTEM, make this technique ideal for this rapidly progressing field. The focus of this dissertation is on the development and application of Lorentz TEM techniques specifically geared toward characterizing topological spin textures. In this dissertation, I will use the terms "skyrmions", and "topological bubbles" interchangeably.

This dissertation is composed of five previously published papers and 3 manuscripts that are in progress. Results from papers of which I was not the primary author are summarized and are mainly contained in chapter III. These chapters are organized as follows: an overview of LTEM and presentation of our new algorithm (SITIE) for interpreting LTEM images, a discussion of dipole-stabilized skyrmions observed in Fe/Gd using a combination of LTEM and X-ray scattering, application of the new LTEM algorithm to quasi-dynamic field sweep data and determination of domain wall chirality, and a combined approach to determine the full 3D structure of dipole-skyrmions using LTEM, Scanning Electron Microscopy with Polarization Analysis (SEMPA), and Landau Lifshitz Gilbert (LLG) simulations.

The following manuscripts are included in this work:

Chapter II. Lorentz Transmission Electron Microscopy

Jordan J Chess, Sergio A Montoya, Tyler R Harvey, Colin Ophus, Simon Couture, Vitaliy Lomakin, Eric E Fullerton, Benjamin J McMorran. "Streamlined approach to mapping the magnetic induction of skyrmionic materials." *Ultramicroscopy* **177**, 7883 (2017).

LTEM is one of a very few techniques for direct real space imaging of magnetic features at the nanoscale. For Fresnel-contrast LTEM, the transport of intensity equation (TIE) is the tool of choice for quantitative reconstruction of the local magnetic induction through the sample thickness. Typically this analysis requires collection of at least three images. Here we show that for uniform thin magnetic films which includes many skyrmionic samples, the magnetic induction can be quantitatively determined from a single defocused image using a simplified TIE approach.

Chapter III. Topological defects in Fe/Gd

Summary of results of three articles:

JC T Lee, JJ Chess, SA Montoya, X Shi, Nobumichi Tamura, SK Mishra, P Fischer, BJ McMorran, SK Sinha, EE Fullerton, SD Kevan, S Roy "Synthesizing skyrmion bound pairs in Fe-Gd thin films" *Applied Physics Letters* **109** 022402 (2016)

SA Montoya, S Couture, JJ Chess, JCT Lee, N Kent, D Henze, SK Sinha, M-Y Im, SD Kevan, P Fischer, BJ McMorran, V Lomakin, S Roy, EE Fullerton. "Tailoring magnetic energies to form dipole skyrmions and skyrmion lattices" *Physical Review B* **95(2)** 024415 (2017).

SA Montoya, S Couture, JJ Chess, JCT Lee, N Kent, D Henze, SK Sinha, M-Y Im, SD Kevan, P Fischer, BJ McMorran, V Lomakin, S Roy, EE Fullerton. "Resonant properties of dipole skyrmions in amorphous Fe/Gd multilayers." *Physical Review B* **95(22)** 224405 (2017).

The main material samples imaged in this dissertation are discussed in more detail, including the synthesis, characterization techniques, phase space diagram, resonance, and topological properties.

Chapter IV. Detecting chiral magnetic domains

Jordan J Chess, Sergio A Montoya, Eric E Fullerton, Benjamin J McMorran. "Determination of domain wall chirality using *in situ* Lorentz transmission electron microscopy." *AIP Advances* **7**, 056807 (2017).

Controlling domain wall chirality is increasingly seen in non-centrosymmetric materials. Mapping chiral magnetic domains requires knowledge about all the vector components of the magnetization, which poses a problem for conventional Lorentz transmission electron microscopy (LTEM) that is only sensitive to magnetic fields perpendicular to the electron beams direction of travel. The standard approach in LTEM for determining the third component of the magnetization is to tilt the sample to some angle and record a second image. This presents a problem for any domain structures that are stabilized by an applied external magnetic field (e.g. skyrmions), because the standard LTEM setup does not allow independent control of the angle of an applied magnetic field, and sample tilt angle. Here we show that applying a modified transport of intensity equation analysis to LTEM images collected during an applied field sweep, we can determine the domain wall chirality of labyrinth domains in a perpendicularly magnetized material, avoiding the need to tilt the sample.

Chapter V. Improved domain wall detection

Jordan J Chess, Harjasleen Gulati, and Benjamin J McMorran. “Python tools for domain wall detection” Manuscript in progress

The measurement technique presented in chapter IV is quite labor intensive because of the need to segment the images. We present a supervised machine learning algorithm that utilizes the labeled data used in chapter IV to detect edges and segment new data.

Chapter VI. Quantitative analysis of chirality measurements

The algorithm developed in chapter V and the technique presented in chapter IV are applied to a statistically significant number of images.

Jordan J Chess, Sergio A Montoya, Harjasleen Gulati, Eric E Fullerton, Benjamin J McMorran. “Control of Bloch walls chirality using asymmetrical layer stacking in Fe/Gd/Pt/Ir multilayer films” Manuscript in progress.

Asymmetrical layer stacking of ferromagnetic and heavy metal films, such as Co/Pt, is known to produce interfacial DMI (iDMI) and explains the presence of Néel domain walls with fixed chirality in these systems. The energy term describing iDMI evaluates to zero for Bloch domain walls, so one would not expect asymmetrical layer stacking to effect the chirality of Bloch walls. We demonstrate using both topological hall effect measurements, and real space mapping of Bloch domain walls with a fixed chirality. This result would only be expected for bulk DMI and not iDMI, indicating a need for further theoretical investigations into these systems.

Chapter VII. 3D structure of dipole skyrmions

JJ Chess, SA Montoya, SB Propp, I Gilbert, S Couture, JV Lomakin, JJ Razink, J Unguris EE Fullerton, BJ McMorran. “Determination of the 3D structure of dipole-skyrmions” Manuscript in progress

LTEM, and SEMPA are used to confirm the results of LLG simulations giving the full 3-dimensional structure of diple-skyrmions in Fe/Gd. This three dimensional object can be described as a stack or string of two dimensional skyrmions. The helicity of each of these skyrmions rotates through the thickness of the film following a hyperbolic tangent curve. A three dimensional mathematical model is fit to the LLG data, and this model is used to calculate the Hopf index of the object.

CHAPTER II

LORENTZ TRANSMISSION ELECTRON MICROSCOPY

Note on 'Streamlined Approach to Mapping the Magnetic Induction of Skyrmionic Materials'

From Jordan J Chess *et al.*, *Ultramicroscopy* **177**, 78-83 (2017).

I conceived of the idea, inspired by a suggestion from Vincenzo Grillo to try and use only two images for TIE. The samples were produced by Sergio Montoya. The LLG simulations used to simulate the LTEM images were done by Simon Couture. Colin Ophus assisted in developing the ideas in the supplementary material, and helped me find errors in my original TIE code. Colin Ophus and Tyler Harvey both gave coding pointers. I performed the LTEM simulations, recorded experimental data, analyzed the experimental and simulated data, produced all figures, and wrote the manuscript with input from co-authors.

Classical Treatment of LTEM

Lorentz TEM is sensitive to components of the magnetic induction perpendicular to the propagation direction of the electron beam. Classically this can be understood as the Lorentz force acting on the electron as it passes through the magnetic field produced by the material. This model is useful in estimating the magnitude of an LTEM signal, typically characterized by the Lorentz deflection angle. If we first consider a uniformly magnetized foil with magnetization pointing the in x-direction and thickness t, the momentum transferred to an electron traveling down the z-axis can be written as[20],

$$p_y = eB_0 t, \tag{2.1}$$

where e is the electron charge, and B_0 is the magnitude of the magnetic field. Dividing this by the z momentum gives the Lorentz deflection angle (θ_L). If we make the approximation that $p \approx p_z$ we can substitute in the de Broglie relation ($p = h/\lambda$) which yields[20],

$$\theta_L = \frac{e\lambda}{h} B_0 t. \tag{2.2}$$

In electron microscopy literature $e\lambda/h$ is generally relabeled as $C_L(E)$, which including relevant relativistic effects needed for energies of a TEM is given by[20],

$$C_L(E) \approx \frac{9.37783}{\sqrt{E + 0.97485 \times 10^{-3} E^2}}\ \mu\text{rad/T/nm}, \tag{2.3}$$

here the accelerating potential E must be expressed in kilovolts. At 300 kV, the energy used for all of our LTEM experiments, $C_L(300) = 0.476050$. For a 100 nm foil with magnetic induction of 1 T, this gives a deflection angle of $\theta_L = 47.6\,\mu$rad. One can compare this to typical Bragg angles, which are in the millirad range. This is why orders of magnitude higher defocus must be used to observe magnetic-related phase contrast, when compared to crystallographic information.

Quantum Treatment of LTEM

For a quantitative determination of the magnetic induction it is best to treat the system quantum mechanically. In this case the interaction of the electron with the magnetic field as it travels along a path L can be written in terms of the Aharonov-

Bohm phase shift,

$$\phi_m(\mathbf{r}_\perp) = -\frac{e}{\hbar}\int_L \mathbf{A}(\mathbf{r}_\perp, z)\cdot d\mathbf{r}. \tag{2.4}$$

The electron phase will also be affected by electrostatic interactions with the sample, which can be expressed in terms of a potential V as,

$$\phi_e(\mathbf{r}_\perp) = \frac{\pi}{\lambda E_t}\int_L V(\mathbf{r}_\perp, z)\,\mathrm{d}z, \tag{2.5}$$

where E_t is the total energy of the beam. Since I am only interested in magnetic interaction here, I will avoid a detailed discussion of the electrostatic contribution to the phase. To readers interested in this topic I would recommend the book by EJ Kirkland[21]. In experiments there are several methods used to discern electrostatic and magnetostatic contributions to the phase: flip the sample over and record a second dataset, change the energy of the beam, saturate the magnetic sample, or heat the magnetic sample above the Curie temperature. All of these rely on gaining two equations for the allowing one to solve for the two unknowns (ϕ_m, ϕ_e). Figure 2 shows a schematic version of the LTEM image formation process.

Outside of a few special cases with high symmetry, it is quite difficult to evaluate equation (2.4) analytically. This makes it necessary to have a numerical method of evaluating equation (2.4) for a given magnetization configuration.

The method employed in the LTEM simulations in this dissertation closely follow the paper by Walton *et al.* in which they present Matlab software for simulating LTEM images[22]. Their work is an implementation of the Mansuripur algorithm[23], which is a Fourier-based approach to easily calculate ϕ_m given a sample magnetization. This calculation is particularly simple if we make three assumptions: (1) the electron is traveling along the $\hat{\mathbf{z}}$ direction, (2) the magnetization is constant along $\hat{\mathbf{z}}$ (this

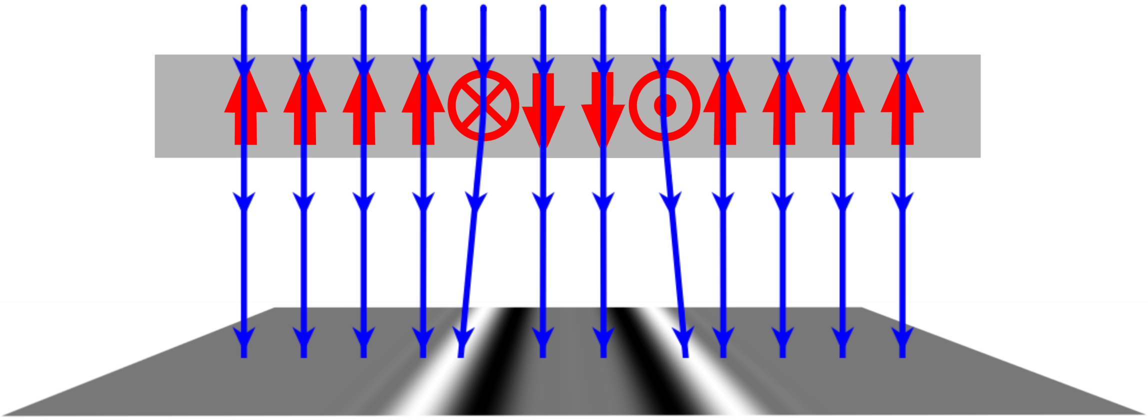

FIGURE 2. Schematic of LTEM image formation
Schematic showing how deflection of electrons transmitted through domain walls (classical) can generate contrast in a defocused LTEM image (simulated-quantum).

can be relaxed by treating the sample as thin slices), (3) the sample has a uniform thickness t. In this case the Fourier transform of the phase $\tilde{\phi}_m$ is given by,

$$\tilde{\phi}_m(\mathbf{k}_\perp) = \frac{i\pi\mu_0 M_s t}{\Phi_0}\left(\frac{\tilde{m}_x k_y - \tilde{m}_y k_x}{k_\perp^2}\right) \tag{2.6}$$

where $\tilde{m}_x$ is the Fourier transform of the $\hat{\mathbf{x}}$ vector component of $\mathbf{M}/M_s$, here M_s is the saturation magnetization, and Φ_0 is the magnetic flux quantum. **Note:** In the above equation the Fourier transform is defined with the 2π in the exponent, this is consistent with the paper by Walton *et al.* and with most fft functions.

The following section will discuss how to take this phase and simulate Fresnel contrast LTEM images, as well as the inverse, how to calculate this phase from Fresnel contrast LTEM images.

Streamlined Approach to Mapping the Magnetic Induction of Skyrmionic Materials

Jordan J. Chess[1], Sergio A. Montoya[2,3], Tyler R. Harvey[1], Colin Ophus[4], Simon Couture[2,3]
Vitaliy Lomakin[2,3], Eric E. Fullerton[2,3] and Benjamin J. McMorran[1]

[1] Department of Physics, University of Oregon, Eugene, OR

[2] Center for Memory and Recording Research, University of California, San Diego, CA

[3] Department of Electrical and Computer Engineering, University of California, San Diego, La Jolla, CA

[4] National Center for Electron Microscopy, Molecular Foundry, Lawrence Berkeley National Laboratory, Berkeley, California

30 June, 2017

Introduction to Streamlined Approach to Mapping the Magnetic Induction of Skyrmionic Materials

Magnetic skyrmions are particle-like solitons or magnetic bubbles in a magnetization texture that have topologically non-trivial spin textures[14]. The stability of skyrmions and the low current density necessary to move them[24] has inspired many suggested applications that employ skyrmions as bits in both memory and logic devices which are predicted to be highly energy-efficient[25, 26, 27, 28, 29, 30]. These magnetic quasi-particles were initially identified only at low temperatures in non-centrosymmetric crystals including MnSi[10, 31], FeCoSi[32] and FeGe[33], but recent observations have shown that skyrmions can be stabilized in a more diverse class of materials including films with perpendicular magnetic anisotropy (PMA)[30, 34, 35, 36, 37, 38]. This larger swath of materials suggests the need for more rapid characterization techniques to both facilitate the efficient search for materials suitable for applications in skyrmionic devices and explore the basic physics of these magnetic textures.

Lorentz transmission electron microscopy (LTEM) is one of a very few techniques for providing direct real space images of magnetic features at the nanoscale. Recent improvements in aberration correction and instrument stability have led to a new resolution benchmark of 1 nm for scanning LTEM[39]. Additionally, new tomographic reconstruction algorithms have led to the demonstration of 3D vector field electron tomography by Phatak *et al.* [40]

Most of the LTEM studies of skyrmion materials have employed analysis based on the transport of intensity equation (TIE),[20, 41] an equation that relates the z-derivative of the image intensity to the phase shift of an electron. This approach yields quantitative maps of the local in-plane magnetic induction integrated through the sample thickness, but requires multiple images (under-, in-, and over-focused) be taken at a specific point of interest in the sample[20]. In a post-processing step these images are first aligned and then used to approximate the z-derivative of the image intensity. In order to maximize the final field of view, the microscopist must carefully align the microscope to minimize image movement between images recorded at different focus values. These alignments can be sensitive to changes in other experimental parameters including magnetic field applied to the sample. This, coupled with the need to properly align images which can be difficult to automate[42], increases the total time needed to extract useful information from a magnetic sample. This often makes certain experiments prohibitively time-consuming, such as determining the in-plane magnetic induction during an *in-situ* applied field sweep (although this type of study does exists in the LTEM literature[43, 44]). One approach, differential phase imaging[45], developed by Pollard *et al.* maps the change in magnetic state during a dynamic measurement, this approach can be applied to non-uniform films. Alternatively, one can forego mapping the magnetic induction and instead answer questions that depend only on the location of domain walls, which can in general be accomplished with a single defocused image. This method has been used to determine the non-adiabatic spin torque parameter[46], image domain wall nucleation[47], and record skyrmion motion[13]. Additionally, Phatak *et al.*, showed that both the polarity and chirality of a vortex magnetization pattern of a magnetic disk can be determined from a single Fresnel contrast image of a tilted sample[48].

Similar to the work by Eastwood *et al.*[49] or Koch[50], in which they present iterative algorithms for single image phase reconstruction, here we show that one defocused image is sufficient to determine the magnetic portion of the electron phase shift of a uniform film using a simplified TIE approach. This allows one to map the magnetic induction without the trade-off of a slower, more involved focal series experiment, making it ideal for *in-situ* experiments on suitable samples. Figure 3 shows an application of the single image TIE approach we are discussing here, applied to an [Gd (0.4 nm)/Fe (0.36 nm)] × 80 multilayered film[37, 51], under quasi-dynamic conditions. The data were taken as an applied perpendicular magnetic field was swept from a field strong enough to saturate the sample to a slightly negative applied field. The data show skyrmions (black/white circles), worm domains, and bubbles with zero topological charge (elliptically shaped) nucleating as the field strength is reduced. These features then evolve during the field sweep into a mixture of skyrmions and labyrinth domains. The top two images (a,b) are the under-focus LTEM image and reconstructed magnetic induction with Δf=-300 µm, and applied field H_z= 180 mT, while (c) and (d) are the under-focus and magnetic induction at H_z= 70 mT.

Additional algorithms for single-image phase retrieval or exit-wave reconstruction exist but require specific sample geometries such as an isolated object[52], or specific illumination conditions and a diffraction image[53, 54] which make them not suitable

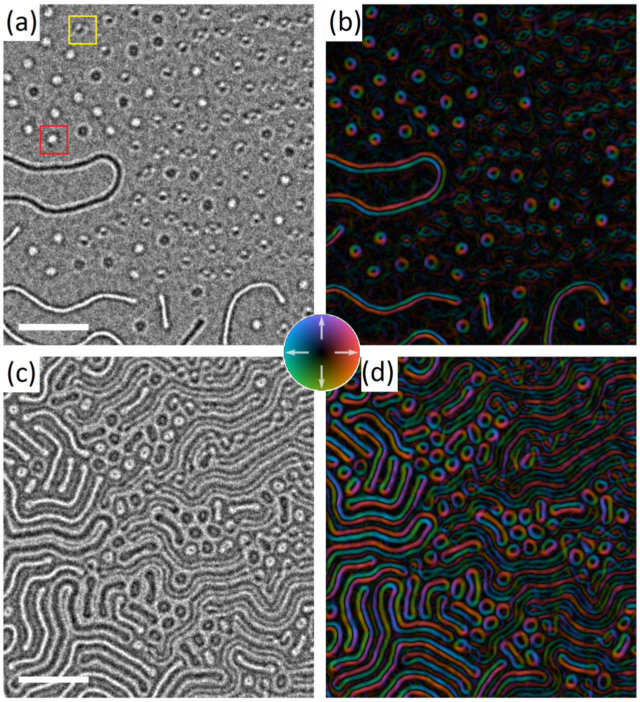

FIGURE 3. Example use of single image TIE
(a) and (c) Selected under-focused Lorentz TEM images from a field sweep performed on a Fe/Gd multilayered thin film with (a, b) 180 mT and (c, d) 70 mT field applied perpendicular to the film. Scale bar is 1 µm. (b), (d), The magnetic induction calculated using our single image analysis on the image to the left (hue and saturation of color indicate the direction and magnitude of the magnetic induction). See supplemental material video for full field sweep.

for this type of sample or difficult to implement in a TEM. It is worth emphasizing that the general paradigm for these single image phase retrieval algorithms is to use *a priori* knowledge to simplify the analysis, which in practice usually means restricting oneself to a subset of samples. In this case we are choosing to restrict our analysis to uniform thin magnetic films, which can be treated as pure magnetic phase objects. Utilizing our new approach, the full in-plane magnetic induction can be determined for each image in a quasi-dynamic measurement with no extra experimental requirements and fewer post-processing steps. This fuller understanding is often required to interpret the LTEM images of the complex magnetization textures present in skyrmionic materials.

Theory

The phase imparted on an electron plane wave traveling along the z-axis after transmission through a sample with electric potential V and vector potential $\mathbf{A}$ is given by the Aharonov-Bohm phase shift[55]:

$$\begin{aligned}\phi(\mathbf{r}_\perp) &= C_E \int_L V(\mathbf{r}_\perp, z)\,\mathrm{d}z - \frac{\pi}{\Phi_0}\int_L \mathbf{A}(\mathbf{r}_\perp, z)\cdot \mathrm{d}\mathbf{r} \\ &\equiv \phi_e + \phi_m\end{aligned} \tag{2.7}$$

where L is a path parallel to the propagation direction of the electron beam, $\mathbf{r}_\perp$ is the location in the sample plane, C_E is the interaction constant[20], and Φ_0 is the magnetic flux quantum. If we assume a homogeneous foil of uniform thickness d and constant mean inner potential (V_0) the electrostatic term can be easily evaluated and yields,

$$\phi_e = C_E V_0 d$$

Additionally, the effects of inelastic scattering and high angle scattering of electrons out of the optical system can be described by an exponential drop in the initial amplitude of the electron wave function. Thus, assuming parallel illumination, the complex amplitude exiting the foil is,

$$\psi_0(\mathbf{r}_\perp) = A e^{-\alpha d} e^{i C_E V_0 d} e^{i \phi_m(\mathbf{r}_\perp)}. \tag{2.8}$$

The intensity of the wave at the image plane using the microscope transfer function ($\mathcal{T}(\mathbf{q}_\perp)$) is then given by,

$$I(\mathbf{r}_\perp, \Delta f) = \left| \mathscr{F}^{-1} \left\{ \mathscr{F}[\psi_0(\mathbf{r}_\perp)] \mathcal{T}(\mathbf{q}_\perp) \right\} \right|^2 \tag{2.9}$$

where $\mathbf{q}_\perp$ are the in-plane spatial frequencies. A relevant transfer function that models the effects of spherical aberration (C_s) and a damping envelope ($E_s(q_\perp)$) due to a spread in illumination angles caused by lens instabilities is:

$$\mathcal{T}(\mathbf{q}_\perp) = a(|\mathbf{q}_\perp|) e^{-i\chi(q_\perp)} e^{-E_s(q_\perp)} \tag{2.10}$$

where $a(q_\perp)$ is an aperture function, the phase transfer function $\chi(q_\perp)$ is described by,

$$\chi(q_\perp) = \pi \lambda \Delta f q_\perp^2 + \frac{1}{2} \pi C_s \lambda^3 {q_\perp}^4 \tag{2.11}$$

and $E_s(q_\perp)$ given in terms of the divergence angle Θ_c is[22],

$$E_s(q_\perp) = \left(\frac{\pi \Theta_c}{\lambda} \right)^2 \left(C_s \lambda^3 q_\perp^3 + \Delta f \lambda q_\perp \right)^2 \tag{2.12}$$

Above, λ is the relativistic electron wavelength, Δf is the distance from the in-focus plane, and we have used $q_\perp \equiv |\mathbf{q}_\perp|$ for notational convenience. Before continuing we stop to note that conventional TIE analysis presumes both of the blue terms in equations (2.11) and (2.12) are negligible. This is generally a reasonable assumption because of the large defocus values used in LTEM, for example see Figure 4. As will be discussed, our method neglects one additional term (the last term in equation (2.12)). For completeness and accuracy the full transfer function (eq. (2.10)) was used in all image simulations.

Taylor expanding the transfer function for small $q_\perp$, the "paraxial approximation", we arrive at an approximate form of equation (2.9)[56],

$$\begin{aligned} I(\mathbf{r}_\perp, \Delta f) \approx I_0 &- \frac{\lambda \Delta f}{2\pi} \nabla_\perp \cdot (I_0 \nabla_\perp \phi_m) \\ &+ \frac{(\pi \Theta_c \Delta f)^2}{2} [\sqrt{I_0} \nabla_\perp^2 \sqrt{I_0} - I_0 (\nabla_\perp \phi_m)^2] \end{aligned} \tag{2.13}$$

here $I_0 = |\psi_0(\mathbf{r}_\perp)|^2$. Examining equation (2.8) we see that if we are analyzing homogeneous thin film specimens with a uniform thickness, which includes many materials, then I_0 becomes a constant, as shown, for example in Figure5.b. We emphasize that this technique can only be applied to regions that have no amplitude or diffraction contrast in the in-focus image. The amorphous material shown in this paper meets this criterion, as do many magnetic thin film materials. And equation (2.13) simplifies to,

$$\begin{aligned} I(\mathbf{r}_\perp, \Delta f) \approx I_0 \bigg(1 &- \frac{\lambda \Delta f}{2\pi} \nabla_\perp^2 \phi_m \\ &- \frac{(\pi \Theta_c \Delta f)^2}{2} (\nabla_\perp \phi_m)^2 \bigg) \end{aligned} \tag{2.14}$$

As shown by De Graef *et al.*[56] the transport of intensity equation can be obtained from (2.14) by simply subtracting the value at $I(\mathbf{r}_\perp, \pm\Delta f)$ yielding,

$$\begin{aligned}\nabla_\perp^2 \phi_m &= -\frac{2\pi}{I_0\lambda}\frac{I(\mathbf{r}_\perp, \Delta f) - I(\mathbf{r}_\perp, -\Delta f)}{2\Delta f} \\ &\approx -\frac{2\pi}{I_0\lambda}\frac{\partial I}{\partial z}.\end{aligned} \tag{2.15}$$

In this way, the Laplacian of the phase can be derived from two different images of the specimen recorded under different focal conditions. Equation (2.15) is the standard equation used in analyzing LTEM data. Note that a crucial step in standard use of TIE analysis is the calculation of the difference between two images (Eq. (2.15) RHS). Thus, the reconstructed magnetic phase is subject to errors introduced when acquiring images under different conditions including: drift, rotations, and changes in magnification.

Here we suggest that due to the high spatial coherence of modern field emission microscopes (Θ_c in the range $(0.01 - 0.08)$mrad[20, 22, 50]), the effects of the last term in equation (2.14) are negligible at the medium resolutions used for LTEM. We present Figure 5 as evidence of the above statement. Additionally, the validity of this approximation and its implications are discussed in detail in the supplementary material as well as the effects of noise.

This simplification results in a Single Image Transport of Intensity Equation (SITIE),

$$\nabla_\perp^2 \phi_m \approx \frac{2\pi}{\lambda\Delta f}\left(1 - \frac{I(\mathbf{r}_\perp, \Delta f)}{I_0}\right). \tag{2.16}$$

One then needs to determine a value for I_0, which is given by the average of the out-of-focus image due to the preservation of electron flux[50]. Alternatively, one can arrive at equation (2.16) by simply starting with the TIE equation, assuming the object in question is a pure phase object, and using $I(\mathbf{r}_\perp, \Delta f) - I_0$ as a first order $\mathcal{O}(\Delta f)$ approximation to $\partial I/\partial z$. Here we chose to present a more involved derivation to make clear what was being neglected when making this first order approximation of the derivative, when compared to the more traditional $\mathcal{O}(\Delta f^2)$ approach used in equation (2.15).

Multiple techniques have been developed to solve the standard TIE equation including a Fourier-based approach[57], a multigrid algorithm[58], a symmetrized version of the Fourier method[59], and finite element method[60], all of which can also be applied to the SITIE to determine the phase of the exit wave. From this phase the local magnetic induction can easily be determine using the relation,

$$\nabla_\perp \phi_m(\mathbf{r}_\perp) = -\frac{e}{\hbar}[\mathbf{B}(\mathbf{r}_\perp) \times \hat{\mathbf{e}}_\mathbf{z}]d \tag{2.17}$$

where $\hat{\mathbf{e}}_\mathbf{z}$ is a vector parallel to the beam propagation direction.

Methods

Micromagnetic simulations

To validate SITIE and quantify the errors associated with this method, we simulated through-focal series images of an exactly known, simulated magnetization textures. These micromagnetic textures were obtained from Landau-Lifshitz-Gilbert simulations calculated using the FastMag solver[61]. The micromagnetic simulation is for a $2\,\mu\mathrm{m} \times 2\,\mu\mathrm{m} \times 80\,\mathrm{nm}$ ferromagnetic film, using experimentally measured values for the saturation magnetization ($M_s = 0.4\,\mathrm{A\,\mu m^{-1}}$), anisotropy constant ($\mathrm{K} = 4 \times 10^4\,\mathrm{J/m^3}$), Gilbert damping ($\alpha = 0.05$), and exchange stiffness ($A_{ex} = 5 \times 10^5\,\mathrm{J/m}$). An applied perpendicular magnetic field of $H_z = 0.2\,\mathrm{T}$ was used, and

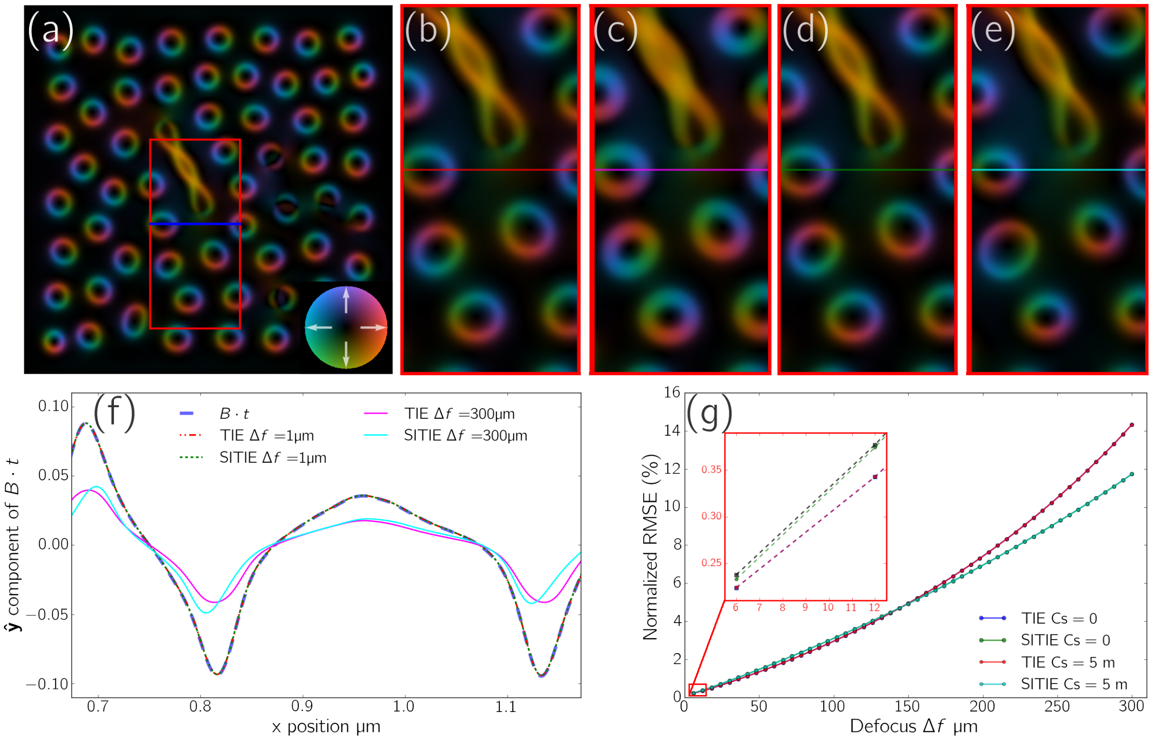

FIGURE 4. Numerical comparison of TIE and SITIE **Simulations** (a) Plot of in-plane components of the local magnetic induction calculated from output of a micromagnetic simulation (color indicates direction and magnitude of the field). (b-e) Local magnetic induction of the region shown in the red box in (a), calculated using conventional TIE with $\Delta f = 1\,\mu\text{m}$ and $\Delta f = 300\,\mu\text{m}$ for (b) and (c) respectively. The red box has a 0.5 μm width. SITIE-calculated magnetic induction for (d) $\Delta f = 1\,\mu\text{m}$ and (e) $\Delta f = 300\,\mu\text{m}$. Notice that only slight distortion errors are present in the $\Delta f = 300\,\mu\text{m}$ cases, caused by using a focus outside of the validity of the paraxial approximation. (f) y-component of the magnetic induction along the colored lines in images (a-e), note the nearly perfect agreement between the reference, TIE, and SITIE for the $\Delta f = 1\,\mu\text{m}$. (g) Plot of the total normalized root mean square error in the determination of $B \cdot t$ calculated using equation (2.18) as function of defocus for TIE and SITIE showing there is no practical difference between the methods for moderate defocus. For these simulations Θ_c was set at 5×10^{-5} rad. The inset shows that for any Δf larger than 10 μm the effects of including a non-zero C_s are truly negligible.

the system is allowed to relax to an equilibrium state in 10 ns. These parameters result in the in-plane magnetic induction pattern shown in Figure 4.a.

Lorentz Image Simulations

Fresnel-contrast LTEM images were simulated using the Mansuripur algorithm: the magnetic phase shift imparted on the electron wave by the results of the micromagnetic simulation was calculated and then equation (2.10) was used to propagate the wave to a given defocus plane[23]. The electrostatic phase shift was neglected in the simulations, in line with the theory above, as it only contributes an overall constant phase and doesn't contribute to the image intensity. Prior to applying the Mansuripur algorithm the output of the FastMag simulations were expanded from 200×200 arrays to 2048×2048, and then padded with zeros to a total array size of 4096×4096 to mitigate the introduction of any artifacts from the Fourier-based approach used in both the Mansuripur algorithm and transfer function formalism. The parameters used for image simulations were: accelerating voltage 300 kV, defocus values $\Delta f = 1\,\mu\mathrm{m} - 300\,\mu\mathrm{m}$, and spherical aberration $C_s = 0 - 5\,\mathrm{m}$. These values more than cover the range encountered in both standard and aberration-corrected microscopes during an LTEM experiment. The normalized root mean square error is used as a metric to compare the reconstructed phase to the known phase calculated as,

$$\mathbf{NRMSE} = \frac{\sum_{i=0}^{i=1} \sqrt{\frac{\sum_{m,n}\left((\tilde{\mathbf{B}}t)_{n,m} - (\mathbf{B}t)_{n,m}\right)^2}{nm}}}{(\mathbf{B}t)_{\max} - (\mathbf{B}t)_{\min}} \times 100\% \tag{2.18}$$

where $\tilde{\mathbf{B}}$ is the TIE/SITIE reconstructed local magnetic induction, $\mathbf{B}$ is the known magnetic induction, t the sample thickness, (m, n) the array indices, and $(i = 0, 1)$ the components of the vector.

Evaluation of SITIE

Numerical evaluation

To quantitatively analyze the validity of SITIE compared to TIE, we numerically simulated Fresnel-contrast images from simulated domain structures obtained from the micromagnetic simulation. This allows us to compare the two phase retrieval methods in the absence of noise or any misalignments in images that could cause errors in standard TIE analysis. Additionally, it gives us a known reference to quantify results that is not present when analyzing experimental data. The Fourier transform-based method of solving the transport of intensity equation was utilized to reconstruct the phase of both the experimental and simulated data[20, 62]. A comparison of the two methods applied to experimental data is left to the next Subsection 2.7.

Figure 4.(b-e), show the calculated local magnetic induction from both TIE (b,c) and SITIE (d,e) each under two different focal conditions; the first (b,d) from a small defocus (1 µm) and the second from a large defocus value (c,e) (300 µm). Notice the close agreement between the reference and both TIE and SITIE for small defocus (FIG.4.a,b,d), which have a normalized root mean square error (NRMSE) of 0.169 % and 0.170 % respectively. Interestingly, for the large defocus (300 µm) examples (figure 4.e,f) the error associated with TIE (14.3 %) is larger than that for SITIE (11.7 %). These results can be understood analytically from the right hand side of equations (2.15) and (2.16). They are the central and forward difference approximations for the z-derivative of the image intensity, and have associated errors of order $\mathcal{O}(\Delta f^2)$ and $\mathcal{O}(\Delta f)$ respectively. This quadratic versus linear error is evident in Figure 4.g. Also, evident in Figure 4.g is the well-known fact that for all but

the smallest defocus values used in LTEM, the effects of spherical aberration are negligible[20].

Experimental evaluation

To ensure the validity of SITIE on real data, we collected and analyzed through-focal series images of magnetic bubble domains in a thin film sample. The images were collected using an FEI Titan equipped with a Lorentz lens and integrated CEOS objective lens aberration corrector. The standard objective lens was partially excited to apply a magnetic field perpendicular to the sample plane. The sample is nominally a [Gd (0.4 nm)/Fe (0.34 nm)] × 80 multilayered film deposited by DC magnetron sputtering onto 50 nm Si_3N_4 membrane with 20 nm Ta seed and capping layers[37].

Prior to analysis all experimental images were filtered following the method suggested by Tasdizen *et al.* to remove low-frequency artifacts caused by slightly non-uniform illumination[63]. Figure 5 shows the focal series (a-c) for Δf = (-300,0,300 µm). The left column shows (d) the phase reconstructed using conventional TIE analysis applied to (a-c), (e) the magnetic induction determined using the phase in (d) represented with color indicating the magnitude and direction of the magnetic induction and (f) giving a closer look at the region inside the red square in (e). The right column shows the phase (g) and magnetic induction (h,i) all determined using only image (a). Included in the images are skyrmions, four of which have helicity $\gamma = \pi/2$ (white circles in phase images), and five with $\gamma = -\pi/2$ with γ defined the same as equation B3 in reference ([14]). The remaining features are stripe domains starting to break up into topologically trivial bubbles, and skyrmion bound pairs[37]. It is important to note that the slightly lower signal-to-noise present in Figure 5.g is not an inherent difference between SITIE and TIE, but instead a consequence of Figure 5.g having half the effective exposure time due to it being calculated from

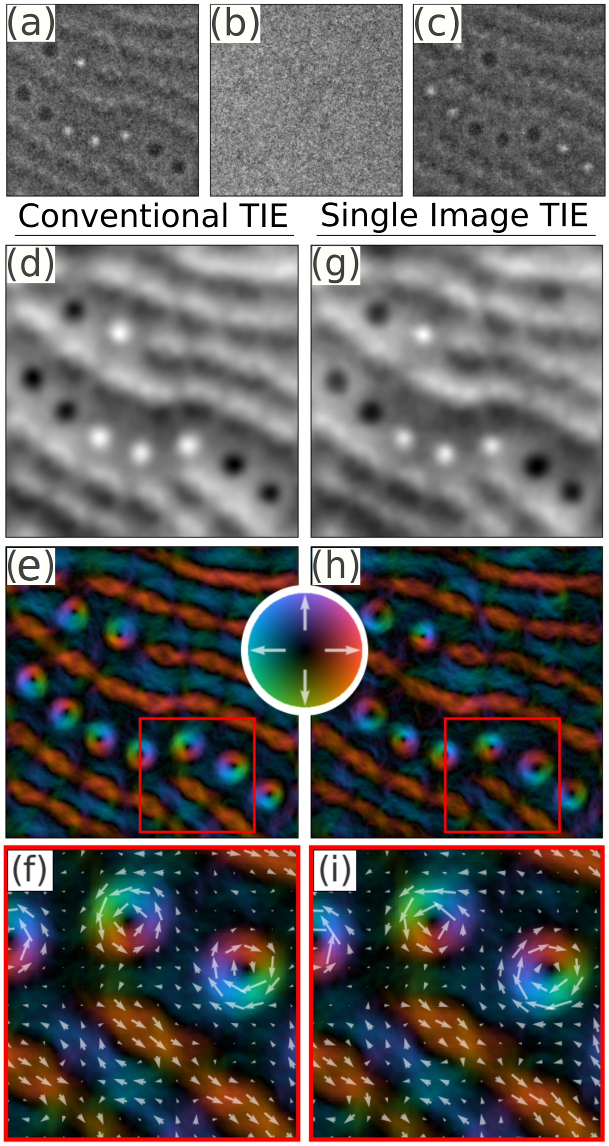

FIGURE 5. Experimental comparison of TIE and SITIE
(a-h) Experimental Lorentz TEM analysis of a Fe/Gd multilayered thin film over the same 1.5 µm field of view. (a) Under-focused, (b) in-focus, and (c) over-focused images showing Fresnel-contrast ((a,c) recorded at $\Delta f = \pm 300\,\mu\text{m}$). (d) Phase calculated using the standard TIE applied to image (a-c). (g) Phase calculated using only image (a). (e), (h), The magnetic induction calculated from phase above. (f), (i) Enlarged area from boxed region in (e), (h) with magnetization represented both by color and vector arrows.

only one image. This could easily be overcome by increasing the exposure time for images collected for SITIE, or by collecting multiple shorter exposures images aligning and averaging them latter. We emphasize here that aligning images collected at the same focus value can be accomplished using simple algorithms such as cross-correlation and is significantly easier than aligning images at different foci, because of the associated reversals in contrast, rotation, and distortions between images. Errors in image alignment caused by pixel shift, magnification changes, and rotations can cause significant errors in the reconstructed phase when performing TIE analysis. For a detailed discussion of this subject we refer the reader to chapter 5.3.2 of De Graef and Zhu [20]. SITIE is free of all these errors.

Conclusion

We have demonstrated, both numerically and experimentally, that a single Lorentz TEM image can appropriately be used to map the magnetic phase of uniform samples, specifically for thin films exhibiting skyrmionic phase. This simplified TIE approach gives roughly equivalent results to conventional TIE analysis. Using SITIE analysis on uniform samples simplifies both the computational load and data collection involved in characterizing topological magnetization textures. Furthermore, this simplification opens the door to exploring new phenomenon that was previously impractical with the traditional TIE analysis by: removing the need to align and collect multiple images, and reducing errors caused by distortions in images. This simplified technique allows for phase reconstruction during quasi-dynamic measurements (e.g. field and/or temperature sweeps), and gives a potential route to ultra-fast LTEM studies.

Practical considerations of SITIE

To understand the potential artifacts that can be present in the magnetic induction when using the SITIE, when compared to TIE, we will examine equation (2.14) of the main text in more detail. By substituting equation (2.14) into equation (2.16) and applying an inverse Laplace operator to both sides we can relate the reconstructed phase (ϕ_r) to the actual phase (ϕ_0).

$$\phi_r(\mathbf{r}_\perp) = \phi_0(\mathbf{r}_\perp) + \frac{\pi^3\Theta_c^2\Delta f}{\lambda}\nabla_\perp^{-2}\left[(\nabla_\perp\phi_0(\mathbf{r}_\perp))^2\right] \tag{2.19}$$

Equation (2.19) indicates that to maximize the accuracy of the reconstructed phase one can increase the coherence, decrease the defocus, or increase the wavelength of the illumination. In general Δf is the most tunable parameter in an experiment. Typical values for Θ_c used in the literature range from $(0.01 - 0.08)$mrad[20, 22, 50]. Obviously, minimizing the prefactor of the second term will increase the accuracy of the reconstructed phase, but how small it needs to be will depend on the functional form of $\phi_0(\mathbf{r}_\perp)$. In LTEM we are primarily interested in measuring the local magnetic induction using equation (11), so here we actually care about the gradient of equation (2.19),

$$\begin{aligned}\nabla_\perp\phi_r(\mathbf{r}_\perp) =& \nabla_\perp\phi_0(\mathbf{r}_\perp) + \frac{\pi^3\Theta_c^2\Delta f}{\lambda}\nabla_\perp\left(\nabla_\perp^{-2}\left[(\nabla_\perp\phi_0(\mathbf{r}_\perp))^2\right]\right)\\ =& \nabla_\perp\phi_0(\mathbf{r}_\perp)\left(1 + \frac{\pi^3\Theta_c^2\Delta f}{\lambda}\frac{\nabla_\perp\left(\nabla_\perp^{-2}\left[(\nabla_\perp\phi_0(\mathbf{r}_\perp))^2\right]\right)}{\nabla_\perp\phi_0(\mathbf{r}_\perp)}\right)\end{aligned} \tag{2.20}$$

The criterion for valid use of SITIE is that the value in the parenthesis to be as close to 1 as possible. This final term is quite opaque, and is the main reason why multiple authors have advocated for the use of over- and under-focused images equidistant from the in-focus plane[64, 65]. To gain insight into this term we examine a simple helical domain, with magnetization given by,

$$\mathbf{M}(x) = M_s(\cos(x/\delta)\hat{y} + \sin(x/\delta)\hat{z}) \tag{2.21}$$

with M_s the saturation magnetization and δ roughly corresponding to the domain/domain wall width. The magnetic phase shift in this case for a sample of uniform thickness d is then given by,

$$\phi_0(\mathbf{r}_\perp) = -\frac{2\pi^3 d\, M_s \mu_0 \delta}{\Phi_0} \sin(x/\delta) \tag{2.22}$$

making,

$$\nabla_\perp \left(\nabla_\perp^{-2} \left[(\nabla_\perp \phi_0(\mathbf{r}_\perp))^2 \right] \right) = -\frac{\pi^4 d^2 M_s^2 \mu_0^2 \delta}{\Phi_0^2} \sin(2x/\delta). \tag{2.23}$$

We can then determine the required defocus for this specific case from the following relation,

$$1 \gg \frac{\pi^5 \Theta_c^2 \Delta f\, d\, M_s \mu_0 \delta}{\lambda \Phi_0} \sin(x/\delta). \tag{2.24}$$

From which we can conclude that the reconstructed magnetic induction will be most accurate when the in-plane field is at its peak and, least accurate where the in-plane field is weakest. For reference for the following parameters ($\Theta_c = 0.01\,\mathrm{mrad}$, $d = 80\,\mathrm{nm}$, $\Delta f = 100\,\mu\mathrm{m}$, $M_s = 0.4\,\mathrm{A}\,\mu\mathrm{m}^{-1}$, $\delta = 10\,\mathrm{nm}$, $\lambda = 2\,\mathrm{pm}$), the prefactor is 0.2976. It is interesting to note that the magnitude of this error is linear with the domain wall width meaning it is more accurate for smaller features. This of course should be applied with some caution for two reasons: first the global effect of $E_s(q_\perp)$ is to attenuate high spatial frequencies (see Figures 7, 8), second at sufficiently small length scales a uniform form film can in no way be approximated with a constant electrostatic phase shift or zero intensity contrast because eventually you will run into thickness fluctuations or the inherent atomic structure.

The preceding analysis indicates that in order to minimize the error in the reconstructed phase one should employ the smallest possible defocus. Of course Δf cannot be decreased indefinitely, due to the presence of noise, as lower Δf means lower signal. A detailed analysis of the effects of noise on TIE analysis was done by Paganin *et al.*[66] a similar approach applied to SITIE yields bounds on Δf,

$$\frac{2\pi\sigma}{\lambda I_0\langle\nabla_\perp^2\phi\rangle_{RMS}} \ll \Delta f \ll \sqrt{\frac{\lambda I_0\langle\nabla_\perp^2\phi\rangle_{RMS}}{2\pi\left\langle\frac{\partial I}{\partial z}\right\rangle_{RMS}}} \tag{2.25}$$

where σ is the standard deviation of the noise distribution and $\langle f\rangle_{RMS}$ indicates the root-mean-square of f. This can be used to as a guide in applying SITIE.

For reference we have simulated images (FIG. 6) of a simple 40 nm sample with $M_s = 0.4\,\mathrm{A\,\mu m^{-1}}$, containing two Bloch walls. This fictitious sample has Bloch walls that vary in width as a function of y such that at the bottom of the image the domain wall width is 10 nm and at the top of the image it reaches 50 nm. This was done to help show the effects of feature size on the performance of each algorithm. The images were simulated assuming a fixed $\Theta_c = 0.01$ mrad, with varying Δf and signal-to-noise (SNR). Here the SNR is defined as the signal mean divided by the standard deviation of the noise. The results of the application of TIE and SITIE to the simulated images in Figure 6 are show in Figure 7 and 8. These results show two effects caused by non-zeros Θ_c first the attenuation of higher spatial frequencies which explains the reduction in the magnitude of the reconstructed magnetic induction for the larger defocus values. The second effect is only present in the results of Figure 8 where we see the effects of the last term of equation (2.14). While all of the above analysis is a useful guide in assessing when SITIE and applied, the most pragmatic method is to try in on a given sample and compare the results to a more established method.

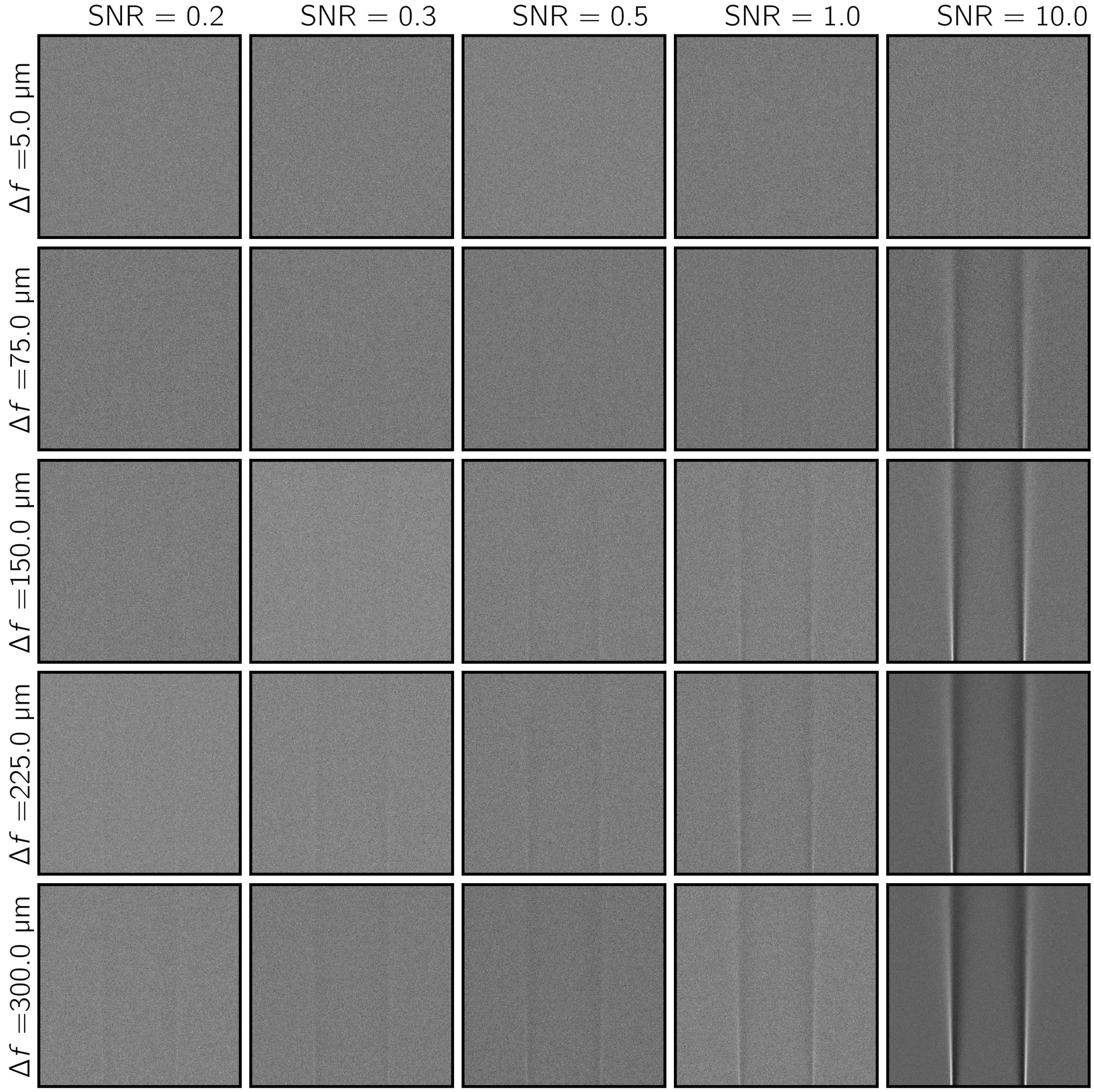

FIGURE 6. Visualization of varying defocus and noise in LTEM data **Simulations** showing LTEM data with varying signal to noise ratio (SNR) and Δf, for a fixed $\theta_c = 0.01\,\text{mrad}$. The intensity of each images is scaled individually to fit the full range of pixel values. The field of view in each image is 1.5 µm.

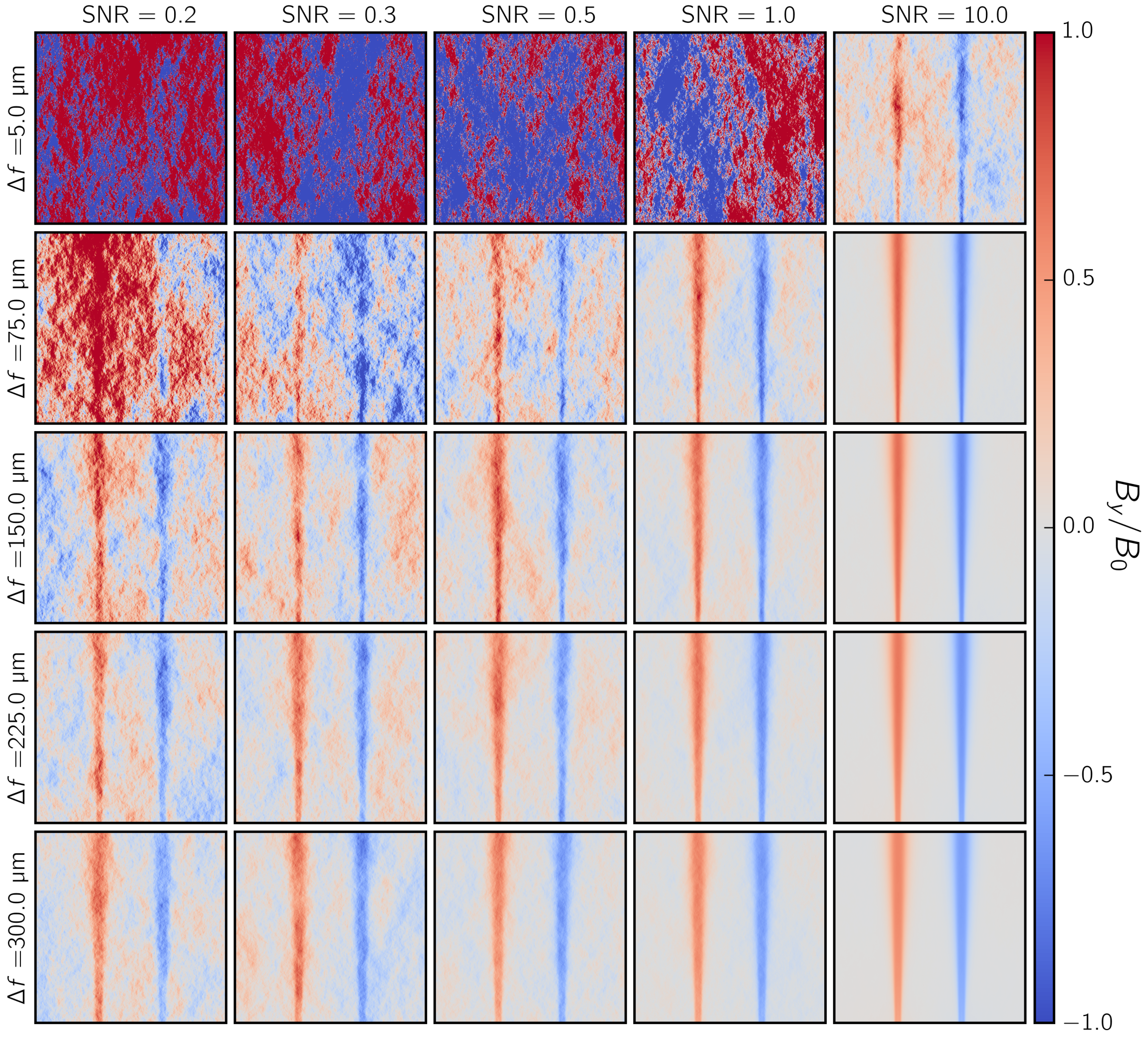

FIGURE 7. Effect of noise and defocus on TIE
Calculated magnetic induction from the data show in Figure 6 and the image on the opposite side of focus (not shown) using standard TIE. The magnetic induction of each image has been normalized by the theoretical value (B_0), and the color scale is clipped at ±1. The field of view in each image is 1.5 µm.

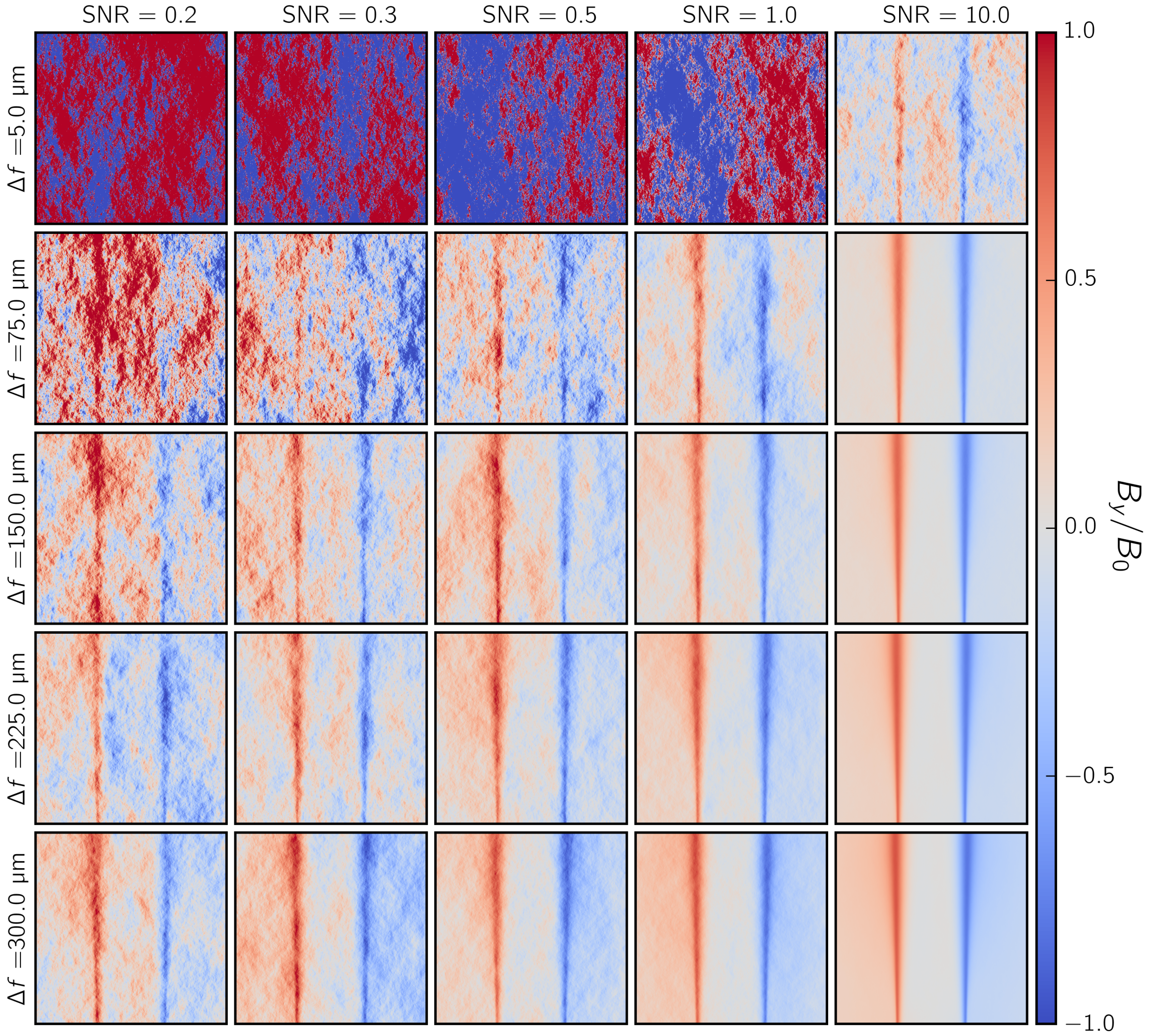

FIGURE 8. Effect of noise and defocus on SITIE

Calculated magnetic induction from the data show in Figure 6 using SITIE. The magnetic induction of each image has been normalized by the theoretical value (B_0), and the color scale is clipped at ±1. The field of view in each image is 1.5 µm.

Chapter Conclusion

In this chapter the basics of LTEM were introduced. A numerical method capable of calculating the phase shift imparted on an electron passing through a magnetic sample was outlined. The transfer function formalism was then used to derive an approximate equation relating the intensity in experimental LTEM images to second order derivatives of the electron phase. An approximate solution to solve for the electron phase was then given. Experimental and simulated data were used to demonstrate the effectiveness of this approach compared to the standard approach found in the literature. Finally, a specific simplified example was given to help guide in the application of our simplified SITIE algorithm.

CHAPTER III

TOPOLOGICAL DEFECTS IN FE/GD

Notes on Manuscripts

The results in this chapter are presented in three previously published articles:

S Montoya, S Couture, **J Chess**, J Lee, N Kent, M-Y Im, S Kevan, P Fischer, B McMorran, and S Roy. *Physical Review B* **95** 224405 (2017),

S Montoya, S Couture, **J. Chess**, J Lee, N Kent, D Henze, S Sinha, M-Y Im, S Kevan, and P Fischer. *Physical Review B* **95** 024415 (2017),

JT Lee, **J Chess**, S Montoya, X Shi, N Tamura, S Mishra, P Fischer, B McMorran, S Sinha, and E Fullerton. *Applied Physics Letters* **109** 022402 (2016),

For all of these articles Sergio Montoya and Eric Fullerton conceived of the project. Sergio Montoya deposited all specimens, measured the bulk magnetic, resonance, MFM, and transport properties. James Lee conducted the RSXS measurements. Simon Couture the LLG simulations. For each article the first author wrote up the initial manuscript with input from all co-authors. This is a large project with multiple authors. I don't want to give the perception of ownership of parts that I didn't play a major role in, so I will avoid telling the full story and will only discuss details and results that I had a significant involvement in or that help with understanding of later chapters. Figures and captions are reproduced verbatim from the original articles.

Skyrmion Phase Diagram

In this chapter we present an investigation into the conditions under which various topological defects can be produced in Fe/Gd multilayers. Each layer in the sample's were deposited with thicknesses <0.4 nm. Fe and Gd antiferromagnetically couple, resulting in a ferrimagnet. This allows us to tune the samples saturation magnetization by varying the alloy composition. By carefully controlling the layer thickness and deposition conditions we are able to induce perpendicular magnetic anisotropy (PMA)[67, 68]. Normally, the requirement for PMA is that the material's Q factor defined as $K/(2\pi M_s^2)$ be greater than unity, where K is the uniaxial anisotropy. Here Q is less than one, but we were able to overcome this requirement by increasing the total film thickness, as previously documented by others[69, 70, 71, 72, 73]. We use this tunability of material parameters as a tool to map out that parameter space for stable topological defects. LTEM and Resonant Soft X-ray Scattering (RSXS) were then used to map the magnetic phase diagram.

The multilayer films were deposited by Sergio Montoya as UCSD, layer by layer by alternating Fe and Gd using sputter deposition at room temperature in ultra high vacuum under 3 mTorr Argon. Each sample had a 5 nm Ta seed/capping layer, to protect against oxidation. The samples were deposited on multiple different substrates, including 50 nm and 200 nm SiN membranes to allow for LTEM and RSXS measurements respectively. LTEM measurements were done at the University of Oregon using the Titan and procedure mentioned in the previous chapter. Analysis of the LTEM images was done using standard TIE (this is because this analysis was done before SITIE was fully developed). Figure 9 shows some of these results at room temperature with varying applied field. RSXS measurements were done at Gd M_5 (1198 eV) and Fe L_3 (708 eV) absorption edge at Beamline 12.0.2 Advanced

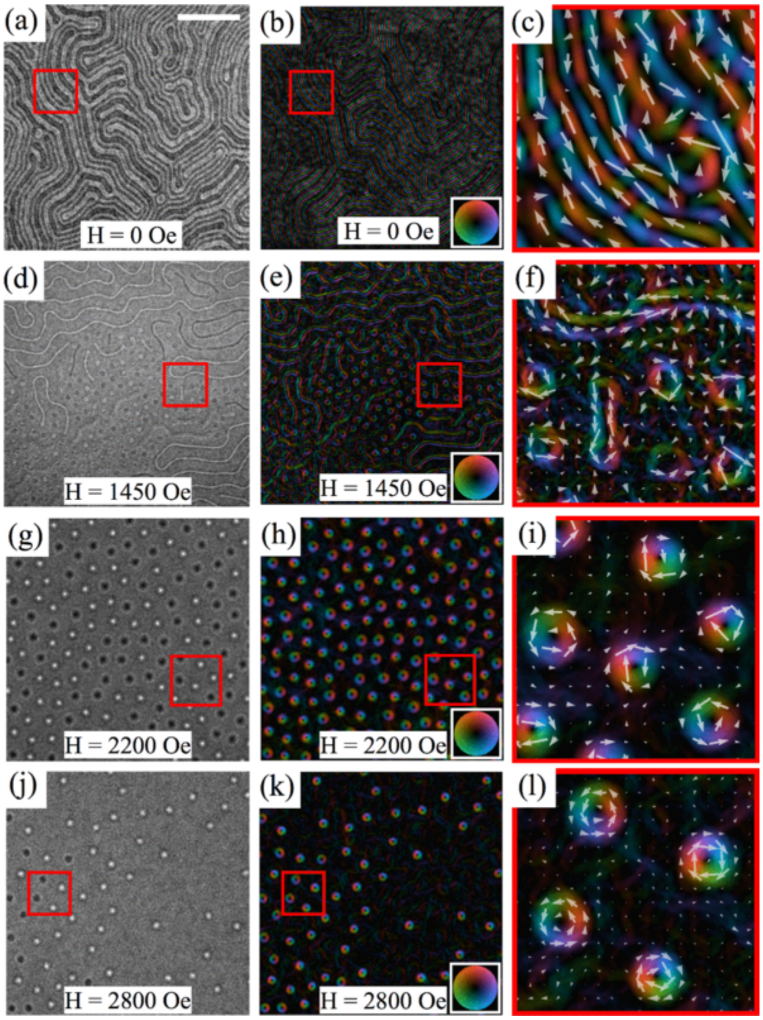

FIGURE 9. Lorentz TEM of FeGd

Real space imaging of the field-dependent magnetic domain morphology of [Fe (0.34 nm)/Gd (0.4 nm)] × 80 Underfocused Lorentz TEM images (first column) measured at room temperature and their corresponding magnetic induction color maps (second column) are detailed. The images are captured as a perpendicular magnetic field is applied from zero field to magnetic saturation. Four different magnetic states are observed as the field is swept, including: disordered stripe domains (a, b), stripe-to-skyrmion transition (d, e), skyrmion lattice (g, h), and disordered skyrmions (j, k). Enclosed regions in the first two columns are enlarged to detail the in-plane magnetic domain configuration using both color and vector magnetic induction maps in the third column (c, f, i, l). The scale bar in (a) corresponds to 1μm.

Light Source, Lawrence Berkeley National Laboratory by James Lee. Figure 10 has examples of RSXS diffraction patterns showing the 4 magnetic phases measurable using this technique. The phase diagram of two sample compositions, determined using a combination of RSXS and LTEM is shown in Figure 11.

Further, micromagnetic numerical simulations were done using Landau Lifshitz Gilbert (LLG) equation, utilizing FASTMAG[61]. These results are in good agreement with both the real and reciprocal space measurements. They also show that the presence of the topological defects in these films can be fully explained without an appeal to DMI. These simulations also predict that the topological defects present in our samples have a more complex structure than what can be observed in LTEM or other transmission based imaging techniques. This is because the numerical simulations predict the presence of Néel caps at the top and bottom of the skyrmions. These caps have opposite magnetization on the top vs the bottom surface, this makes them invisible to transmission based technique because the signal from one side will cancel the signal from the opposite side. This structure can be seen in Figure 12. Additional, resonance data was recorded and compared to LLG simulations that indirectly suggest the presence of these Néel caps. Chapter VI is dedicated to directly detecting this 3D structure.

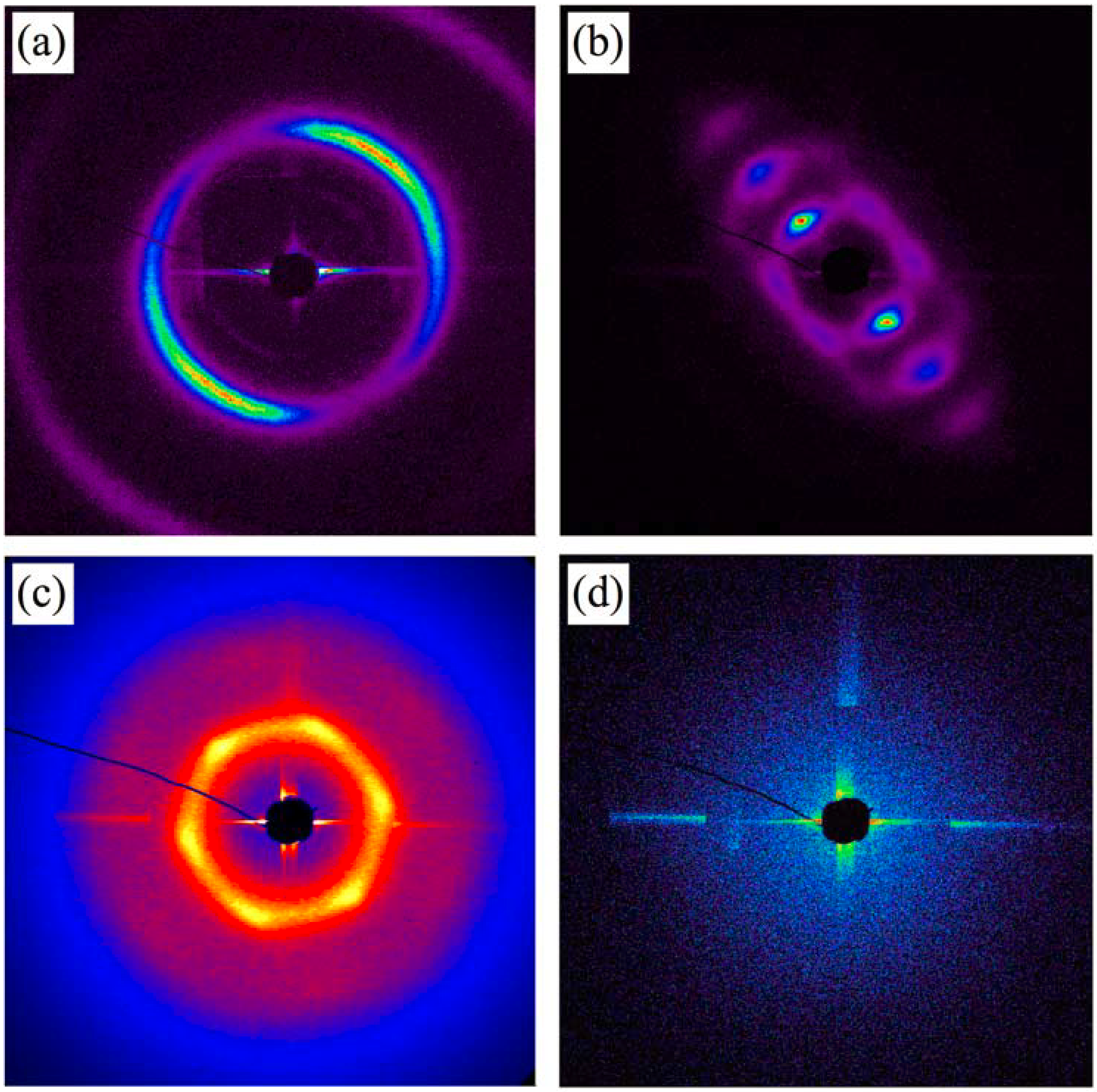

FIGURE 10. Reciprocal space imaging of the magnetic domain morphology The scatter images obtained at room temperature of [Fe (0.34 nm)/Gd (0.4 nm)]× 80 detail the four magnetic phases observable using this technique: (a) disordered stripe domains, (b) coexisting stripes and skyrmions, (c) skyrmion lattice and (d) uniform magnetization. (a) The diffraction image is obtained along the Fe L_3 (708eV) absorption edge at zero-field at 85K. (b, c) These diffraction images are both obtained at room temperature along the Gd M_5 (1180eV) absorption edge at (b) $H_z = 1500$ Oe and (c) $H_z = 1900$ Oe. (d) The saturated state is obtained along the Fe L_3 (708eV) absorption edge at $H_z = 5000$ Oe at room temperature.

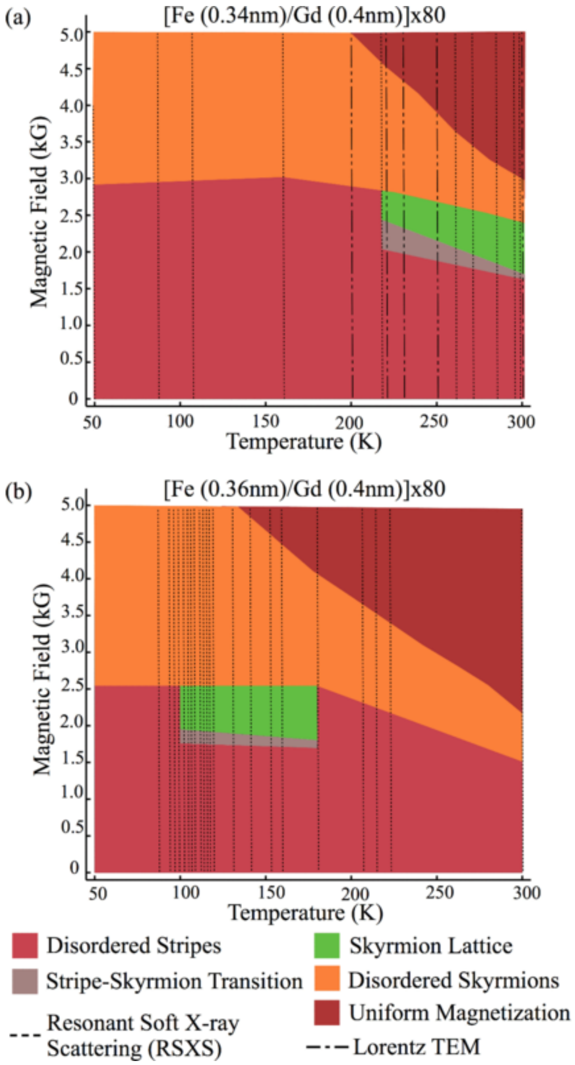

FIGURE 11. Phase Diagram for Fe/Gd

Magnetic field and temperature dependence of the skyrmion phase. The magnetic phase diagrams for two Fe/Gd film structures are shown: (a) [Fe (0.34 nm)/Gd (0.4 nm)] × 80 exhibits a broad skyrmion phase around room temperature, and (b) [Fe (0.36 nm)/Gd (0.4 nm)] × 80 shows a similar skyrmion phase that is shifted to lower temperatures. These magnetic phase maps were constructed using data from four different imaging techniques: resonant soft x-ray scattering, Lorentz TEM, and transmission x-ray microscopy (at room temperature only). The marker lines detail the temperature and imaging technique used to scan the domain morphology.

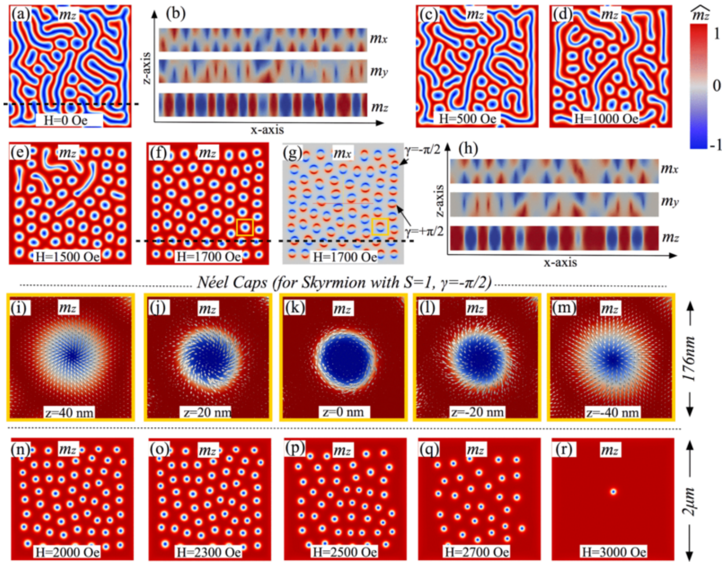

FIGURE 12. Micromagnetic modeling of domain morphology. (a-r) [$M_S = 400$ emu/cm^3, $K = 4 \times 105$ erg/cm^3, and A $= 5 \times 10^7$ erg/cm]. The equilibrium states illustrate the field-dependent domain morphology at several magnetic fields that capture the domain evolution from a stripe to a skyrmion phase. These equilibrium states primarily depict the top side view of the magnetization along the z axis (m_z) at the top surface of the slab ($z = 40$ nm). The magnetization (m_z) is represented by regions in red ($+m_z$) and blue (m_z), whereas the in-plane magnetization (m_x, m_y) is represented by white regions surrounding the blue features. (b, h) Panels illustrating the lateral magnetization components (m_x, m_y, m_z) across the film thickness for the disordered stripe domains in (a) and the skyrmion phase in (f, g) along the dashed line. Inspection along the lateral magnetization reveals a Bloch-like wall configuration with closure domains in both states. The chirality of the skyrmions is depicted in (g) along the top side view of m_x across the center of the slab. (i-m) Detail of the magnetization distribution at different depths (z = 40, 20, 0, 20, 40 nm) for a skyrmion with chirality S = +1, $\gamma = \pi/2$ that is enclosed in a box in (f, g). At each depth, the perpendicular magnetization is represented by blue (m_z) and red ($+m_z$) regions and the in-plane magnetization distribution (m_x and m_y) is depicted by white arrows. The white arrows illustrate how the magnetization of the closure domains and Bloch line arrange at different depths of the slab. (n-r) Detail of the field evolution from ordered skyrmions to disordered skyrmions.

Other Topologically Non-Trivial Magnetization Textures in Fe/Gd

In addition to dipole skyrmions other topological defects are present in the Fe/Gd system. Using RSXS a lattice with symmetry close to the skyrmion lattice was found, but the peaks were slightly asymmetric suggesting a hexagonal lattice with a basis. By using LTEM imaging this basis was determined to be a bound pair of skyrmions, similar to what was seen in $La_{1+2x}Sr_{2\text{-}2x}Mn_2O_7$[38]. These bound skyrmions or biskyrmions are formed by two Bloch skyrmions with like polarity but opposite helicity each having a skyrmion number $S_k = 1$, which then gives the total object $S_k = 2$. By recording LTEM data during a field sweep and applying SITIE to each frame, we were able to develop a model for how to synthesize these bound pairs in the Fe/Gd films. This model is shown schematically in Figure 13, while LTEM of these magnetic textures is show in Figure 14.

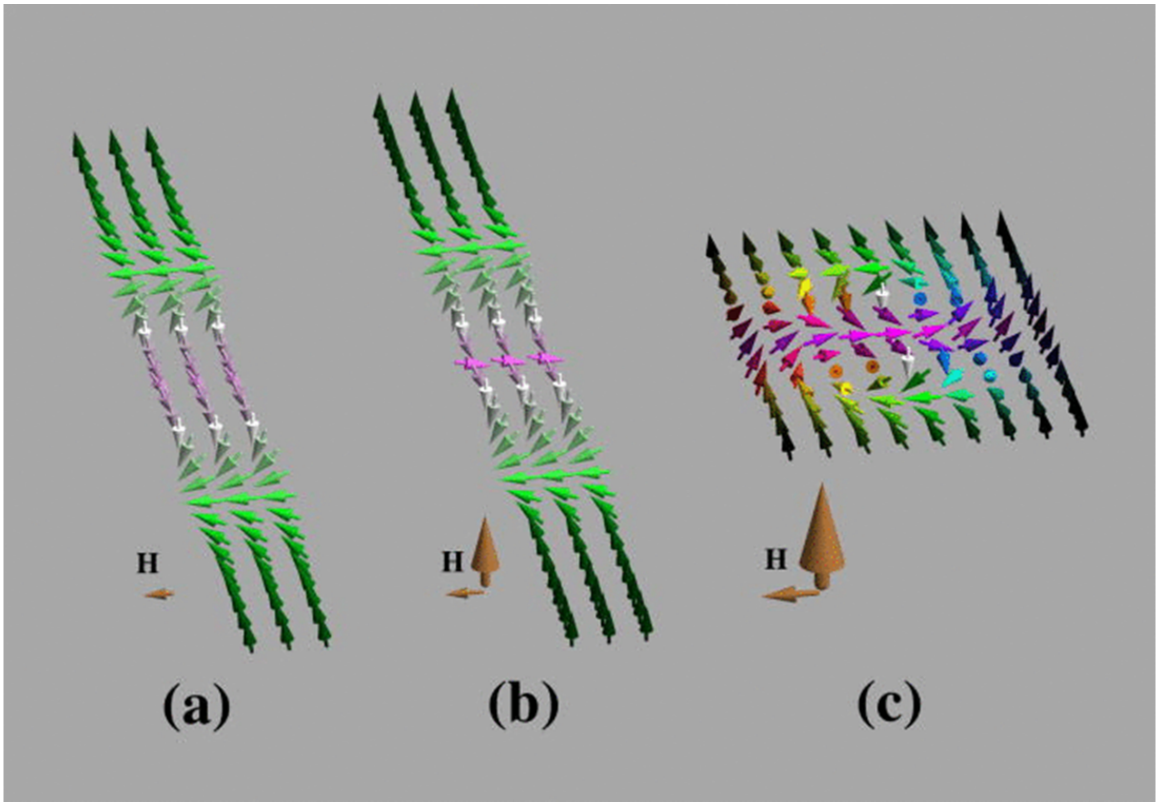

FIGURE 13. Schematic of transition from stripes to bound pairs
Schematic evolution from canted stripes to the skyrmion bound pairs. Color and brightness denote direction and magnitude of spin in-plane component; green and pink have opposite in-plane directions. Brown arrows denote the applied magnetic field, the vertical arrow being the out-of-plane component and the horizontal arrow being the in-plane component. (a) In low fields, up and down stripes are nearly of equal width. The rotational sense of the magnetization switches at the center of these regions. (b) Applied field causes dark green regions to widen, pink regions to narrow, and tilts spins upward. (c) At a critical field, the stripes pinch off into short patches. The dipole fields of these patches cause green spins in parts (a) and (b) to form swirling (multi-hued) spin textures and out-of-plane (white) spins to form the cores of nascent skyrmions.

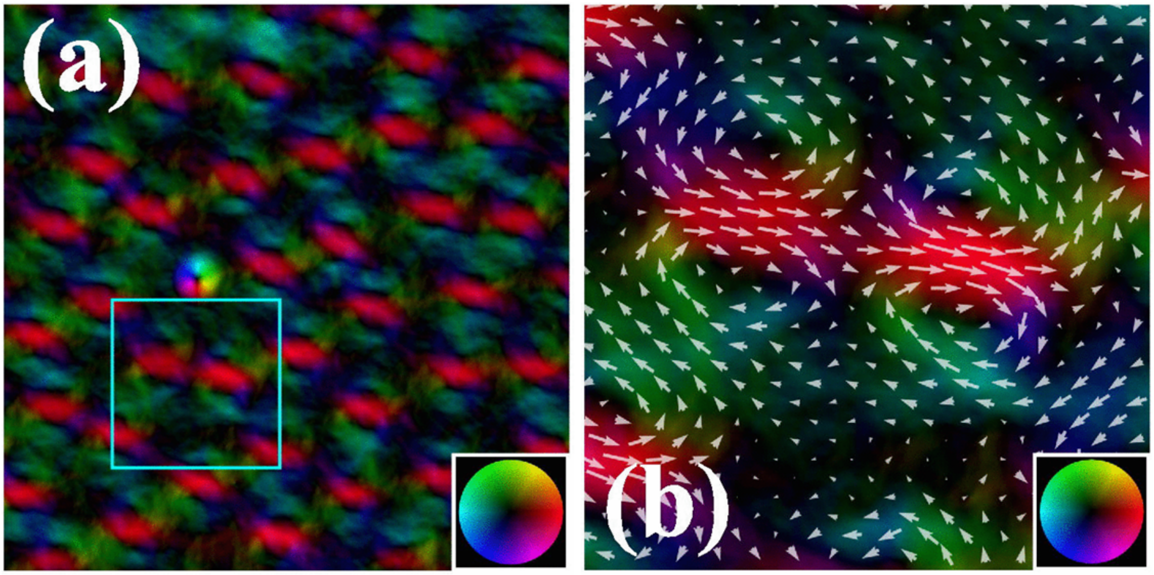

FIGURE 14. LTEM of skyrmion bound pair
In-plane component of magnetic induction (B) of skyrmion bound pairs obtained using the TIE method from LTEM images. Obtained at room temperature and $\mu_0 H$=207mT. The color wheels relate the color to the in-plane orientation of B. (a) Bound pairs are the majority of the objects in the image, with red lines running through their centers. An isolated (circular) unit winding number skyrmion is seen. (b) A vector map of the $0.5\times0.5\mu\text{m}^2$ boxed region in part (a). The B-fields of the top and bottom halves of the bound pair (above and below the red center) have opposite circulations.

Conclusion

In this chapter we have outlined the various topological defects present in Fe/Gd. Additionally, a description of the 3D structure of these dipole-stabilized skyrmions was given. A question that remains to be answered is: is there a mechanism to control the chirality of these magnetic structures? Additional confirmation of the 3D structure of the micromagnetic predicted magnetization is also needed.

CHAPTER IV

DETECTING CHIRAL MAGNETIC DOMAINS

Notes on 'Determination of Domain Wall Chirality Using *in situ* Lorentz Transmission Electron Microscopy'

From Jordan J Chess *et al.* *AIP Advances* **7**, 056807 (2017).

Ben McMorran and I conceived of the measurement technique. Sergio Montoya supplied the samples. Sergio and Eric conceived of the idea to make a sample with Bloch walls and asymmetric layer stacking. I recorded the data, did the analysis, figure creation, and wrote up the initial manuscript with input from all co-authors. Eric Fullerton came up with the explanation that the asymmetry we measured could have arisen because the domains nucleate from a small number of bubbles and expand to large domains.

Determination of Domain Wall Chirality using *in situ* Lorentz Transmission Electron Microscopy

Jordan J. Chess[1], Sergio A. Montoya[2,3], Eric E. Fullerton[2,3] and Benjamin J. McMorran[1]

[1] Department of Physics, University of Oregon, Eugene, OR

[2] Center for Memory and Recording Research, University of California, San Diego, CA

[3] Department of Electrical and Computer Engineering, University of California, San Diego, La Jolla, CA

February, 2017

Determination of Domain Wall Chirality using *in situ* Lorentz Transmission Electron Microscopy

The Dzyaloshinskii-Moriya interaction (DMI) has been at the center of many recent advances in our understanding of magnetic structures, including its ability to stabilize the skyrmion phase in non-centrosymmetric crystals[10, 74, 75], and the stabilization of chiral Néel walls with increased field and current induced mobility[76] by interfacial DMI[77, 78]. Mapping the handedness of these chiral structures requires information of all three vector components of the magnetization and as such has largely relied on imaging techniques capable of directly measuring all three components of the surface magnetization such as spin-polarized scanning tunneling microscopy[79, 80], and spin-polarized low-energy electron microscopy (SPLEEM)[78, 81, 82]. Using SPLEEM, Chen *et al.* demonstrated that this ability to characterize asymmetries in domain wall structures can be a useful tool for determining both the magnitude and sign of the interfacial DMI for multiple magnetic non-magnetic interfaces. Here we show that the x and y components of the magnetic induction determined using LTEM coupled with the additional information gained during an *in situ* magnetic field sweep, can be used to map domain wall chirality.

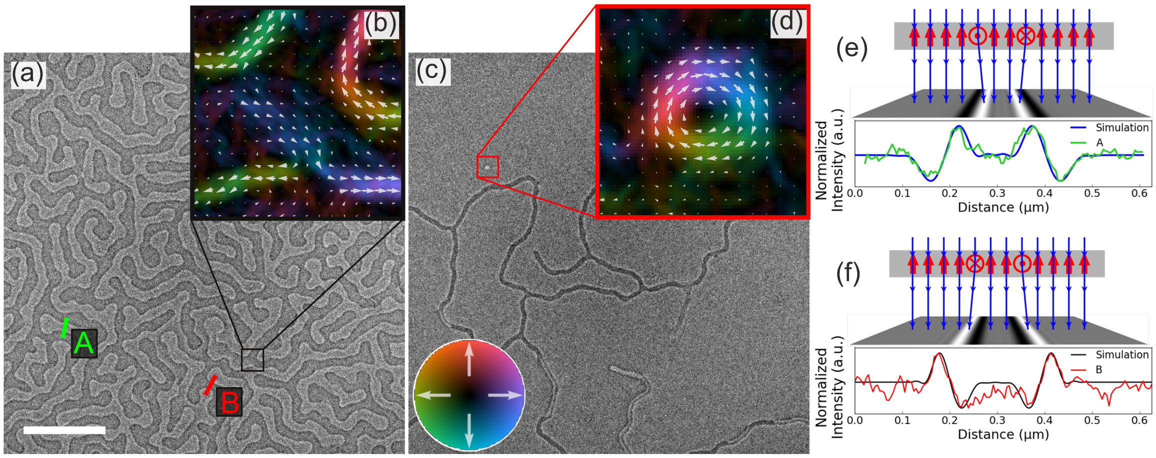

FIGURE 15. LTEM of chiral domain walls
Fresnel-contrast LTEM images of FeGdPtIr at 200 K in an applied field of $H_z = 1$ mT (a) and 20 mT (c), scale bar 2 μm. Insets show the results of single image TIE analysis applied to the indicated sub-regions, color (see color scale wheel) and vector arrows indicate the direction and magnitude of the local in-plane magnetic induction. Inset (b) highlights a region where the Bloch domain wall changes chirality, with a Néel wall bridging the gap between the two regions. Inset (d) gives a detailed look at the magnetic texture of the skyrmion that appears during the field sweep. (e), (f) (top) Schematics showing how deflection of electrons transmitted through the walls can generate LTEM images (simulated) matching the contrast seen in the experimental data. (e), (f) (bottom) Line profiles across domains along the lines (A, B) in experimental image (a) match profiles from the simulated LTEM images in the schematics above.

We apply this approach to field series data taken of an Fe/Gd/Fe/Pt/Ir multilayer film with 80 repeating layers with nominal thicknesses [Fe (3.4) / Gd (4) / Fe (3.4) / Pt (0.25) / Ir (0.75)], produced by d.c. magnetron sputtering onto a 50-nm Si_3N4 membrane. The images were collected using an FEI Titan equipped with a Lorentz lens and integrated CEOS objective lens aberration corrector, using a Gatan cryo-holder for temperature control. The Fresnel-contrast images were recorded at 200 K with a defocus of 300 μm. An out-of-plane magnetic field was applied to the sample by partially exciting the microscope's standard objective lens from -1 to 0.9 % excitation, which results in an applied field varying from roughly $\mathrm{H_z}$ = -28 to 33 mT. This field strength was strong enough to saturate the film in both directions, allowing us to record the progression of the magnetization from the $\mathrm{M_z}$-down saturated state, domain nucleation, expansion of those domains, and finally annihilation of the remaining $\mathrm{M_z}$-down domains leaving the $\mathrm{M_z}$-up saturated state. Figure 15 shows selected images from this field sweep at 1 mT (top) and 20 mT (bottom). These images display labyrinth stripe domains that progress into isolated worm-like domains as the field approaches saturation, similar to previously reported magnetic transmission X-ray microscopy (M-TXM) results on Fe/Gd multilayers[11]. Normally, determining the in-plane local magnetic induction from LTEM data requires multiple images taken at multiple different defoci, but because these films are uniform thickness, a single-image transport of intensity (SITIE) equation can be used to determine the in-plane magnetic induction[83]. The SITIE relates the intensity $I\left(\mathbf{r}_\perp,\ \Delta f\right)$ at a given defocus to the magnetic phase shift (ϕ_m), given a suitable approximation for the intensity of the in-focus image (I_0)

$$\nabla_\perp^2\ \phi_m\left(\mathbf{r}_\perp\right) \approx\ -\frac{2\pi}{\mathrm{f}}\left(1\ -\frac{I\left(\mathbf{r}_\perp,\ \Delta f\right)}{I_0}\right), \tag{4.1}$$

where $\nabla_{\perp}^2$ is the in-plane (x, y) Laplace operator, $\mathbf{r}_{\perp}$ is the in-plane position vector, and $\Delta f$the defocus distance in z from the image plane. In this case, because the film is uniform I_0 is a constant and not dependent on $\mathbf{r}_{\perp}$, we choose to approximate it as the mean of the defocused image. To solve equation (4.1) we employed the Fourier-based method of Paganin and Nugen to determine the magnetic phase shift (ϕ_m)[57]. From the magnetic phase the local magnetic induction averaged through the sample thickness (d) is given by[20],

$$\nabla_{\perp}\phi_m(\mathbf{r}_{\perp}) = -\frac{e}{\hbar}[\mathbf{B}(\mathbf{r}_{\perp}) \times \hat{\mathbf{e}}_{\mathbf{z}}]d \tag{4.2}$$

where e is the electron charge, $\hbar$ is the reduced Planks constant and $\hat{e}_z$ is a unit vector parallel to the electron propagation direction.

Using this analysis, we determined the in-plane component of the magnetic induction from each of the individual LTEM images taken during the field sweep. Examples of this analysis are shown in the insets of Figure 15. The left inset (FIG 15.b) shows a region of Figure 15.a where the domain wall chirality reverses (a Bloch-point). The domain walls in this film are predominantly Bloch. Figure 15.d shows this analysis applied to the region containing a skyrmion that appears in the image during the field sweep.

We observe that many of the domain walls have no chirality reversals, i.e. Bloch-points, suggesting that the domain walls in this sample are mostly of one chirality. This cannot be known for certain without knowing which domains are up and which are down. This single chirality for a given domain wall, can also be determined by observing the intensity patterns in the Fresnel-contrast images. The domains in these images appear to have light and dark contrast which gives the false impression that the contrast is related the magnetization in the domain. In reality this contrast is only dependent on the in-plane domain wall spins. In fact, close examination of the images reveals that this light-dark gray shading is a result of the Bloch-type domain walls which act to push the impinging electrons into or out of the domain depending on the direction of the in-plane domain wall spin. Figure 15.(e and f) schematically show the origin of this contrast, in both the particle (rays) and wave picture (simulated image[23]). Additionally, shown in (e) and (f) are line profile data taken from the regions indicated in image (a) together with the profile from the simulated image. These profiles show the agreement between the experimental data and simulated images, indicating that indeed the apparent lightness or darkness of labyrinth domains in raw Lorentz images are due to the chirality of the domain walls surrounding them, and not the perpendicular orientation of the magnetization within the domains.

The Lorentz force only acts on electrons traveling perpendicular to a magnetic field, so LTEM is only sensitive to in-plane components of the magnetization. This poses a problem when attempting to assign a handedness to the domain walls rotation because one must know the perpendicular component of the magnetization M_z. Fortunately, this information is easily obtained from the history-dependent information in the field sweep. This information is clearly discernable in Figure 15.c, in which the applied external field is 20 mT, where we can see narrow worm-like domains surrounded by larger domains. As the applied field increases these domains continue to shrink and eventually annihilate, leaving the whole film in the saturated M_z-up configuration. This indicates that the domains that are shrinking in size are pointed in the direction anti-parallel to the applied magnetic field.

To determine the sign of the perpendicular component of the magnetization in each magnetic domain, we start at the image where domains first nucleate, assign each large domain to be pointing in the direction of the applied field, and each narrow domain in the direction opposite of the applied field, then ensuring that the up domains expand and the down domains contract as the applied field is swept from positive to negative. Computationally this required segmenting each image in the sequence which was accomplished using 4 steps: (1) automated edge detection, then (2) manual correction to the detected edges, followed by (3) automated sorting of domain walls based on domain width, and then finally (4) corrections to sorted domains, enforcing the rule that a domain shrinking in area is pointed in the direction anti-parallel to the increasing applied field.

After determining the sign of each perpendicular magnetic domain, the chirality of the spins in each domain wall were characterized following the approach of Chen *et al.* defining the local domain wall chirality angle α. Here $\mathbf{n}$ is defined to be in the plane of the film perpendicular to the domain wall and pointing from M_z-down to M_z-up. The angle α is then defined to be the angle between the domain wall normal ($\mathbf{n}$) and the domain wall magnetic moment measured in the counter clockwise direction[78]. At the top of Figure 16, a schematic visualization of α is shown for the region included in Figure 15.b.

Figure 16 has a spatial visualization of the distribution of domain wall chirality angles (α) for three of the images taken during the field sweep with the applied field indicated on the LTEM data in the left column. In each image in the right column the M_z-down domains are shown in black, M_z -up in white, and alpha is show in color corresponding the to the color scale wheel. The frames are dominated by the blue color corresponding to $\alpha \approx \pi/2$, which we are referring to as a right-rotating Bloch wall where right denotes the direction the magnetization rotates (clockwise)

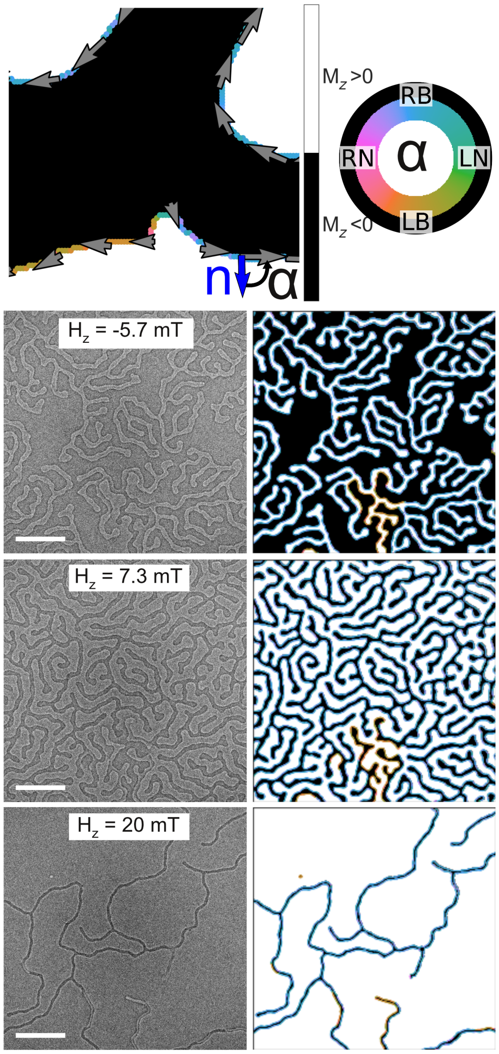

FIGURE 16. Chirality map

Top The same region as Figure 15.b. with the sign of $\mathrm{M_z}$ labeled with black (negative) and white (positive), along with the domain wall chirality angle (α) visualized in color (see color wheel indicating (RB right-rotating Bloch, LB left-rotating Bloch, RN right Néel, LN left Néel)). **Left** Fresnel-contrast LTEM image of FeGdPtIr at 200 K with applied filed indicated on each image, scale bar 2 μm. **Right** Maps of domain walls chirality, white indicates $\mathrm{M_z}$-up domains, $\mathrm{M_z}$-spin down, color the angle α. α is defined to be the angle between the in-plane domain wall spin and the vector normal (**n**) to the domain wall pointing from $\mathrm{M_z}$-down to $\mathrm{M_z}$ -up, measured from **n** to the in-plane spin (see schematic in top image with **n** shown in blue).

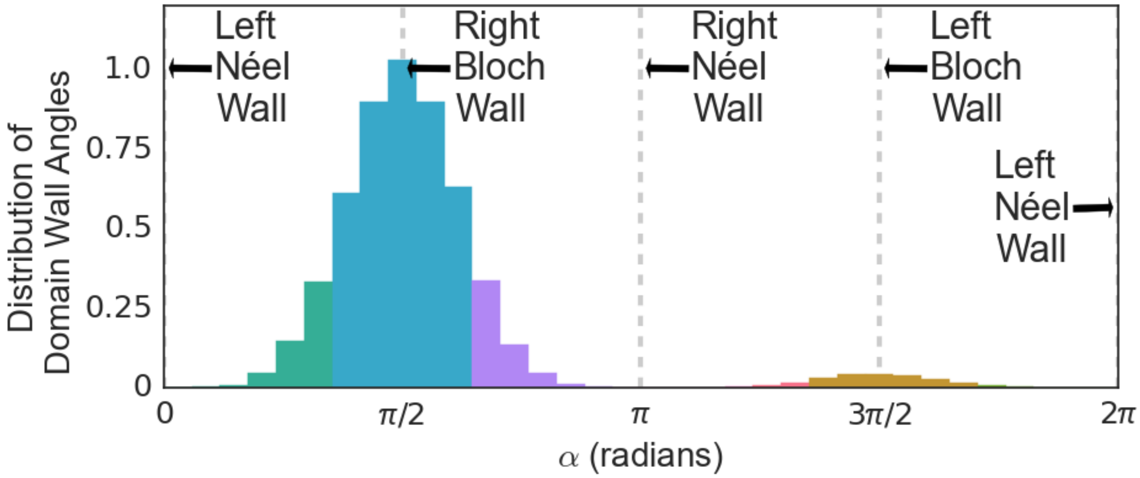

FIGURE 17. Chirality distribution
Probability distribution of domain wall chirality angle (α) in the field of view, for all field values in the series that have domains present. There is a high asymmetry that favors right-rotating Bloch walls in this field of view, making up 95% of the domain wall pixels, which remains constant thought the field sweep.

as the domain wall is traversed from $\mathrm{M_z}$-down to $\mathrm{M_z}$-up, and counter clockwise for a left-rotating Bloch wall ($\alpha = (3\ \pi)/2$).

The statistical distribution in α is shown in Figure 17 for all images in the series for which domains are present. The overwhelming majority of the domain walls are right-rotating Bloch walls comprising 95% of the domain walls imaged. We note that this number remains roughly constant as a function of applied field. To remain consistent with the literature[78, 81, 82] in Figure 17 we have labeled $\alpha = 0$ and $\alpha = \pi$ as right-rotating and left-rotating Néel walls respectively.

It is somewhat surprising that there is a preferred helicity of the domain walls. As noted by multiple authors, interfacial DMI that may be expected from the Ir/Pt layers is not expected to split the energy degeneracy between right and left Bloch walls.[76, 82] There could be multiple explanations for the preferred helicity. It has been shown previously that stripe domains in similar high-anisotropy films emerge out of widely distributed nucleation sites[84]. Each nucleation site would be expected have one of two helicities. As the field magnitude increases the nucleation site become unstable and the stripe domains grow and fill the volume, forming large regions with interconnected stripe domains arising from the same nucleation site[85]. As the stripe domains grow and split it would not be surprising that they maintain a common helicity determined during nucleation. Thus a finite image area may have a common or preferred helicity even in the absence of symmetry breaking. Micromagnetic simulations of Fe/Gd indicate that Néel caps are present near the surfaces of the film at the top and bottom of each domain wall[51]. In the simulations, the caps at the top surface have exactly opposite in-plane components as their counter-part on the bottom surface, making their effects cancel in transmission-based imaging such as LTEM images taken at normal incidence. Such Néel caps are expected to be less prevalent in the current films but they could provide a mechanism through which interfacial DMI affects the helicity of the Bloch part of the wall imaged by LTEM. Further investigations will be dedicated to determining the existence of Néel caps in this system, and their possible role in controlling the chirality of the Bloch walls.

We have shown that by coupling a single-image TIE analysis with the history-dependent information gained from an *in situ* applied field sweep, the chirality of a given domain wall can be unambiguously determined as well as the evolution with applied field. This technique has the advantage of avoiding the need to tilt the sample to gain information about the third component of the magnetic induction, and it can be applied to rapidly measure domain wall chirality distribution over a large area. This allows its use to be extended to magnetic structures that must be stabilized by a perpendicular field such as a skyrmion phase.

Chapter Conclusion

In this chapter, we developed a measurement technique that allows us to measure the chirality of Bloch-type domain walls. The initial results on one small region of the sample were promising in that they indicated that asymmetric layer stacking could be used to control the chirality of Bloch domain walls. This is interesting because theory predicts that iDMI does not break the degeneracy of Bloch walls. The next chapter includes results of applying this method to a larger dataset.

CHAPTER V

IMPROVED DOMAIN WALL DETECTION

Notes on Manuscript

This chapter ‘Python Tools for Domain Wall Detection and Domain Classification’ is the skeleton of a manuscript detailing a refined algorithm that can be used to detect domain walls for segmentation of LTEM images. This worked benefitted from fruitful conversations and pointers from Professor Greg Bothun. Harjasleen Gulati added in the manual labeling of images. The work started as a project for the graduate student-organized seminar, Data Science and Machine Learning at the University of Oregon.

Python Tools for Domain Wall Detection and Domain Classification

Recently we demonstrated a method for measuring the chirality of domain walls using *in situ* Lorentz transmission electron microscopy[86]. This approach requires a significant amount of edge detection (domain walls) and image segmentation (domain classification). The second step, segmenting and classifying the domains after the edges are detected is quite easy using publically available python packages[87, 88]. The hard part is detecting all the domain walls properly. Our approach was to try using existing packages such as scikit-image's Canny edge detector[88]. Prior to using the Canny detector, an anisotropic diffusion filter was applied to the images to reduce noise but preserve edge features[89]. Additionally, Mahotas[90] hit-and-miss functions were used to detect and remove locations where a labeled edge forked into two lines, since physically a domain wall does not fork into two domain walls. Finally, custom python functions were developed to remove short superfluous lines and connect nearly connected lines. In all, this resulted in the correct labeling of roughly 80% of the domain walls. The results of this processing were then overlaid in color on top of the original grayscale data and exported to a paint program to be corrected by hand. Figure 18, depicts the various stages of this process.

Unfortunately, the process outlined above-even with the aid of the automated edge detection algorithm-required roughly four hours of manual correction per image. As noted in the previous chapter, before any quantitative statement about the domain wall chirality of a given material can be made, a statistically significant sample area must be imaged. This suggests a need for improved domain wall detection tools. It is worth noting that edge detection is in no way a solved problem in the computer vision community; it remains on of the most studied problems in the field[91]. Taking a cue from recent developments in the field, we take a supervised learning based

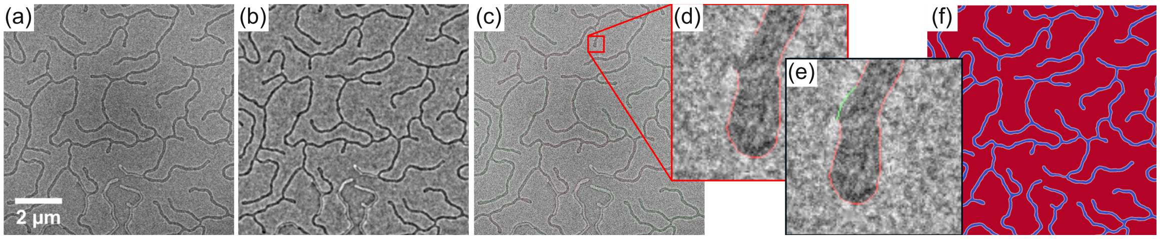

FIGURE 18. Initial Edge Detection Process
(a) Representative raw LTEM data. (b) The same data after smoothing process. (c) Detected edges overlaid on top of the original data, green indicates an edge with no endpoints other than those that terminate at the boundary of the image, red indicates edges with dangling endpoints that need connected to other detected edge segments. (d) A close up of a region where manual correction was required, and (e) the correction to the problem. (f) The final segmented image with up domains labeled in red, down domains in blue, and domain walls white.

approach[91], using the previously labeled data to train a new edge detection model. Many supervised learning edge detection algorithms in the literature require many human-labeled training examples, in this case there were only nine available. On the other hand, each image in our data is a 2048 × 2048 array, meaning 4,194,304 pixels. Due to the large number of pixels needing to be processed and the risk of overfitting associated with more complex models, logistic regression is used for our new edge classifier.

Basics of Logistic Regression

The goal of a classification algorithm is to find a decision boundary between two populations. In the edge detection context an edge is considered a success and everything else a failure. To better understand the logistic regression model consider a specific example using only one variable, also known as a “feature”: the gradient magnitude of the image. This example is chosen because the gradient magnitude is the basic quantity used in the canny algorithm, and a natural way to define an edge is a region in which the gradient is large. Additionally, in this case the gradient of the

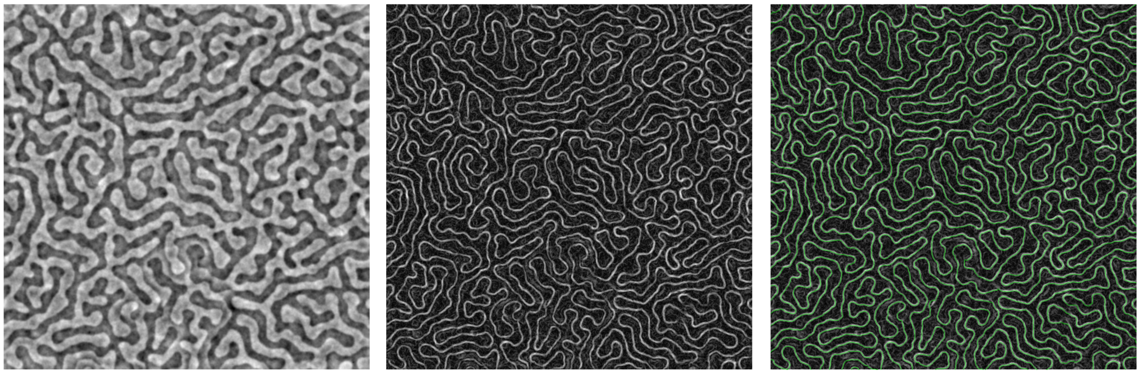

FIGURE 19. Gradient Edge Detection
(Left) Example phase image of a FeGdPtIr multilayer film (field of view $\approx 9\mu$m).
(Center) Gradient magnitude of the phase image on left. (Right) Gradient magnitude with edges overlaid on top.

phase image is directly related to the magnitude of the magnetic induction. Figure 19 shows an example phase image determined using SITIE, the gradient magnitude of the same image, and the gradient magnitude with the labeled edges overlaid. The eye can easily pick out where the edges are in Figure 19.b, but keep in mind that the eye is using much more information that just the value of the gradient. Nevertheless from the Figure it is clear that the gradient is a reasonable feature to use for edge detection.

For logistic regression we seek to fit the model,

$$F(x) = \frac{1}{1 + \exp\left(-(\beta_0 + \beta_1 x)\right)}, \tag{5.1}$$

to our labeled data. Above β_0 and β_1 are fitting parameters and x is the value of the gradient magnetude at a given pixel. Figure 20 visually shows this fit on a subsample of the pixels in the image above. One advantage of using logistic regression is the simplicity of interpreting the results, the value of $F(x = x_0)$ is the probability of a pixel with gradient magnitude x_0. The decision boundary for a 50% probability is

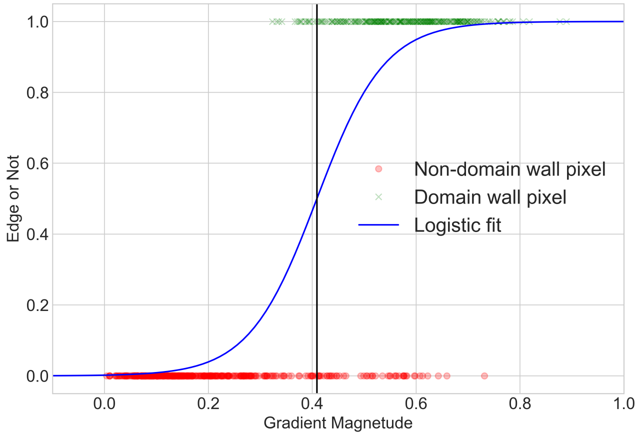

FIGURE 20. Logistic regression classifier
Visualization of the logistic regression classifier. Domain wall pixels were subsampled at 1:1,000th the original number and domain pixels at 1:10,000th, to allow for a meaningful visual representation with discernible individual points.

then given, simply by the value x where $F(x) = 0.5$. In this case $F(0.41) \approx 0.5$, so any pixel with gradient value above 0.41 could be classified as a domain wall because the model is predicting a greater than 50% probability.

Full logistic regression model

The logistic regression model can easily be extended to multiple dimensions, in which case the new equation is,

$$F(\mathbf{x}) = \frac{1}{1 + \exp\left(-\beta \cdot \mathbf{x}\right)}. \tag{5.2}$$

Now $\mathbf{x}$ and β are both vectors with dimensionality equal to the number of features plus one, for the x_0 component which is set to 1. In this case the decision boundary is not a single value on the 1D number line, instead it is a hyperplane that divides the multidimensional feature space. The new model is composed of fourteen different features (shown in Figure 21). These features include the Gaussian

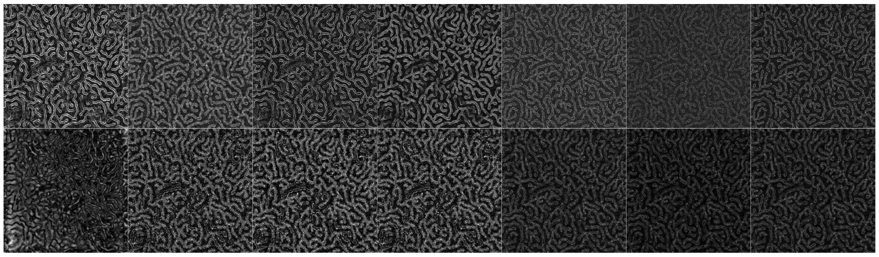

FIGURE 21. Logistic regression features
The fourteen different transformations to the original image that are used as features in the logistic regression model.

gradient magnitude of the image taken with different kernel sizes, rolling standard deviation filters, higher-order derivatives, gradient magnitudes of images smoothed with various edge preserving filters, and the results of convolving a wavelet with the initial image. This initial logistic regression classifier interprets low-level local pixel information into a number between 0 and 1 that is the model's prediction for the probability that a given pixel is part of a domain wall. A threshold of 45% was then used to separate the two classes, and the resulting binary image was then skeletonized to a single pixel line. 45% results in more false positives but these turn out to be easy to remove. This value was picked using the guess-and-check method and could be refined further. Finally, all endpoint pairs that were each other's only nearest neighbor, less then 15 pixels apart, and well aligned, were connected with a straight line.

Incorporating Mid-level Information

The logistic regression classifier detailed in the section above performs better than the Canny detector, but not sufficiently well to have it be the final step in the

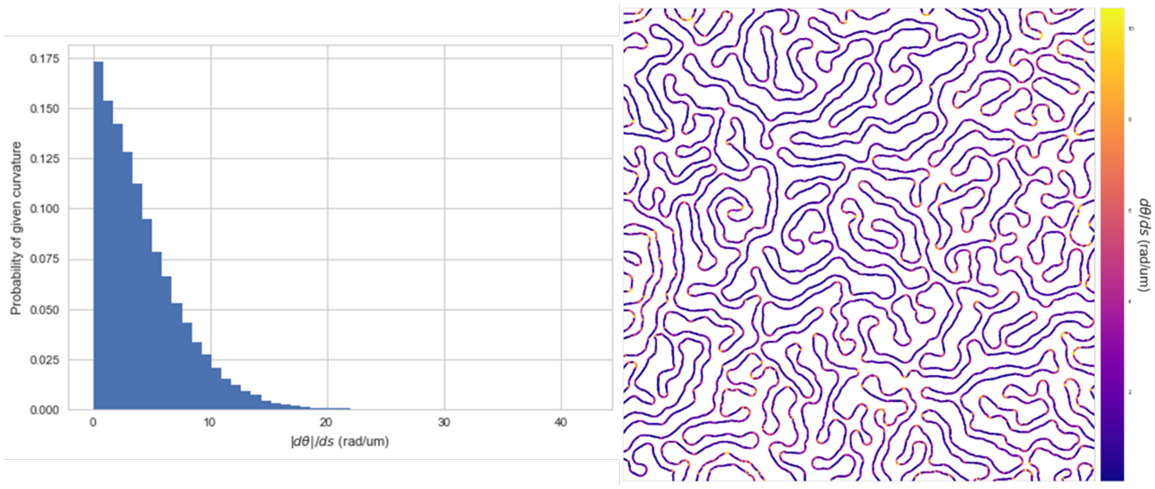

FIGURE 22. Domain wall curvature
Probability density function for the domain wall curvature in the image to the right.

process. Three additional classifiers were built to incorporate the mid-, and high-level information in the images.

First, from the previous section one could guess that due to the threshold being set below 50% the results are biased toward including false positives. The majority of the false positive pixels add to the thickness of the edge and are removed during the thinning process, but there are also some systematic problems caused by this threshold. Almost always these problems are near the end of a detected domain wall segment, in which case the false positives cause the end of the line segment to curve sharply, when in reality the line should continue roughly straight. To solve this problem, the curvature of the path at each pixel was calculated. This information was then used to construct a probability density function (PDF) for the domain wall curvature for each image, Figure 22 shows an example PDF. The PDF was then used to identify the top 99th percentile of curvature pixels, which were then removed from the detected paths.

Second, after removing the high curvature pixels, more mid-high-level information was used to determine both how parallel edge segments were to their nearest neighbor segment. This was done by calculating for each pixel the distance to the nearest pixel that is not part of the edge segment in question. Then for each segment the mean and standard deviation of these values were calculated. All the values were then normalized to have standard deviation of one. Clusters in the data were then detected using the spectral clustering algorithm available from scikit-learn[92]. Further, to prevent removal of false negatives, the length, distance of endpoint to nearest endpoint, and angular change needed to attach to that endpoint were calculated. If the length was above a threshold value, or if the distance to a nearest endpoint and angular change were both small, negatives were moved into the positive group. Finally, these results are used to train a support vector machine classifier so that they can continue to be used on the data when additional lines are added during future steps. Figure 23.a show an example of this clustering process, accompanied by the spatial version of the data.

Third, the final classifier categorizes endpoints based on two features: ratio of nearest neighbor to next-nearest neighbor distance, and angular change needed to connect the two lines. The three categories are: connectable by straight line, obvious nearest neighbor, cluster needing more information. Figure 24 show an example of this network like analysis. Like the category name suggests, neighbors that can be connected with a straight line are, the code then attempts to find a high probability path to connect the obvious nearest neighbors. Finally, a structured element that we will refer to as a flashlight (see FIG 25), and describe below, is used to try to connect lines in the clustered regions or at least move these points into one of the other categories for further processing.

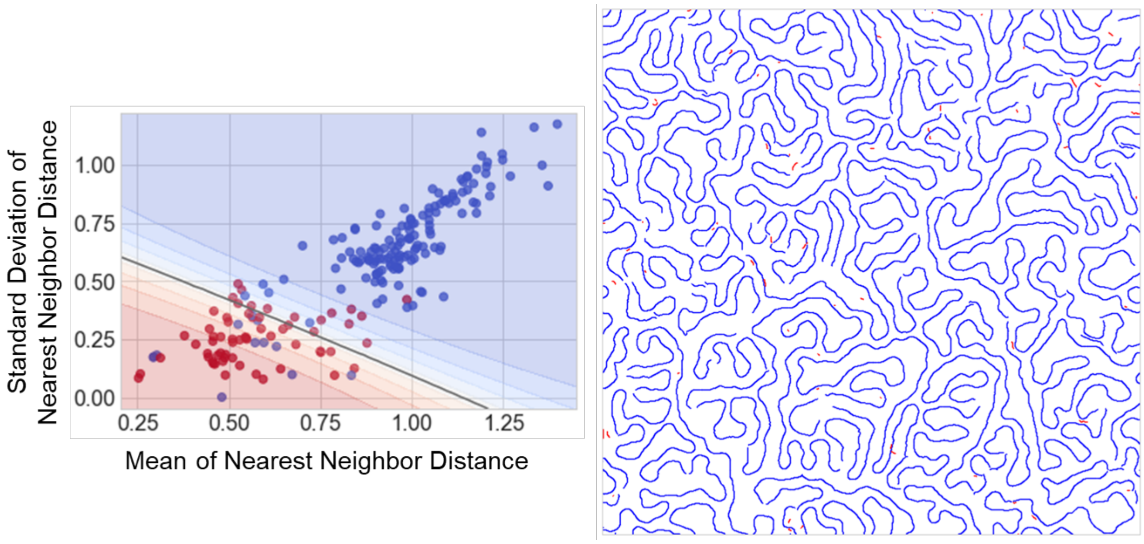

FIGURE 23. Removal of Non-parallel Edges
Left Results of cluster analysis, red points labeled to be removed from the image.
Right Results of cluster analysis visualized in real space.

The flashlight was calculated using the previously labeled data; it is related to the radial plus angular conditional probability. Given an endpoint and velocity vector at the end of a line, it represents the probability that the line will propagate to a given r and θ value. The flashlight is used by placing it in at the location of the endpoint of a line pointing in the direction of the end of the line, weighted by the probability predicted by the initial logistic regression step, shown in Figure25.b. This process is repeated for each of the next 15–30 pixels at the end of the line, and then for each line of interest. Following this, a threshold is again applied and the resulting regions are thinned to a single pixel line. This generally acts to either connect two edge segments or to extend them allowing them to be placed in a different category.

The full process is then iterated, generally for a set number of times due to the difficulty of determining a proper stopping condition. During each consecutive iteration the initial logistic regression threshold is lowered to incorporate more pixels that were missed in the previous pass, and the higher level classifiers are relied on to

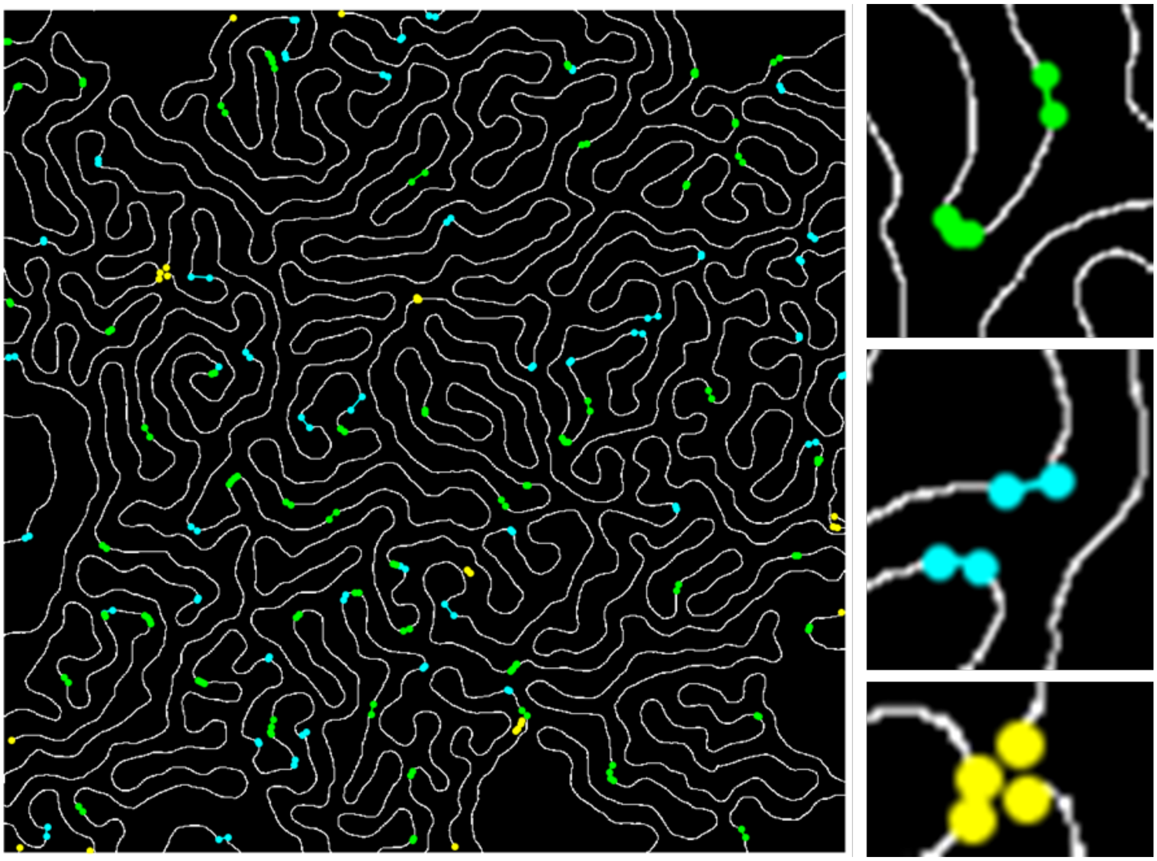

FIGURE 24. Network analysis
Labeled endpoints after categorization, green-straight connect, cyan-obvious nearest neighbors, yellow-needs more information.

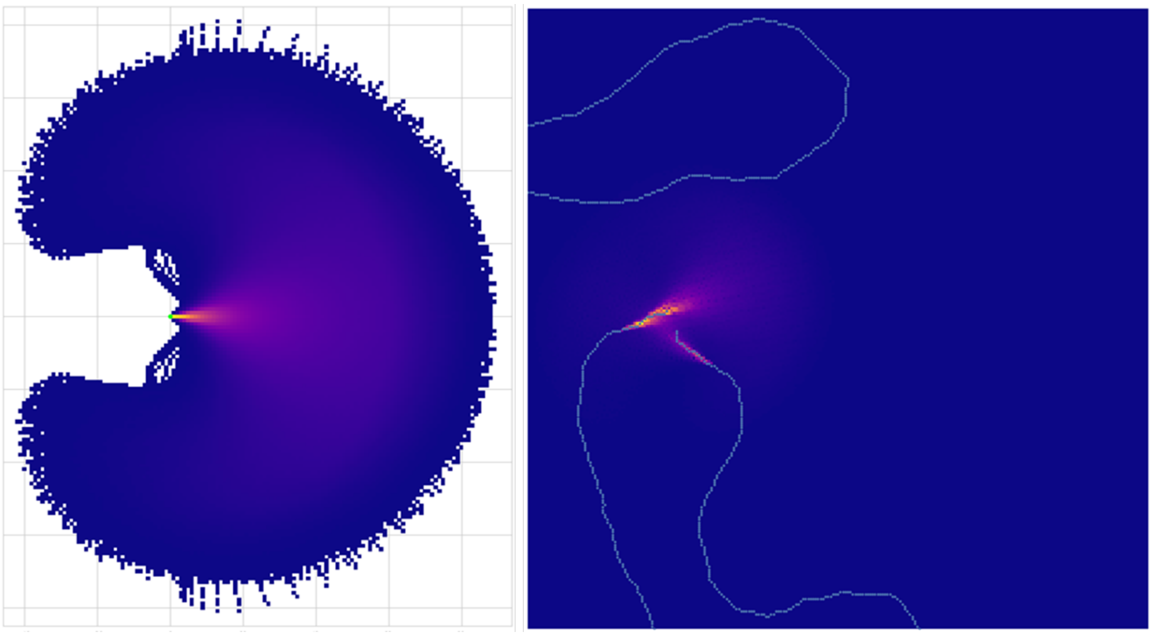

FIGURE 25. Flashlight Structure Element
Left Flashlight structure element used to weight possible paths.**Right** Application of the flashlight element used to connect two endpoints in a broken path.

reject false positives. This process at best detects all the domain walls present in the image, and at worst greatly reduces the amount of human time needed to correct the labeling. Figure 26 shows the lines detected using the original process and those using the new process with zero human corrections. Notice that the new process detected domain walls that were missed during the original process, and didn't detect a false positive that was present in the initial data.

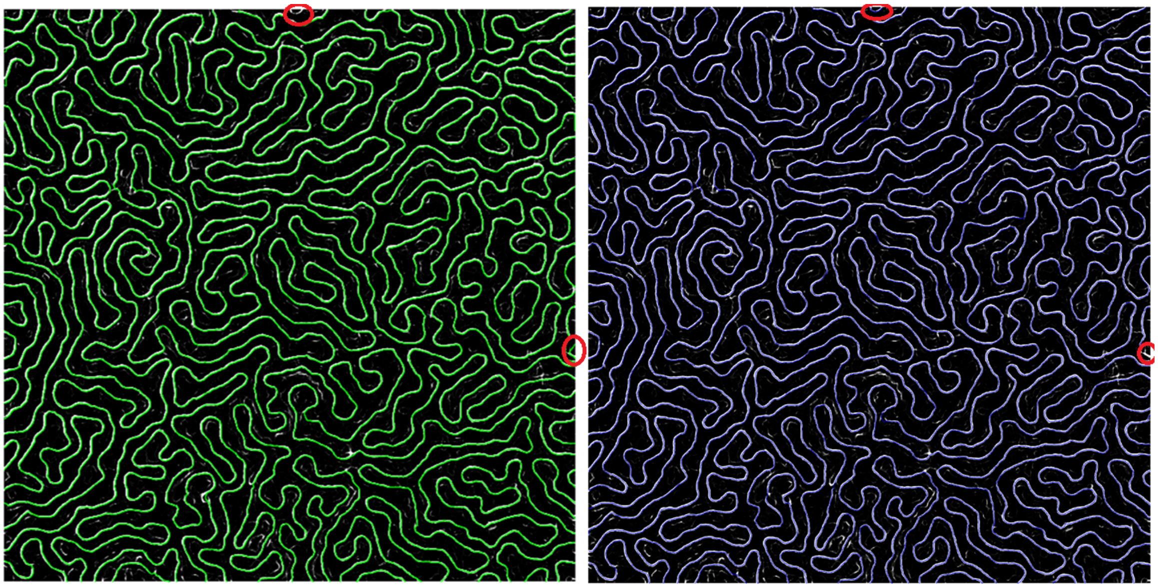

FIGURE 26. Old vs New Edge Detection
Left Domain walls detected using the original algorithm.**Right** Domain walls detected using the new algorithm. Circled are two points where the new algorithm outperformed the origianl one.

Chapter Conclusion

In this chapter an algorithm for detection of domain walls was described. The algorithm utilizes previously labeled data, and could easily be modified for use on other image segmentation tasks. The following chapter discusses the results of applying this algorithm to a larger dataset.

CHAPTER VI

QUANTITATIVE ANALYSIS OF CHIRALITY MEASUREMENTS

Notes on Manuscript

‘Controlling the Chirality of Bloch Domain Walls’ is my contribution to a manuscript being co-written with Sergio Montoya, Eric Fullerton and Ben McMorran. Harjasleen Gulati assisted in the manual segmentation of part of the LTEM images. Sergio conceived of the idea, made the samples, and did the topological hall effect measurements. I recorded and analyzed all the LTEM data presented below, and wrote up this portion of the manuscript.

Controlling the Chirality of Bloch Domain Walls

Recently, the massive search for materials supporting skyrmions above room temperature in the absence of large magnetic fields has identified a number of promising thin-film and multilayer systems[24, 30, 93, 94]. The existence of skyrmions in these systems is attributed to the interfacial Dzyaloshinskii-Moriya interaction (iDMI). This effect arises from the breaking of inversion symmetry at the interface and spin-orbit coupling between the layers[95]. In the micromagnetic framework this energy can be expressed as,

$$E = D\left(m_z\partial_x m_x - m_x\partial_x m_z + m_z\partial_y m_y - m_y\partial_y m_z\right). \tag{6.1}$$

This term lowers the energy for Néel walls with a specific chirality, thus the sign of D determines the chirality of the sample. Here we present the observation of a topological Hall resistance and an extensive Lorentz microscopy study that both reveal that the chirality of Bloch walls can be controlled by stacking of layers in a way that breaks inversion symmetry.

Fe/Gd/Fe/Pt/Ir multilayer film with 160 repeating layers with nominal thicknesses [Fe (3.4Å)/Gd (4Å)/Fe (3.4Å)/Pt (0.25Å)/Ir (0.75Å)] were produced by sputter deposition onto a 50 nm Si_3N_4 membrane. Simultaneous anisotropic magneto resistance (AMR) and Hall resistivity field dependent measurements were performed using Quantum Design Physical Property Measurement System. The AMR is measured in three different magnetic field configurations: (i) longitudinal, $\rho_{||}$, (ii) transverse, $\rho_{\perp}$, and (iii) perpendicular to the film $\rho_{\otimes}$ (see Figure 27). Our measurements suggest that the samples possess a preferred chirality due to the presence of a topological Hall response.

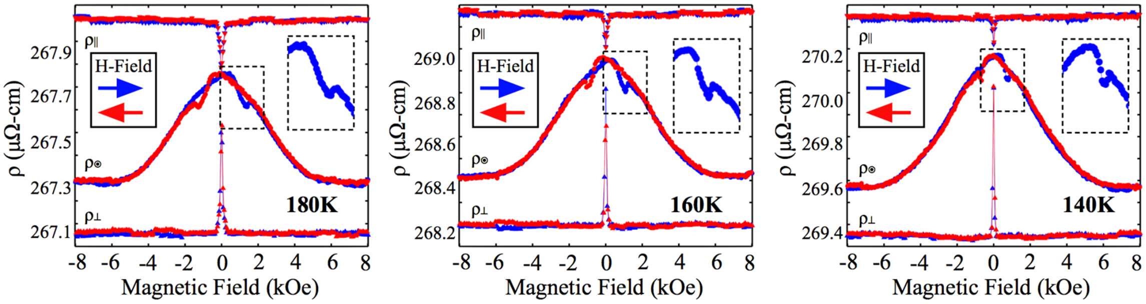

FIGURE 27. Anisotropic Magneto Resistance (AMR)
AMR loops from three different magnetic field configurations: (i) longitudinal, $\rho_{||}$, (ii) transverse, $\rho_{\perp}$, and (iii) perpendicular to the film $\rho_{\otimes}$.

To confirm this result we apply the approach described by Chess *et al.*, with an improved image segmentation algorithm, to numerous images taken of Fe/Gd/Fe/Pt/Ir multilayer films. The images were collected using an FEI Titan equipped with a Lorentz lens and integrated CEOS objective lens aberration corrector. Cooling was achieved using a Gatan cryo-holder. Fresnel-contrast images were recorded at 140, 160, and 180 K with a defocus of 1.5 mm. Unless indicated otherwise all data was recorded after a field cycle from positive saturation to negative saturation and then up to a slightly positive field. The slightly positive field was chosen to allow for differentiation between positive and negative domains, based on domain width. This field cycle was done both to remove any effects of exposure to magnetic field while inserting the sample into the microscope, and it allows for direct comparison with previously recorded topological hall measurements.

The films have out-of-plane magnetization with labyrinth like domains. Figure 28 shows a typical LTEM image accompanied with an image of the in-plane magnetic induction calculated using SITIE[96] for the same field of view. Figure 29 shows the chirality map for the same region shown in Figure 28.

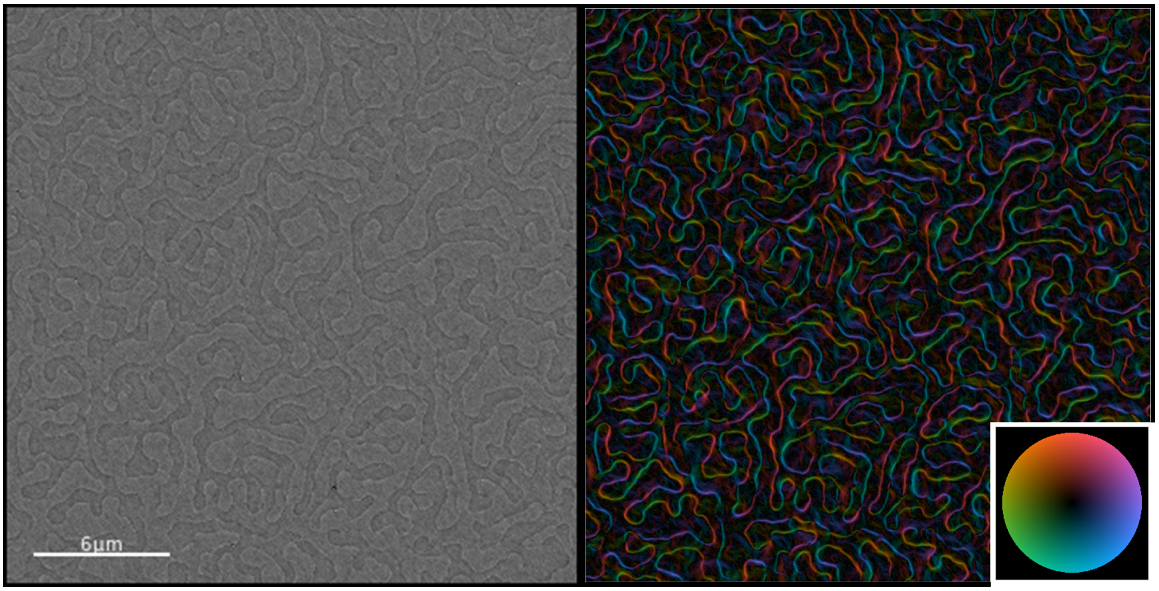

FIGURE 28. LTEM and SITIE of FeGdPtIr
Representative Lorentz TEM image, together with the corresponding in-plane magnetic induction map.

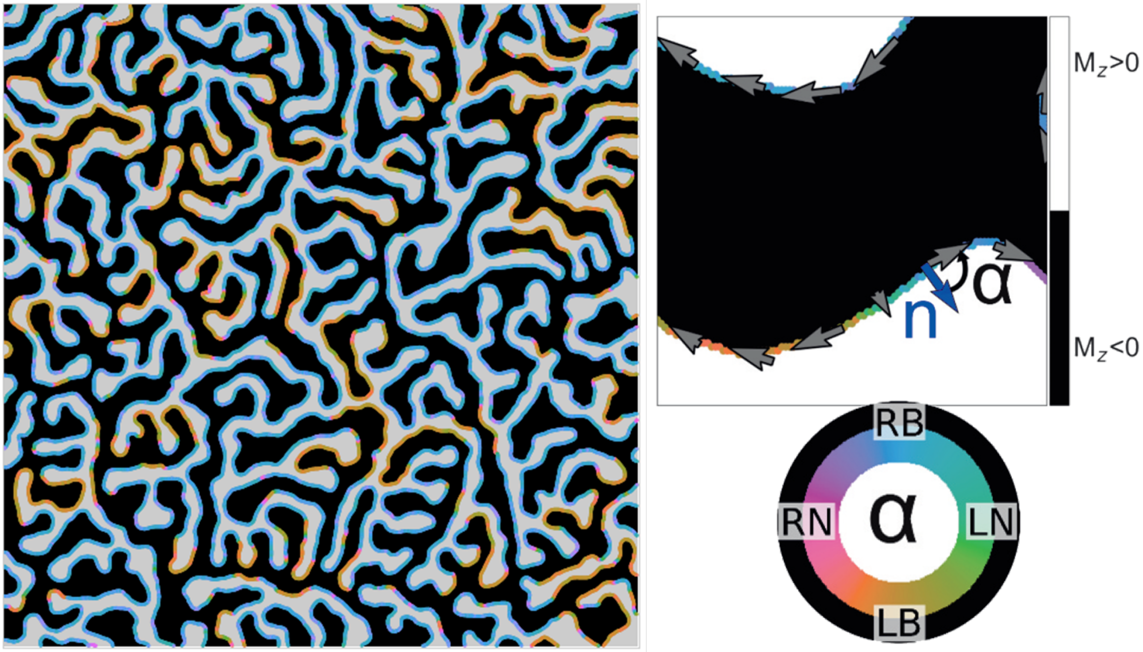

FIGURE 29. Chirality Map
Chirality map indicating the spatial distribution of domain wall chirality. Also included, the scale and schematic illustrating how alpha is defined.

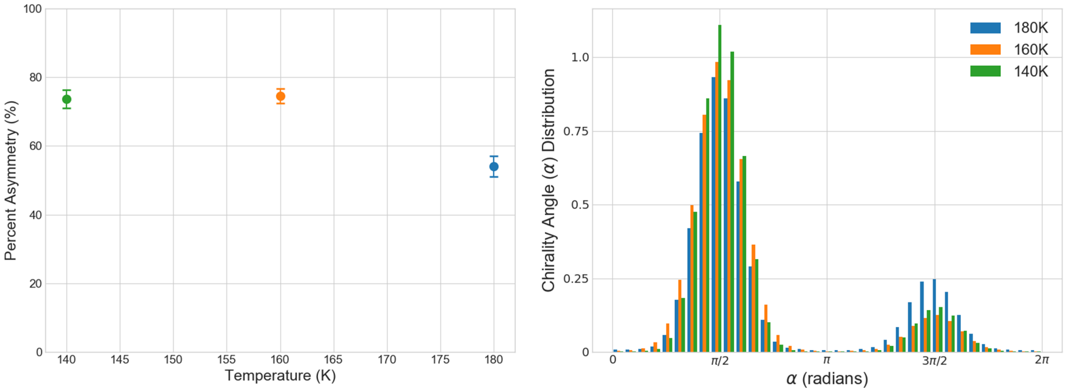

FIGURE 30. Chirality as a Function of Temperature
Left Plot showing the change in chirality as a function of temperature. The error bars in the plot indicate the standard error, treating each image as an individual sample.**Right** Histogram showing the chirality distribution for the three measured temperatures.

The total number of images included in this study is 31, taken at a magnification of 810 X, converted to an area that is ~20,956 μm^2, or ~46 mm in domain wall length. Figure 30 is a plot of the percent asymmetry (γ),

$$\gamma = \frac{(\text{number of R Bloch wall pixels}) - (\text{number of L Bloch wall pixels})}{(\text{number of R Bloch wall pixels}) + (\text{number of L Bloch wall pixels})} \times 100\%, \tag{6.2}$$

for each temperature, as well a histogram showing the chirality distribution for each temperature individually.

Additionally, we had two auxiliary questions: “Is the chirality dependent on the directionality of previous field cycles applied to the sample?” and “Is the chirality determined at one location during multiple field cycles statistically different than the chirality determined from randomly sampling multiple locations on the sample?” To answer these questions, images at 160 K were recorded in three different ways: first cycle the field and record images of random locations, second record 5 images at one

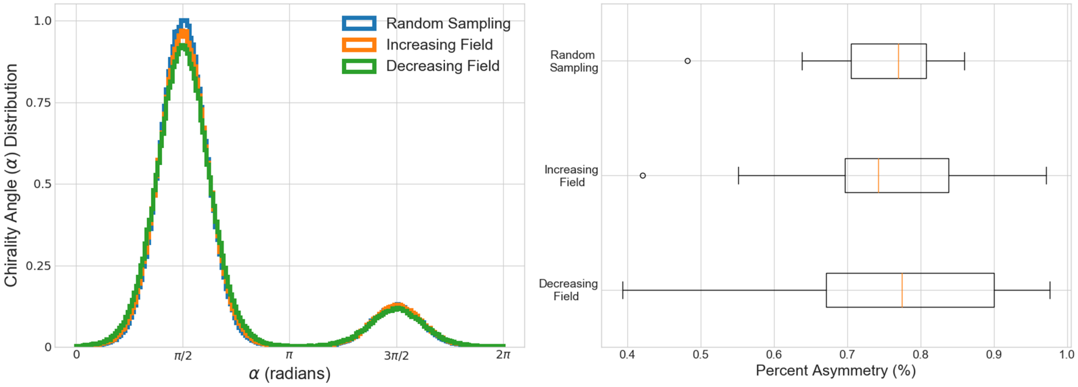

FIGURE 31. Independence of Chirality on Direction of Applied Field **Left** Histogram showing the chirality distribution for the three measurement methods. **Right** Box and whisker plot showing the three measurement methods.

location but cycle the field between each image, third in the same location as before cycle the field from negative to positive and then to a slightly negative field between each image, again recording 5 images.

Figure 31 shows the chirality distribution for the negative, positive, randomly sampled locations. Also shown in 31 is a box and whisker plot showing that there are no significant differences between the three measurements. Further, binomial statistics were used to quantify the error which indicates that each of the three sample means are within counting error of each other.

Evaluating equation (6.1) for a Bloch wall gives zero, so iDMI cannot explain the degree of chirality for this sample. The existence of this high degree of chirality indicates the presence of a bulk-like DMI term in the energy. Our results reveal that the chirality of Bloch walls can be controlled by breaking inversion symmetry through asymmetric layer stacking. These results necessitate a further theoretical study on the origin of this induced bulk-like DMI.

Chapter Conclusion

This chapter presented the results of combining the algorithm and analysis technique described in the previous two chapters applied to a large dataset. The results of this analysis showed that the chirality of Bloch domain walls can be controlled by asymmetric layer stacking. This asymmetry is not predicted by theory and necessitates further theoretical developments.

CHAPTER VII

3D STRUCTURE OF DIPOLE SKYRMIONS

Notes on Manuscript

This chapter 'Determination of the 3D Structure of Dipole-Skyrmions' is the start of a manuscript detailing a correlative microscopy approach utilizing transmission and surface based magnetic imaging and micromagnetic simulation to determine the full 3D magnetization of dipole-skyrmions in Fe/Gd films.

Ben and I conceived of the idea. Sergio Montoya deposited all specimens and measured the bulk magnetic. Simon Couture ran the micromagnetic simulations. John Unguris and Ian Gilbert collected and helped analyze the SEMPA data. Saul Propp helped identify the Hopf character of the magnetic structure. Josh Rasink assisted in collecting LTEM data. I collected part of and analyzed all the LTEM data assisted in analyzing the SEMPA data produced all figures and wrote up the initial manuscript.

CHAPTER VIII

DETERMINATION OF THE 3D STRUCTURE OF DIPOLE-SKYRMIONS

As discussed in Chapter III, both the micromagnetic simulations and the resonance spectra suggest a more intricate three dimensional magnetization for dipole-stabilized skyrmions in the Fe/Gd system. A full understanding of the 3D magnetic skyrmion texture can help build better models for skyrmion dynamics. As referenced earlier, due to presence of magnetization with opposite directions at the top and bottom of the sample (asymmetric Néel caps), the transmission geometry of LTEM and RSXS do not produce any contrast indicating this magnetization. This effect is further exacerbated in LTEM due to the fact that Néel walls and Néel-type skyrmions do not produce LTEM contrast. This phenomenon can be understood by writing out to first order the image intensity in terms of the sample magnetization. For an electron traveling in the $\hat{z}$ direction[97],

$$I(\mathbf{r}_\perp, \Delta f) = 1 - \Delta f \frac{e\mu_0\lambda t}{h} \left(\nabla \times M(\mathbf{r})\right) \cdot \hat{z}, \tag{8.1}$$

where e, μ_0, λ, t, h are the electron charge, permeability of free space, electron wavelength, sample thickness, and Planck's constant, respectively. For a Néel wall $(\nabla \times M(\mathbf{r})) \cdot \hat{z}$ evaluates to zero. This problem can be overcome by tilting the sample. This strategy has been used to image Néel walls as well as skyrmions by several authors[98, 99]. The image contrast is then largely caused by the core of a skyrmion, meaning the polarity of a skyrmion can be determined but not the topology, making it difficult to distinguish between a skyrmion and a topologically trivial bubble with this approach. To date there has been no direct real-space observations of the 3D magnetic texture of a dipole-skyrmions.

Park *et al.* claimed to determine the skyrmion texture for a DMI skyrmion[100] by using off-axis electron holography to measure a $\mathrm{Fe_{0.5}Co_{0.5}Si}$ sample with a stepped thickness. Off-axis electron holography is a interferometric technique that can be used to measure the phase shift experienced by a electron passing through sample. Off-axis electron holography is a more demanding experimental technique than in-line holography (TIE), but it has the advantage of being sensitive to the D.C. component of the electron phase and is generally thought to be more accurate. Park *et al.* used this added sensitivity to determine the magnetic phase shift caused by a skyrmion as a function of thickness, which is the reason for the step-shaped sample. They determined that the phase changed linearly as a function of thickness, and used this to argue that this could only be the case if the skyrmion texture was uniform through the thickness of the sample. Unfortunately, they only used the model $\varphi = mt$. Their fit to the data does not look especially bad, but by eye it appears that a better fit could be obtained by using a linear model with a constant offset. The presence of a constant term in the linear model could indicate the presence of asymmetric Néel caps at the top and bottom of the skyrmions that they observe. They fail to address this point in their paper. Interestingly, this means that the presence of Néel caps at the surface of skyrmions in DMI systems has not been ruled out experimentally.

Here we present the results of a combined approach to determine the full magnetization based on both transmission and surface sensitive data. These experimental results corroborate the micromagnetic and resonance data presented earlier. Interestingly, we found based on fitting an analytical model to the micromagnetic simulations that the full 3D skyrmionic structure can also be described as a fractional or cavity hopfion.

In order to determine if Néel-like domain walls were present at the surface of the film, Scanning Electron Microscopy with Polarization Analysis (SEMPA) was performed at the Center for Nanoscale Science and Technology at NIST. SEMPA relies on measuring the spin-polarization of the low energy secondary electrons that are emitted from the sample while being illuminated by an electron beam probe. These electrons retain the spin polarization of the sample and can thus be used to map all three vector components of the surface magnetization. These electrons will when exposed to a magnetic field, but at different frequencies because they are not monochromatic, making it necessary to collect images in a field-free environment. Luckily, Sergio found that by tuning the composition and thickness of Fe/Gd, a mixed phase of skyrmions, worm domains, and stripes could be stabilized at room temperature and zero applied magnetic field. Samples were prepared using sputter deposition on both Si with a native oxide layer and SiN windows for SEMPA and LTEM respectively with the layer structure Ta 5 nm / [Fe ($\approx$ 3.1 Å– 3.5Å) / Gd ($\approx$ 3.9 – 4.1Å)] x 120 / Pt 2nm. The platinum was used as a capping layer to allow for more easy removal prior to SEMPA imaging, which must have a pristine magnetic surface.

The SEMPA results are shown in Figure 32. The SEMPA data shows the presence of Néel-like domain walls with some remnant in-plane magnetization. Based on LTEM studies this is believed to be caused by the exposure to a slight in-plane field prior to imaging. Similar stripes can be found in the LTEM sample in regions where the sample was exposed to a field that wasn't totally perpendicular to the film (see Figure 32.c). Using LTEM, this was verified by tilting the sample to a slight

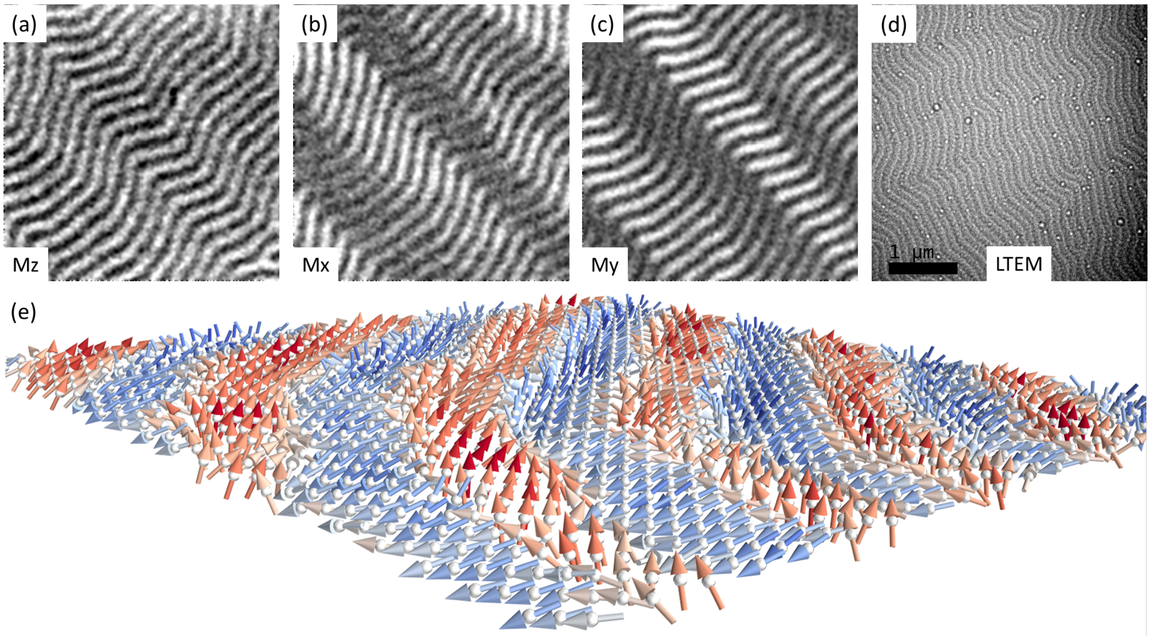

FIGURE 32. SEMPA image of Néel-like walls
(a-c) SEMPA images of each component of the surface magnetization of a Fe/Gd multilayered thin film. (c) LTEM image showing similar magnetic stripes, note the bright dots in the image are caused by structural defects in the SiN substrate. (e) Enlarged 3D visualization of a region in (a-c). Notice the Néel-like character of the domain walls. Also, note that there is a slight remnant in-plane component to the magnetization.

angle applying a field, removing the field and then tilting the sample back to zero. These stripes also appear in region where the SiN window is slightly bowed. The center, edges, and corners of the window are closer to parallel with Si chip making them normal to the applied field, while regions between are slightly tilted receiving some dose of in-plane field. This is similar to the effect that leads to the formation of skyrmion bound pairs[101] discussed in Chapter III. Unfortunately, because of this field history no skyrmions were found during SEMPA imaging. Nevertheless, the presence of Néel caps on the stripe domains in SEMPA, and Bloch walls in the LTEM, are in good agreement with the micromagnetic simulations.

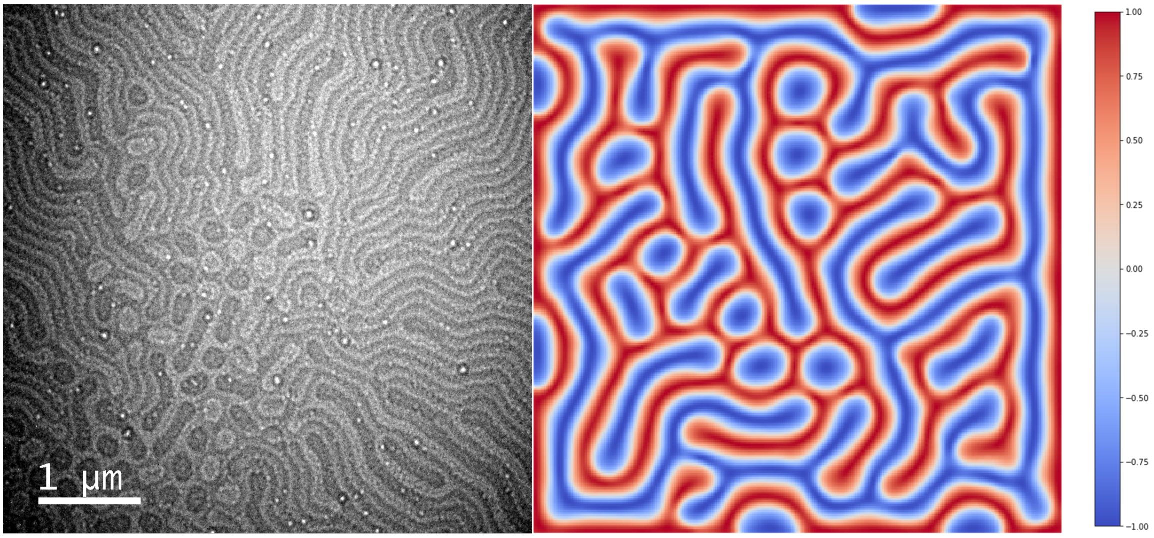

FIGURE 33. Comparison of LTEM with micromagnetic simulations
(a) LTEM data of a region from the same sample shown in Figure 32.c. Again, the bright dots in the image are caused by structural defects in the SiN window. (b) Micromagnetic simulation showing the close agreement between the LTEM and simulated domain morphology. Width of the simulation is 2 μm.

With the surface magnetization determined by SEMPA the only thing left is to confirm that the central thickness of the film has Bloch-type walls. Figure 33 shows the close agreement between the morphology present in the LTEM and the micromagnetic simulation. Again remember that the presence of contrast in this image is evidence of Bloch walls in the projected magnetization. Figure 34 also shows a direct map determined using SITIE on a small region containing a skyrmions. Combining this with the SEMPA results and the previously reported resonance spectra, we believe we have sufficient evidence to conclude that the skyrmion structure determined in the micromagnetic simulations is a close reflection of reality. This makes this the most characterized 3D skyrmion structure.

In an attempt to further determine the 3D structure, we collected a series of tilted images from -30° to 30° (the maximum angle for the single tilt sample holder we were using). Prior to attempting reconstructing this tomographic dataset, a mathematical

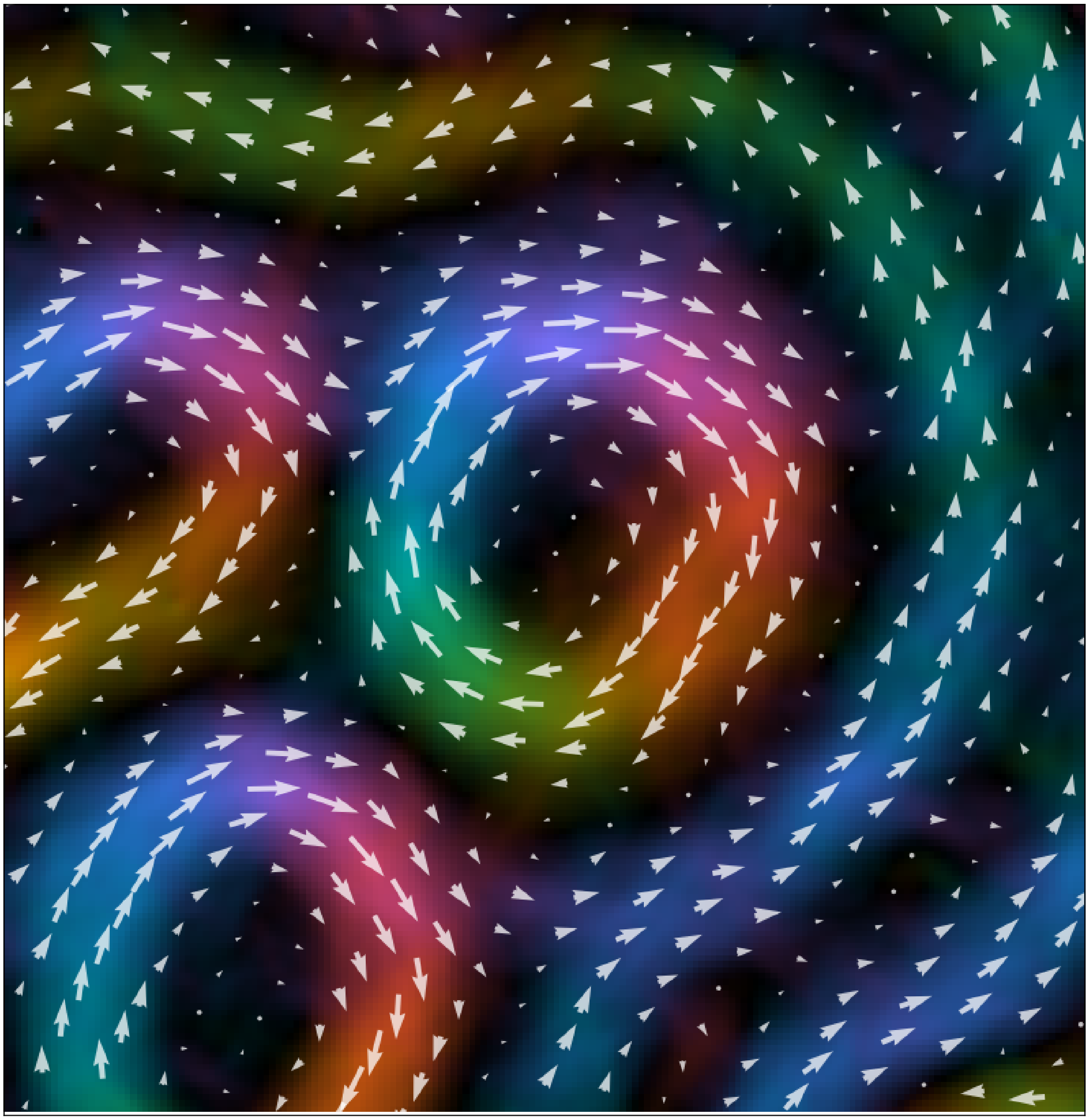

FIGURE 34. Bloch skyrmion
Color and vector map showing a Bloch-type skyrmion and the Bloch nature of the surrounding walls (width of the image is 546 nm).

model was fit to a skyrmion present in the micromagnetic data. This model was then used to simulate the magnetic contrast expected for a tilt series. Additionally, a 'standard' skyrmion with no Néel caps but with the same z and domain wall thickness was also simulated. SITIE was then applied to these images and the x and y components of the magnetic field were computed. These simulations and the experimental data are presented in Figure 35. Viewing the data it is not possible to distinguish between the two models. Even though the data is inconclusive it is presented to demonstrate the difficulty of trying to determine 3D magnetic structure without appealing to complementary techniques like SEMPA.

Fitting a mathematical model to the micromagnetic simulation allows us to use this model to calculate further topological densities, such as the Hopf index. The model used is,

$$\begin{aligned}
m(x,y,z) &= \{m_x, m_y, m_z\} \\
m(x,y,z) &= \{\sin[\Theta(\rho,z)]\cos[\phi-\gamma(z)], \sin[\Theta(\rho,z)]\sin[\phi-\gamma(z)], \cos[\Theta(\rho,z)]\} \\
\Theta(\rho,z) &= 2\tan^{-1}\left[(k(z)\rho^{\alpha(z)}\right] \\
\gamma(z) &= \frac{\pi}{2}\tanh(b_\gamma z) + c_\gamma \\
k(z) &= a_k e^{-b_k z^2} + c_k \\
\alpha(z) &= a_\alpha e^{-b_\alpha z^2} + c_\alpha
\end{aligned} \tag{8.2}$$

This equation is quite complex and warrants some discussion. First we examine $\gamma(z)$ this is the helicity of the skyrmion which now varies as a function of z. This reproduces the Néel caps, changing the skyrmion from Néel-like at the top surface to Bloch at the center and then Néel again at the bottom but this time with the opposite helicity. Next there are the two Gaussian terms $k(z)$, and $\alpha(z)$ these both act to reproduce

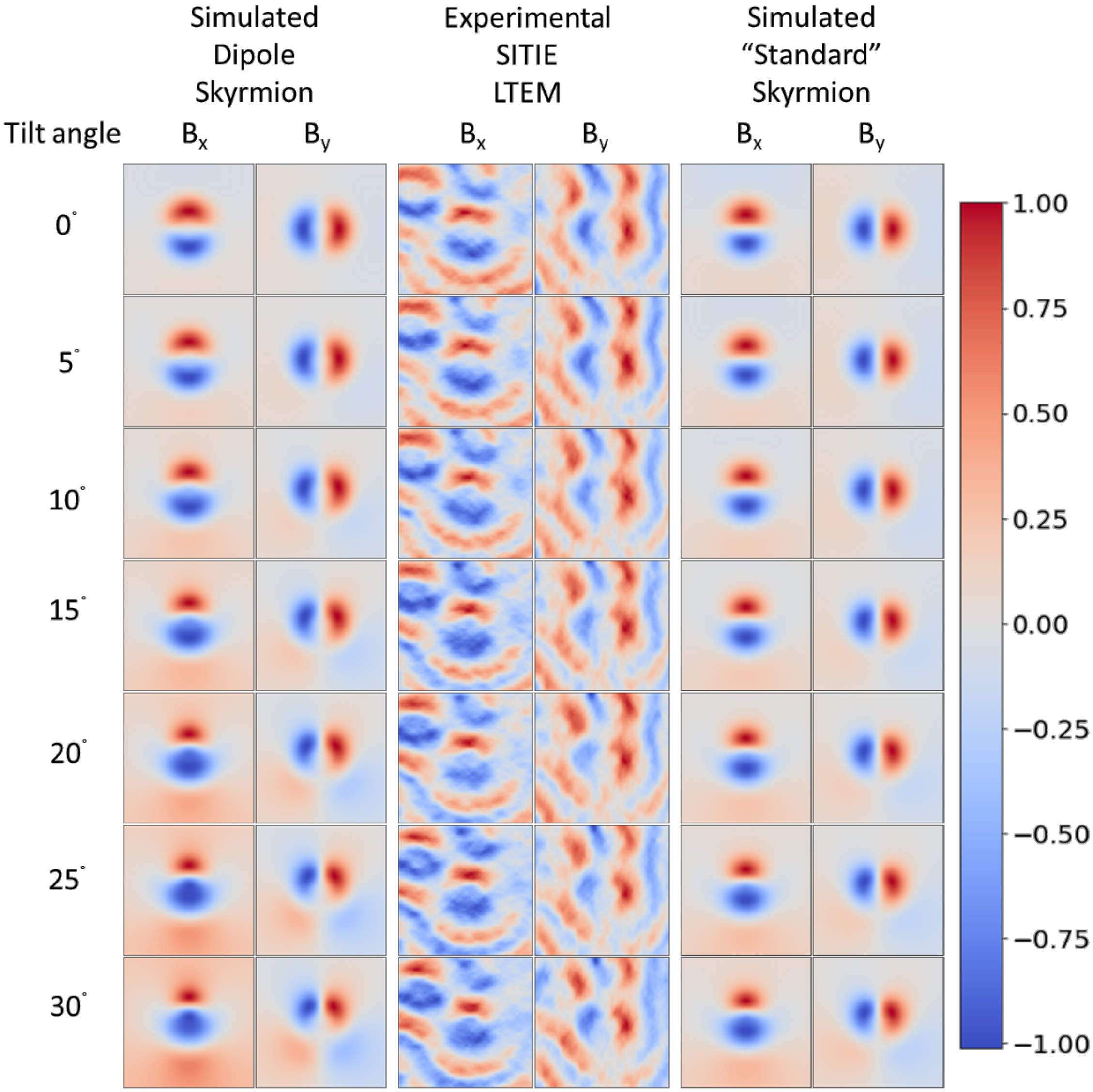

FIGURE 35. Tomographic comparison of LTEM with two models
Simulated and experimental x and y components of the magnetic field of a skyrmion with Néel caps (dipole) and without ('standard').

the barrel like aspect that is present in the domain. The first $k(z)$ sets the extent of the core, while $\alpha(z)$ is the thickness of the domain wall. This results in a nearly perfect reproduction of the micromagnetic simulation skyrmion.

From here we are able to calculate the Hopf index given by,

$$H = \frac{Q}{4\pi} \int_{-\infty}^{-\infty} \int_{0}^{-\infty} \sin(\Theta) \left(\partial_\rho \Theta \partial_z \phi - \partial_z \Theta \partial_\rho \phi \right) \mathrm{d}\rho \, \mathrm{d}z \tag{8.3}$$

The Gaussian terms inside $k(z)$ and $\alpha(z)$ make this particularly difficult to evaluate analytically, but luckily they are continuous deformation of the field and can be dropped when calculating H. With this, H can then be calculated directly using Mathematica with no special tricks, where the limits of integration on z are adjusted to ±40 nm, and is independent of all fitting parameters except b_γ. Substituting in the result from fitting the model gives,

$$H = \frac{\tanh(112.613)}{2} \approx \frac{1}{2} \tag{8.4}$$

Figure 36 shows a 3D model of this fractional Hopfion, along with flow lines which form closed paths and have integer valued linking numbers. Similar formations have been discovered in chiral liquid crystals, another skyrmion-hosting system[102].

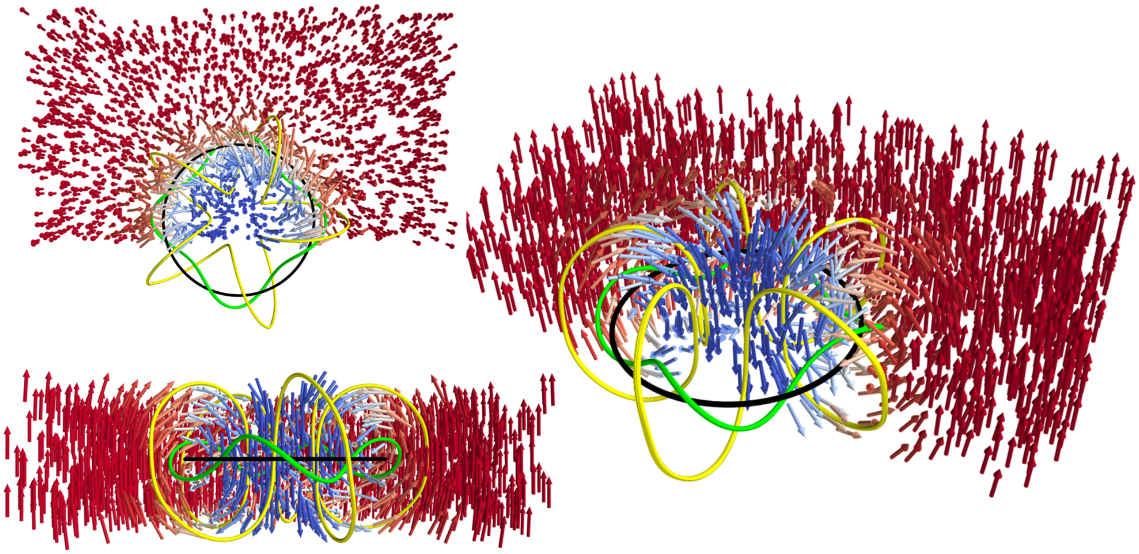

FIGURE 36. Three dimensional visualization of half integer Hopfion
Dipole skyrmion visualized in 3D, showing its Hopf Fibration like character. Also show are flow lines with integer linking numbers.

CHAPTER IX

CONCLUSION AND FUTURE DIRECTIONS

We demonstrated a new simplified phase reconstruction algorithm that was employed to advance the emerging field of magnetic skyrmions. The application of this technique identified the topological defects in Fe/Gd, and allowed for the collection of quasi-dynamic data that was used to characterize domain wall chirality. Further, this technique was coupled with SEMPA to determine the 3-dimensional structure of dipole stabilized skyrmions.

Much of my work has been directed at building up a sufficient code base to analyze and visualize the magnetic information in LTEM data. With this complete, the path is clear to develop new phase measurement techniques geared toward magnetic imaging. Currently, fast direct electron detectors are totally changing the way an electron microscope is used. One such application is MIDI-STEM[103], like many new techniques it was originally marked for increasing phase contrast in biological applications. This technique could likely be applied with no modification to map the phase of magnetic samples. An advantage of using magnetic materials over biological samples, is that most magnetic materials can hold up to much larger electron doses. Further, one could imagine developing probes tailored specifically to be sensitive to the z-component of the magnetic field. Electrons passing through a magnetic field in the z direction experience a rotation, a MIDI-STEM probe could be constructed to maximize sensitivity to this effect.

Adding the capability to measure all three vector components of the magnetic induction in a TEM could will greatly enhance our ability to understand the full 3D character topologically non-trivial magnetizations. Coupling this ability with modern computing power and fast direct electron detectors could have a transformative effect on magnetic imaging similar to the effect that cryo-electron microscopy had on imaging biological molecules[104].

REFERENCES CITED

[1] Arman Shehabi, Sarah Smith, Dale Sartor, Richard Brown, Magnus Herrlin, Jonathan Koomey, Eric Masanet, Nathaniel Horner, Inês Azevedo, and William Lintner. United states data center energy usage report. 2016.

[2] Christopher Helman. Berkeley Lab: It Takes 70 Billion Kilowatt Hours A Year To Run The Internet.

[3] AP Malozemoff and JC Slonczewski. *Magnetic Domain Walls in Bubble Materials: Advances in Materials and Device Research*, volume 1. New York: Academic press, 1979.

[4] Andres R. Lucero, David E. Williams, and James L. Nelson. Cash accounting and surveillance system for games, August 1981.

[5] Robert M. Best. Video games with voice dialog, April 1984.

[6] Stuart S. P. Parkin, Masamitsu Hayashi, and Luc Thomas. Magnetic Domain-Wall Racetrack Memory. *Science*, 320(5873):190–194, April 2008.

[7] Stuart Parkin and See-Hun Yang. Memory on the racetrack. *Nature Nanotechnology*, 10(3):195–198, March 2015.

[8] Albert Fert, Vincent Cros, and Joo Sampaio. Skyrmions on the track. *Nature Nanotechnology*, 8(3):152–156, March 2013.

[9] T. H. R. Skyrme. A non-linear field theory. *Proc. R. Soc. Lond. A*, 260(1300):127–138, February 1961.

[10] S. Mhlbauer, B. Binz, F. Jonietz, C. Pfleiderer, A. Rosch, A. Neubauer, R. Georgii, and P. Bni. Skyrmion Lattice in a Chiral Magnet. *Science*, 323(5916):915–919, February 2009.

[11] A. Neubauer, C. Pfleiderer, B. Binz, A. Rosch, R. Ritz, P. G. Niklowitz, and P. Bni. Topological Hall Effect in the A Phase of MnSi. *Physical Review Letters*, 102(18):186602, May 2009.

[12] C. Pappas, E. Lelivre-Berna, P. Falus, P. M. Bentley, E. Moskvin, S. Grigoriev, P. Fouquet, and B. Farago. Chiral Paramagnetic Skyrmion-like Phase in MnSi. *Physical Review Letters*, 102(19):197202, May 2009.

[13] X. Z. Yu, N. Kanazawa, W. Z. Zhang, T. Nagai, T. Hara, K. Kimoto, Y. Matsui, Y. Onose, and Y. Tokura. Skyrmion flow near room temperature in an ultralow current density. *Nature Communications*, 3:988, August 2012.

[14] Naoto Nagaosa and Yoshinori Tokura. Topological properties and dynamics of magnetic skyrmions. *Nature Nanotechnology*, 8(12):899–911, December 2013.

[15] N. S. Kiselev, A. N. Bogdanov, R. Schfer, and U. K. Rler. Comment on “Giant Skyrmions Stabilized by Dipole-Dipole Interactions in Thin Ferromagnetic Films”. *Physical Review Letters*, 107(17):179701, October 2011.

[16] Motohiko Ezawa. Giant Skyrmions Stabilized by Dipole-Dipole Interactions in Thin Ferromagnetic Films. *Physical Review Letters*, 105(19):197202, November 2010.

[17] Albert Fert, Nicolas Reyren, and Vincent Cros. Magnetic skyrmions: advances in physics and potential applications. *Nature Reviews Materials*, 2:17031, July 2017.

[18] Wanjun Jiang, Gong Chen, Kai Liu, Jiadong Zang, Suzanne G. E. te Velthuis, and Axel Hoffmann. Skyrmions in Magnetic Multilayers. *arXiv:1706.08295 [cond-mat]*, June 2017. arXiv: 1706.08295.

[19] Felix Bttner, C. Moutafis, M. Schneider, B. Krger, C. M. Gnther, J. Geilhufe, C. v Korff Schmising, J. Mohanty, B. Pfau, S. Schaffert, A. Bisig, M. Foerster, T. Schulz, C. a. F. Vaz, J. H. Franken, H. J. M. Swagten, M. Klui, and S. Eisebitt. Dynamics and inertia of skyrmionic spin structures. *Nature Physics*, 11(3):225–228, March 2015.

[20] Marc De Graef and Yimei Zhu. *Magnetic Imaging and Its Applications to Materials, Volume 36*. San Diego : Academic Press, San Diego, 1 edition, 2001.

[21] Earl J Kirkland. *Advanced computing in electron microscopy*. Springer Science & Business Media, 2010.

[22] S.K. Walton, K. Zeissler, W.R. Branford, and S. Felton. MALTS: A Tool to Simulate Lorentz Transmission Electron Microscopy From Micromagnetic Simulations. *IEEE Transactions on Magnetics*, 49(8):4795–4800, August 2013.

[23] M. Mansuripur. Computation of electron diffraction patterns in Lorentz electron microscopy of thin magnetic films. *Journal of Applied Physics*, 69(4):2455–2464, February 1991.

[24] Guoqiang Yu, Pramey Upadhyaya, Xiang Li, Wenyuan Li, Se Kwon Kim, Yabin Fan, Kin L. Wong, Yaroslav Tserkovnyak, Pedram Khalili Amiri, and Kang L. Wang. Room-Temperature Creation and SpinOrbit Torque Manipulation of Skyrmions in Thin Films with Engineered Asymmetry. *Nano Letters*, February 2016.

[25] R. Tomasello, E. Martinez, R. Zivieri, L. Torres, M. Carpentieri, and G. Finocchio. A strategy for the design of skyrmion racetrack memories. *Scientific Reports*, 4, October 2014. 00003.

[26] Xichao Zhang, Yan Zhou, Motohiko Ezawa, G. P. Zhao, and Weisheng Zhao. Magnetic skyrmion transistor: skyrmion motion in a voltage-gated nanotrack. *Scientific Reports*, 5:11369, June 2015.

[27] Xichao Zhang, G. P. Zhao, Hans Fangohr, J. Ping Liu, W. X. Xia, J. Xia, and F. J. Morvan. Skyrmion-skyrmion and skyrmion-edge repulsions in skyrmion-based racetrack memory. *Scientific Reports*, 5:7643, January 2015.

[28] Stefan Krause and Roland Wiesendanger. Spintronics: Skyrmionics gets hot. *Nature Materials*, 15(5):493–494, May 2016.

[29] Xichao Zhang, Motohiko Ezawa, and Yan Zhou. Thermally stable magnetic skyrmions in multilayer synthetic antiferromagnetic racetracks. *arXiv:1601.03893 [cond-mat]*, January 2016. arXiv: 1601.03893.

[30] Seonghoon Woo, Kai Litzius, Benjamin Krger, Mi-Young Im, Lucas Caretta, Kornel Richter, Maxwell Mann, Andrea Krone, Robert M. Reeve, Markus Weigand, Parnika Agrawal, Ivan Lemesh, Mohamad-Assaad Mawass, Peter Fischer, Mathias Klui, and Geoffrey S. D. Beach. Observation of room-temperature magnetic skyrmions and their current-driven dynamics in ultrathin metallic ferromagnets. *Nature Materials*, advance online publication, February 2016.

[31] X. Z. Yu, Y. Onose, N. Kanazawa, J. H. Park, J. H. Han, Y. Matsui, N. Nagaosa, and Y. Tokura. Real-space observation of a two-dimensional skyrmion crystal. *Nature*, 465(7300):901–904, June 2010.

[32] W. Munzer, A. Neubauer, T. Adams, S. Muhlbauer, C. Franz, F. Jonietz, R. Georgii, P. Boni, B. Pedersen, M. Schmidt, A. Rosch, and C. Pfleiderer. Skyrmion lattice in the doped semiconductor ${\text{Fe}}_{1\ensuremath{-}x}{\text{Co}}_{x}\text{Si}$. *Physical Review B*, 81(4):041203, January 2010.

[33] X. Z. Yu, N. Kanazawa, Y. Onose, K. Kimoto, W. Z. Zhang, S. Ishiwata, Y. Matsui, and Y. Tokura. Near room-temperature formation of a skyrmion crystal in thin-films of the helimagnet FeGe. *Nature Materials*, 10(2):106–109, February 2011.

[34] Xiuzhen Yu, Maxim Mostovoy, Yusuke Tokunaga, Weizhu Zhang, Koji Kimoto, Yoshio Matsui, Yoshio Kaneko, Naoto Nagaosa, and Yoshinori Tokura. Magnetic stripes and skyrmions with helicity reversals. *Proceedings of the National Academy of Sciences*, 109(23):8856–8860, June 2012.

[35] X. Z. Yu, Y. Tokunaga, Y. Kaneko, W. Z. Zhang, K. Kimoto, Y. Matsui, Y. Taguchi, and Y. Tokura. Biskyrmion states and their current-driven motion in a layered manganite. *Nature Communications*, 5:3198, January 2014.

[36] D. Morikawa, X. Z. Yu, Y. Kaneko, Y. Tokunaga, T. Nagai, K. Kimoto, T. Arima, and Y. Tokura. Lorentz transmission electron microscopy on nanometric magnetic bubbles and skyrmions in bilayered manganites La1.2sr1.8(Mn1yRuy)2o7 with controlled magnetic anisotropy. *Applied Physics Letters*, 107(21):212401, November 2015.

[37] J. C. T. Lee, J. Chess, S. A. Montoya, X. Shi, N. Tamura, S. K. Mishra, P. Fischer, B. McMorran, S. K. Sinha, E. E. Fullerton, S. D. Kevan, and S. Roy. Synthesizing Skyrmion Molecules in Fe-Gd Thin Films. *arXiv:1603.07882 [cond-mat]*, March 2016. arXiv: 1603.07882.

[38] Wenhong Wang, Ying Zhang, Guizhou Xu, Licong Peng, Bei Ding, Yue Wang, Zhipeng Hou, Xiaoming Zhang, Xiyang Li, Enke Liu, Shouguo Wang, Jianwang Cai, Fangwei Wang, Jianqi Li, Fengxia Hu, Guangheng Wu, Baogen Shen, and Xi-Xiang Zhang. A Centrosymmetric Hexagonal Magnet with Superstable Biskyrmion Magnetic Nanodomains in a Wide Temperature Range of 100340 K. *Advanced Materials*, pages n/a–n/a, May 2016.

[39] S. McVitie, D. McGrouther, S. McFadzean, D. A. MacLaren, K. J. OShea, and M. J. Benitez. Aberration corrected Lorentz scanning transmission electron microscopy. *Ultramicroscopy*, 152:57–62, May 2015.

[40] Charudatta Phatak, Amanda K. Petford-Long, and Marc De Graef. Three-Dimensional Study of the Vector Potential of Magnetic Structures. *Physical Review Letters*, 104(25):253901, June 2010.

[41] Michael Reed Teague. Deterministic phase retrieval: a Greens function solution. *Journal of the Optical Society of America*, 73(11):1434, November 1983.

[42] Christoph T. Koch. Towards full-resolution inline electron holography. *Micron*, 63:69–75, August 2014.

[43] A. Budruk, C. Phatak, A. K. Petford-Long, and M. De Graef. In situ Lorentz TEM magnetization studies on a FePdCo martensitic alloy. *Acta Materialia*, 59(17):6646–6657, October 2011.

[44] A. Budruk, C. Phatak, A. K. Petford-Long, and M. De Graef. In situ lorentz TEM magnetization study of a NiMnGa ferromagnetic shape memory alloy. *Acta Materialia*, 59(12):4895–4906, July 2011.

[45] S. D. Pollard, V. Volkov, and Y. Zhu. Propagation of magnetic charge monopoles and Dirac flux strings in an artificial spin-ice lattice. *Physical Review B*, 85(18):180402, May 2012.

[46] S. D. Pollard, L. Huang, K. S. Buchanan, D. A. Arena, and Y. Zhu. Direct dynamic imaging of non-adiabatic spin torque effects. *Nature Communications*, 3:1028, August 2012.

[47] Hyun Soon Park, J. Spencer Baskin, and Ahmed H. Zewail. 4d Lorentz Electron Microscopy Imaging: Magnetic Domain Wall Nucleation, Reversal, and Wave Velocity. *Nano Letters*, 10(9):3796–3803, September 2010.

[48] C. Phatak, M. Tanase, A. K. Petford-Long, and M. De Graef. Determination of magnetic vortex polarity from a single Lorentz Fresnel image. *Ultramicroscopy*, 109(3):264–267, February 2009.

[49] Samuel A. Eastwood, David M. Paganin, and Amelia C. Y. Liu. Automated phase retrieval of a single-material object using a single out-of-focus image. *Optics Letters*, 36(10):1878, May 2011.

[50] Christoph T. Koch. A flux-preserving non-linear inline holography reconstruction algorithm for partially coherent electrons. *Ultramicroscopy*, 108(2):141–150, January 2008.

[51] S. A. Montoya, S. Couture, J. J. Chess, J. C. T. Lee, N. Kent, D. Henze, S. K. Sinha, M.-Y. Im, S. D. Kevan, P. Fischer, B. J. McMorran, V. Lomakin, S. Roy, and E. E. Fullerton. Dipolar-stabilized skyrmions and skyrmion lattices in Fe/Gd multilayers. *arXiv:1608.01368 [cond-mat]*, August 2016. arXiv: 1608.01368.

[52] A. J. Morgan, A. V. Martin, A. J. D'Alfonso, C. T. Putkunz, and L. J. Allen. Direct exit-wave reconstruction from a single defocused image. *Ultramicroscopy*, 111(910):1455–1460, August 2011.

[53] A. V. Martin and L. J. Allen. Direct retrieval of a complex wave from its diffraction pattern. *Optics Communications*, 281(20):5114–5121, October 2008.

[54] A. V. Martin, A. I. Bishop, D. M. Paganin, and L. J. Allen. Practical implementation of a direct method for coherent diffractive imaging. *Ultramicroscopy*, 111(7):777–781, June 2011.

[55] Yakir Aharonov and David Bohm. Significance of electromagnetic potentials in the quantum theory. *Physical Review*, 115(3):485, 1959.

[56] Marc De Graef and Yimei Zhu. Quantitative noninterferometric Lorentz microscopy. *Journal of Applied Physics*, 89(11):7177–7179, June 2001.

[57] D. Paganin and K. A. Nugent. Noninterferometric Phase Imaging with Partially Coherent Light. *Physical Review Letters*, 80(12):2586–2589, March 1998.

[58] T. E. Gureyev, C. Raven, A. Snigirev, I. Snigireva, and S. W. Wilkins. Hard x-ray quantitative non-interferometric phase-contrast microscopy. *Journal of Physics D: Applied Physics*, 32(5):563, 1999.

[59] V. V. Volkov, Y. Zhu, and M. De Graef. A new symmetrized solution for phase retrieval using the transport of intensity equation. *Micron*, 33(5):411–416, 2002.

[60] Axel Lubk, Giulio Guzzinati, Felix Borrnert, and Jo Verbeeck. Transport of Intensity Phase Retrieval of Arbitrary Wave Fields Including Vortices. *Physical Review Letters*, 111(17):173902, October 2013.

[61] R. Chang, S. Li, M. V. Lubarda, B. Livshitz, and V. Lomakin. FastMag: Fast micromagnetic simulator for complex magnetic structures (invited). *Journal of Applied Physics*, 109(7):07D358, April 2011.

[62] T. E. Gureyev and K. A. Nugent. Phase retrieval with the transport-of-intensity equation II Orthogonal series solution for nonuniform illumination. *Journal of the Optical Society of America A*, 13(8):1670, August 1996.

[63] Tolga Tasdizen, Elizabeth Jurrus, and Ross T Whitaker. Non-uniform illumination correction in transmission electron microscopy. pages 5–6, 2008.

[64] Kazuo Ishizuka and Brendan Allman. Phase measurement of atomic resolution image using transport of intensity equation. *Journal of Electron Microscopy*, 54(3):191–197, June 2005.

[65] A. V. Martin, F. R. Chen, W. K. Hsieh, J. J. Kai, S. D. Findlay, and L. J. Allen. Spatial incoherence in phase retrieval based on focus variation. *Ultramicroscopy*, 106(10):914–924, August 2006.

[66] D. Paganin, A. Barty, P. J. McMahon, and K. A. Nugent. Quantitative phase-amplitude microscopy. III. The effects of noise. *Journal of Microscopy*, 214(1):51–61, April 2004.

[67] P. Chaudhari, J.j. Cuomo, and R.j. Gambino. Amorphous metallic films for magnetooptic applications. *Applied Physics Letters*, 22(7):337–339, April 1973.

[68] Noboru Sato and Kazutaka Habu. Amorphous rareearthtransitionmetal thin films with an artificially layered structure. *Journal of Applied Physics*, 61(8):4287–4289, April 1987.

[69] M. W. Muller. Domain Formation in a Ferromagnetic Plate. *Journal of Applied Physics*, 38(6):2413–2416, May 1967.

[70] M. Hehn, S. Padovani, K. Ounadjela, and J. P. Bucher. Nanoscale magnetic domain structures in epitaxial cobalt films. *Physical Review B*, 54(5):3428–3433, August 1996.

[71] D. M. Donnet, K. M. Krishnan, and Y. Yajima. Domain structures in epitaxially grown cobalt thin films. *Journal of Physics D: Applied Physics*, 28(9):1942, 1995.

[72] Nobuo Saito, Hideo Fujiwara, and Yutaka Sugita. A New Type of Magnetic Domain Structure in Negative Magnetostriction Ni-Fe Films. *Journal of the Physical Society of Japan*, 19(7):1116–1125, July 1964.

[73] D. J. Craik and P. V. Cooper. Criteria for uniaxial magnetostatic behaviour in thin platelets. *Physics Letters A*, 41(3):255–256, September 1972.

[74] J. Beille, J. Voiron, and M. Roth. Long period helimagnetism in the cubic B20 FexCo1xSi and CoxMn1x Si alloys. *Solid State Communications*, 47(5):399–402, August 1983.

[75] B. Lebech, J. Bernhard, and T. Freltoft. Magnetic structures of cubic FeGe studied by small-angle neutron scattering. *Journal of Physics: Condensed Matter*, 1(35):6105, 1989.

[76] Andr Thiaville, Stanislas Rohart, milie Ju, Vincent Cros, and Albert Fert. Dynamics of Dzyaloshinskii domain walls in ultrathin magnetic films. *EPL (Europhysics Letters)*, 100(5):57002, 2012.

[77] Satoru Emori, Uwe Bauer, Sung-Min Ahn, Eduardo Martinez, and Geoffrey S. D. Beach. Current-driven dynamics of chiral ferromagnetic domain walls. *Nature Materials*, 12(7):611–616, July 2013.

[78] Gong Chen, Tianping Ma, Alpha T. NDiaye, Heeyoung Kwon, Changyeon Won, Yizheng Wu, and Andreas K. Schmid. Tailoring the chirality of magnetic domain walls by interface engineering. *Nature Communications*, 4:2671, October 2013.

[79] Niklas Romming, Christian Hanneken, Matthias Menzel, Jessica E. Bickel, Boris Wolter, Kirsten von Bergmann, Andr Kubetzka, and Roland Wiesendanger. Writing and Deleting Single Magnetic Skyrmions. *Science*, 341(6146):636–639, August 2013.

[80] M. Bode, M. Heide, K. von Bergmann, P. Ferriani, S. Heinze, G. Bihlmayer, A. Kubetzka, O. Pietzsch, S. Blgel, and R. Wiesendanger. Chiral magnetic order at surfaces driven by inversion asymmetry. *Nature*, 447(7141):190–193, May 2007.

[81] G. Chen, J. Zhu, A. Quesada, J. Li, A. T. NDiaye, Y. Huo, T. P. Ma, Y. Chen, H. Y. Kwon, C. Won, Z. Q. Qiu, A. K. Schmid, and Y. Z. Wu. Novel Chiral Magnetic Domain Wall Structure in `$\mathrm{Fe}/\mathrm{Ni}/\mathrm{Cu}(001)$` Films. *Physical Review Letters*, 110(17):177204, April 2013.

[82] Gong Chen and Andreas K. Schmid. Imaging and Tailoring the Chirality of Domain Walls in Magnetic Films. *Advanced Materials*, 27(38):5738–5743, October 2015.

[83] Jordan J. Chess, Sergio A. Montoya, Tyler R. Harvey, Colin Ophus, Simon Couture, Vitaliy Lomakin, Eric E. Fullerton, and Benjamin J. McMorran. A streamlined approach to mapping the magnetic induction of skyrmionic materials. *arXiv:1608.06000 [cond-mat]*, August 2016. arXiv: 1608.06000.

[84] Joseph E. Davies, Olav Hellwig, Eric E. Fullerton, Greg Denbeaux, J. B. Kortright, and Kai Liu. Magnetization reversal of $\mathrm{Co}\mathrm{Pt}$ multilayers: Microscopic origin of high-field magnetic irreversibility. *Physical Review B*, 70(22):224434, December 2004.

[85] J. E. Davies, O. Hellwig, E. E. Fullerton, M. Winklhofer, R. D. Shull, and Kai Liu. Frustration driven stripe domain formation in Co/Pt multilayer films. *Applied Physics Letters*, 95(2):022505, July 2009.

[86] Jordan J Chess, Sergio A Montoya, Eric E Fullerton, and Benjamin J McMorran. Determination of domain wall chirality using in situ Lorentz transmission electron microscopy. *AIP Advances*, 7(5):056807, 2017.

[87] Eric Jones, Travis Oliphant, Pearu Peterson, and others. *SciPy: Open source scientific tools for Python.* 2001.

[88] Stfan van der Walt, Johannes L. Schnberger, Juan Nunez-Iglesias, Franois Boulogne, Joshua D. Warner, Neil Yager, Emmanuelle Gouillart, and Tony Yu. scikit-image: image processing in Python. *PeerJ*, 2:e453, June 2014.

[89] P. Perona and J. Malik. Scale-space and edge detection using anisotropic diffusion. *IEEE Transactions on Pattern Analysis and Machine Intelligence*, 12(7):629–639, July 1990.

[90] Luis Pedro Coelho. Mahotas: Open source software for scriptable computer vision. *Journal of Open Research Software*, 1(1), July 2013.

[91] P. Dollar, Zhuowen Tu, and S. Belongie. Supervised Learning of Edges and Object Boundaries. In *2006 IEEE Computer Society Conference on Computer Vision and Pattern Recognition (CVPR'06)*, volume 2, pages 1964–1971, 2006.

[92] Fabian Pedregosa, Gal Varoquaux, Alexandre Gramfort, Vincent Michel, Bertrand Thirion, Olivier Grisel, Mathieu Blondel, Peter Prettenhofer, Ron Weiss, Vincent Dubourg, Jake Vanderplas, Alexandre Passos, David Cournapeau, Matthieu Brucher, Matthieu Perrot, and douard Duchesnay. Scikit-learn: Machine Learning in Python. *Journal of Machine Learning Research*, 12:28252830, October 2011.

[93] C. Moreau-Luchaire, C. Moutas, N. Reyren, J. Sampaio, C. a. F. Vaz, N. Van Horne, K. Bouzehouane, K. Garcia, C. Deranlot, P. Warnicke, P. Wohlhter, J.-M. George, M. Weigand, J. Raabe, V. Cros, and A. Fert. Additive interfacial chiral interaction in multilayers for stabilization of small individual skyrmions at room temperature. *Nature Nanotechnology*, advance online publication, January 2016.

[94] Anjan Soumyanarayanan, M. Raju, A. L. Gonzalez Oyarce, Anthony K. C. Tan, Mi-Young Im, A. P. Petrovic, Pin Ho, K. H. Khoo, M. Tran, C. K. Gan, F. Ernult, and C. Panagopoulos. Tunable Room Temperature Magnetic Skyrmions in Ir/Fe/Co/Pt Multilayers. *Nature Materials*, 16(9):898–904, July 2017. arXiv: 1606.06034.

[95] Hongxin Yang, Andr Thiaville, Stanislas Rohart, Albert Fert, and Mairbek Chshiev. Anatomy of Dzyaloshinskii-Moriya Interaction at Co/Pt Interfaces. *Physical Review Letters*, 115(26):267210, December 2015.

[96] Jordan J Chess, Sergio A Montoya, Tyler R Harvey, Colin Ophus, Simon Couture, Vitaliy Lomakin, Eric E Fullerton, and Benjamin J McMorran. Streamlined approach to mapping the magnetic induction of skyrmionic materials. *Ultramicroscopy*, 177:78–83, 2017.

[97] S. McVitie and M. Cushley. Quantitative Fresnel Lorentz microscopy and the transport of intensity equation. *Ultramicroscopy*, 106(45):423–431, March 2006.

[98] M. J. Benitez, A. Hrabec, A. P. Mihai, T. A. Moore, G. Burnell, D. McGrouther, C. H. Marrows, and S. McVitie. Magnetic microscopy and topological stability of homochiral Nel domain walls in a Pt/Co/AlO$_x$ trilayer. *Nature Communications*, 6:ncomms9957, December 2015.

[99] Shawn D. Pollard, Joseph A. Garlow, Jiawei Yu, Zhen Wang, Yimei Zhu, and Hyunsoo Yang. Observation of stable Nel skyrmions in cobalt/palladium multilayers with Lorentz transmission electron microscopy. *Nature Communications*, 8:ncomms14761, March 2017.

[100] Hyun Soon Park, Xiuzhen Yu, Shinji Aizawa, Toshiaki Tanigaki, Tetsuya Akashi, Yoshio Takahashi, Tsuyoshi Matsuda, Naoya Kanazawa, Yoshinori Onose, Daisuke Shindo, Akira Tonomura, and Yoshinori Tokura. Observation of the magnetic flux and three-dimensional structure of skyrmion lattices by electron holography. *Nature Nanotechnology*, 9(5):337–342, May 2014.

[101] J. C. T. Lee, J. J. Chess, S. A. Montoya, X. Shi, N. Tamura, S. K. Mishra, P. Fischer, B. J. McMorran, S. K. Sinha, E. E. Fullerton, S. D. Kevan, and S. Roy. Synthesizing skyrmion bound pairs in Fe-Gd thin films. *Applied Physics Letters*, 109(2):022402, July 2016.

[102] Paul J. Ackerman, Jao van de Lagemaat, and Ivan I. Smalyukh. Self-assembly and electrostriction of arrays and chains of hopfion particles in chiral liquid crystals. *Nature Communications*, 6:ncomms7012, January 2015.

[103] Colin Ophus, Jim Ciston, Jordan Pierce, Tyler R. Harvey, Jordan Chess, Benjamin J. McMorran, Cory Czarnik, Harald H. Rose, and Peter Ercius. Efficient linear phase contrast in scanning transmission electron microscopy with matched illumination and detector interferometry. *Nature Communications*, 7:10719, February 2016.

[104] Daniel Cressey and Ewen Callaway. Cryo-electron microscopy wins chemistry nobel. *Nature*, 550:167, 2017.